REFERENCE COPY

[redacted]

UNCLASSIFIED

NATIONAL AERONAUTICS AND SPACE ADMINISTRATION

Space Programs Summary No. 37-36 Volume II

for the period September 1, 1965 to October 31, 1965

The Planetary–Interplanetary Program

Classification Changed to UNCLASSIFIED
JPL Letter to Authority NASA-Langley
on Nov. 4, 1970 signed by W.E. Hanson
Date Jan. 4, 1971 By G. Castrin

(Title Unclassified)

JET PROPULSION LABORATORY
LIBRARY
JAN 1 1966

Copy No. 451

CALIFORNIA INSTITUTE OF TECHNOLOGY

JET PROPULSION LABORATORY
CALIFORNIA INSTITUTE OF TECHNOLOGY
PASADENA, CALIFORNIA

November 30, 1965

LAB-C00004

[redacted]
GROUP 4 Downgraded at 3 year intervals; declassified after 12 years

UNCLASSIFIED

141891

Preface

The *Space Programs Summary* is a six-volume, bimonthly publication that documents the current project activities and supporting research and advanced development efforts conducted or managed by JPL for the NASA space exploration programs. The titles of all volumes of the *Space Programs Summary* are:

Vol. I. The Lunar Program (Confidential)

Vol. II. The Planetary–Interplanetary Program (Confidential)

Vol. III. The Deep Space Network (Unclassified)

Vol. IV. Supporting Research and Advanced Development (Unclassified)

Vol. V. Supporting Research and Advanced Development (Confidential)

Vol. VI. Space Exploration Programs and Space Sciences (Unclassified)

The *Space Programs Summary*, Vol. VI consists of an unclassified digest of appropriate material from Vols. I, II, and III; an original presentation of technical supporting activities, including engineering development of environmental-test facilities, and quality assurance and reliability; and a reprint of the space science instrumentation studies of Vols. I and II.

W. H. Pickering, *Director*
Jet Propulsion Laboratory

Space Programs Summary No. 37-36, Volume II

Copyright © 1965, Jet Propulsion Laboratory, California Institute of Technology

Prepared under Contract No. NAS 7-100, National Aeronautics & Space Administration

This document contains information affecting the national defense of the United States, [redacted] Laws, Title 18, U.S.C. Sections [redacted] and 794, the transmission or revelation [redacted] in any manner to an unauthorized person is prohibited by law.

Contents

I. *Mariner* Mars 1964 Project 1
A. Introduction 1
B. Systems 2
C. Guidance and Control 3
D. Telecommunications 9
E. Space Sciences 14
F. Propulsion 21

Reference 22

II. *Voyager* Project 23
A. Introduction 23
B. Guidance and Control 24
C. Telecommunications 31
D. Propulsion 39
E. Quality Assurance and Reliability 45

References 48

III. Future Projects 49
A. Introduction 49
B. Systems 49

I. *Mariner* Mars 1964 Project

A. Introduction

The early objective of the Planetary-Interplanetary Program was the initial probing of the planets Mars and Venus by unmanned spacecraft. The initial probing of Venus was successfully accomplished by *Mariner II*. The next step toward this objective was the initial probing of Mars by a *Mariner C* spacecraft.

The primary objective of the *Mariner C* mission (*Mariner* Mars 1964 Project) was to conduct close-up (flyby) scientific observations of the planet Mars during the 1964-1965 opportunity and to transmit the results of these observations back to Earth. The observations should, to the greatest practical extent, provide maximum information about Mars. Television cosmic dust and a reasonable complement of field and particle experiments were carried. In addition, an Earth occultation experiment was carried out to obtain data relating to the scale height and pressure in the atmosphere of Mars. The Project had the option of launching one spacecraft on a Type II trajectory and waiving the occultation experiment if such action would have maximized the probability of success of the total mission.

A secondary objective was to provide experience and knowledge about the performance of the basic engineering equipment of an attitude-stabilized flyby spacecraft during a long duration flight in space. An additional secondary objective was to perform certain field and/or particle measurements in interplanetary space during the trip and in the vicinity of Mars.

The *Atlas/Agena D* launch vehicle used in this project has a capability of injecting a separated spacecraft weight of 570 lbs (minimum) into a Mars transfer orbit.

It was planned to conduct two launchings of *Mariner C* missions from two separate launch pads. All activities were planned to exploit the limited launch period to the maximum extent. Spacecraft and launch vehicles were processed in parallel, so that following the launch of the first space vehicle the second vehicle could have been launched without delay, no earlier than two days after the first launch.

The *Mariner III* (MC-2) spacecraft was launched November 5, 1964. The nose cone failed to eject from the spacecraft thereby precluding solar panel deployment:

the battery power was depleted 8 hr and 43 min after launch.

The *Mariner IV* (MC-3) spacecraft was successfully launched November 28, 1964 in a Mars encounter orbit about the Sun. Since launch, the spacecraft and mission have assumed the title *Mariner IV* in accord with NASA policy. MC-3 and *Mariner IV* can be and are used interchangeably. MC-3 is the actual serial number of the spacecraft and *Mariner IV* the title assigned to the flying spacecraft and mission.

The Phase 1 portion of the *Mariner IV* flight was successfully concluded October 1 when a DC-12 command was transmitted from the 100-kw Venus DSIF station which resulted in a transfer of the spacecraft transmitter from the high gain antenna to the low gain or omni antenna. Phase 2 has been in process since that moment and consists of periodic attempts by the DSN to receive RF energy from *Mariner IV* in its orbit about the Sun. These attempts will be made approximately once per month, but the earliest significant efforts will probably not take place until the new 210-ft dish antenna system at Goldstone is in an R&D operational mode, sometime in the spring of 1966.

In summary, Phase 1 of the *Mariner IV* was a successful operation. The DSN was in continuous contact (with minor exceptions) for the entire time of 307 days, November 28, 1964 to October 1, 1965. The total arc distance travelled by the spacecraft during this period was 418 million miles, and at the time of the DC-12 command the spacecraft/Earth distance was 191,059,922 mi. A total of 85 commands were transmitted, successfully received, and acted upon by the spacecraft. Approximately 50 million bits of data were received during the mission. No spacecraft failures were experienced during the flight with the exception of the ionization chamber experiment, which transmitted its last data March 17, 1965, and a partial failure or degradation of data of the solar plasma experiment, which occurred December 6, 1964. No detectable deterioration or degradation of performance of any spacecraft subsystem was experienced during the mission.

A quarterly review was held at NASA Headquarters October 28-29, where members of the experimenter teams as well as the spacecraft engineers reported on the status of their responsible area up to the completion of Phase 1. Plans for the publication of the formal *Mariner* Project Report were discussed. The last of the currently planned volumes are to be published by June 1966.

The residual *Mariner* equipment, the MC-4 and proof test model spacecraft and the associated supporting ground equipment, is being held in bonded storage. Final disposition of this equipment is still under study.

B. Systems

1. Space Flight Operations

The *Mariner* 1964 space flight operations (SFO) activities covering the report period of August 26, 1965 through October 1965, have been directed toward the planning, coordination, and participation in postencounter flight operations and final documentation.

On August 26, 1965, SFO was involved in a maneuver inhibit sequence. The maneuver command sequence was designed to provide the maximum protection to the spacecraft against the results of certain discrete failure possibilities for that period between end of mission and the projected reacquisition period in 1967. The sequence called for a DC-13 (maneuver inhibit) and minimum QC-1's. There was no direct verification that the DC-13 would be effective, and therefore, the minimum QC-1 commands were inserted for additional protection.

DC-13 was initiated at 21:06:52 GMT August 26, 1965. QC1-1, which provided a minimum pitch turn, was transmitted at 21:15:16 GMT. QC1-2 was transmitted at 21:23:40 to provide minimum roll turn and the minimum motor burn command, QC1-3, was transmitted at 21:32:04 GMT. All commands were verified by event register indications.

The Canopus update operation, originally scheduled for September 7, was accelerated to an earlier date since observation of the data indicated the possible loss of Canopus could occur prior to the September date.

DC-17, Canopus update, was transmitted August 27, 1965, at 19:40:00 GMT. The event register reading changed, confirming that the command was received by the spacecraft. Channel 303 data confirmed the function of DC-17.

On August 30, 1965, SFO was involved with the second attempt to take pictures of dark space.

At 20:30:00 GMT August 30, 1965, DC-25 was transmitted. This command turned on the tape recorder power and started the platform scanning. DC-3 was transmitted at 21:10:24, which provided all science data. DC-24, which inhibited scan platform motion, was transmitted at 22:48:33 GMT.

DC-16 was transmitted at 23:35:26 GMT to start the record sequence. The command was timed to arrive during the 12-sec possible narrow angle acquisition period following a green filter. Since the television will gain step only after the narrow angle acquisition logic is satisfied and only then after a green filter, pictures at all gain steps were recorded.

DC-2 was transmitted at 00:05:00 GMT for the purpose of obtaining Mode 2 data. DC-26 was transmitted at 00:44:00 GMT. This command turned all science off and turned off the battery charger. The DC-2 was transmitted prior to this command as all science was being received at the time, and without the DC-2 all telemetry would have been lost.

DC-22, switch tracks on the recorder was transmitted at 00:49:00 GMT followed by DC-4, Mode 4 data playback, at 01:25:00 GMT. At 02:00:46 the start of the first picture data of the second record sequence was received at the SFOF.

On September 1, 1965, SFO was involved in the playback of the second recording sequence of *Mariner IV*. The camera during this sequence saw dark space and stepped through its four gain levels sequentially on the first five recorded pictures.

This operation provided additional data on the dark response of the camera system in order to aid interpretation of the haze or fogging of the *Mariner IV* pictures. The following data were obtained from the second picture playback.

(1) Absolute dark current response of the vidicon surface

(2) Signal-to-noise characteristics of the entire system in all gain positions

Playback of the five pictures of dark space was completed September 2, 1965, and operations were directed toward returning the spacecraft to a cruise condition.

DC-28 was transmitted September 2, 1965, at 06:17:00 GMT for the purpose of turning off the video system. DC-28 also turned on the battery charger, and therefore, DC-26 was transmitted at 06:23:00 GMT to turn the battery charger off. DC-2 was transmitted at 06:29:00 GMT to place the spacecraft in the cruise mode of operation. This was verified at 07:00:32 GMT by the presence of Mode 2 data.

During the remainder of September no command action was planned due to the interferometer effect, which eliminated the possibility of any command action. This condition existed until just prior to mission termination, which was established as October 1, 1965.

Documentation was started during the month of September for the final project progress report. During September, *Mariner* Mars 1964 technical bulletins 276 through 305 were documented and distributed. The *Mariner IV* flight history chart was updated during this period, and in addition, all previously recorded data were rechecked.

On October 1, 1965, at 21:30:17 GMT, DC-12 was transmitted to *Mariner IV*. DC-12 switches from transmit via the spacecraft high-gain antenna to transmit via the spacecraft low-gain antenna. This resulted in the loss of down link communications.

The last signal from *Mariner IV* was received at 22:05:07 GMT October 1, 1965. Since the termination of Phase I of the *Mariner IV* mission, effort is being directed on the final project progress report. The final two *Mariner* Mars 1964 technical bulletins, numbers 306 and 307 were issued. The *Mariner IV* flight history chart was completed October 6, 1965. This chart will be in the final project progress report.

C. Guidance and Control

1. Spacecraft Power: Mariner IV Flight Analysis

With the one exception of the higher-than-expected battery voltage (see below), operation of the power subsystem was completely normal and predictable throughout the first 307 days of flight of *Mariner IV* after which

UNCLASSIFIED

the antenna changeover precluded the receipt of further data.

Solar panel performance was normal with no evidence of degradation. The actual outputs from the solar panel's open-circuit and short-circuit standard cell transducers agreed with the predicted values within 5%. These, plus the solar panel operating point voltages, currents, and temperatures, gave a large measure of confidence that the panels were operating normally.

Power conditioning equipment operated perfectly during the flight. The main inverter output voltage was constant for any given load, and the voltage variation in going from the maximum load during midcourse maneuver to the minimum load during TV picture playback was 0.6 v ac. This was a highly acceptable value. The power distribution assembly, which controls the turning "on" and "off" of various loads, was operated in all of its modes and performed normally. Similarly, the battery charger, power synchronizer, all regulators, and all inverters performed in a normal manner.

The only area of power system operation that was not completely understood was the battery. As previously noted (*SPS 37-33*, Vol. II, p. 4) the battery voltage increased during the flight to values greater than those predicted at launch. Two theories were proposed to explain the increase.

(1) The increase was a normal consequence of the 0-g gravitational field, temperature effects, and the small (1.6 ma) charge current produced by the battery voltage telemetry transducer.

(2) The battery case had cracked and electrolyte was leaking out slowly and evaporating; this produced a partially open cell which the battery voltage telemetry transducer interpreted as increased voltage.

When the antenna changeover was made, the battery voltage had increased to 37.2 v dc. Since the voltage did not exceed 38.0 v dc—a limit at which Theory 2 would become more likely—there is no way of positively determining which theory is correct. Numerous attempts were made to resolve the problem (including life tests with identical batteries, tests on individual cells, conferences with representatives of the battery manufacturer, etc.), but no solutions were reached. A definite answer to the battery voltage anomaly, using *Mariner IV* data, appears impossible. Only continued study of silver-zinc batteries may provide the answer.

2. Test Results on the Effects of Ionizing Radiation on the Mariner C Canopus Sensor[1]

a. Introduction. The purpose of this article is to present the history of *Mariner IV* Canopus sensor radiation testing, to describe the test conducted and the test results, and to present the analysis used to determine the margin of the Canopus tracker to the Van Allen belt radiation, which was based on the test results.

Ionizing radiation was to be encountered from the Van Allen belts near Earth, possible belts near Mars and from solar flares. It was known that the image dissector would be susceptible to radiation; however, it was difficult to estimate the effect on tracker performance. Simulation of these special environments and the design of the Canopus tracker and attitude control system were important parts of the *Mariner IV* development program.

Evaluating the performance of the tracker in the presence of the type of ionizing radiation to be encountered was quite difficult. The primary radiation comes from high energy particles (protons and electrons) trapped by planetary magnetic fields or emanating from the Sun in solar flares. Difficulty in obtaining a suitable test facility delayed a test using high energy particles until after launch. Prior to launch, tests were conducted on the tracker using 200-kev x-ray radiation. The results of these tests indicated that Van Allen belt radiation might cause the roll error signal to be noisy and that large solar flares, causing 100 r/hr ionization rate within the tracker, might cause the tracker to lose acquisition on Canopus. This test was recognized as being very crude, but it indicated that the tracker was somewhat sensitive to high radiation levels. To avoid possible confusion, the initial Canopus acquisition was delayed until 16 hr after launch. By then the spacecraft was well clear of the Van Allen belt.

Added importance was attached to the postlaunch radiation test due to reports from R. Davies that measurements from Jodrell Bank indicated that the radiation belts at Mars were 10^6 times those of the Earth. More information was needed on the magnitude of the Mars belts and on tracker radiation sensitivity to make decisions concerning the best mode for spacecraft operation at encounter.

Tracker tests were conducted using electrons accelerated by a 3-Mev dynamitron linear accelerator. The primary objective of the test was to determine the sensitivity of the tracker to the radiation found in the outer

[1]For a description of the Canopus sensor see *SPS 37-21* and *37-29*, Vol. II.

UNCLASSIFIED

Van Allen belts (primarily electrons). In particular, the amount of radiation required to cause the spacecraft to lose acquisition on Canopus was of primary concern, since this was the important failure mode near the Mars encounter. The point of loss of acquisition was precisely defined by the inability of the tracker to generate position error signals sufficient to fire the positive and negative attitude control jets.

b. Test setup. To adequately evaluate tracker performance, it is necessary to plot the roll error and intensity signal vs star roll position. A remote control star simulator was built to automatically scan a simulated star through the field of view of the Canopus tracker (Fig. 1). The position of the star was picked off a potentiometer and used to drive the x-axis of an x-y recorder. Intensity and roll error voltages were simultaneously plotted vs the roll position of the star. The simulated star was scanned across the field of view for each electron energy and each current density.

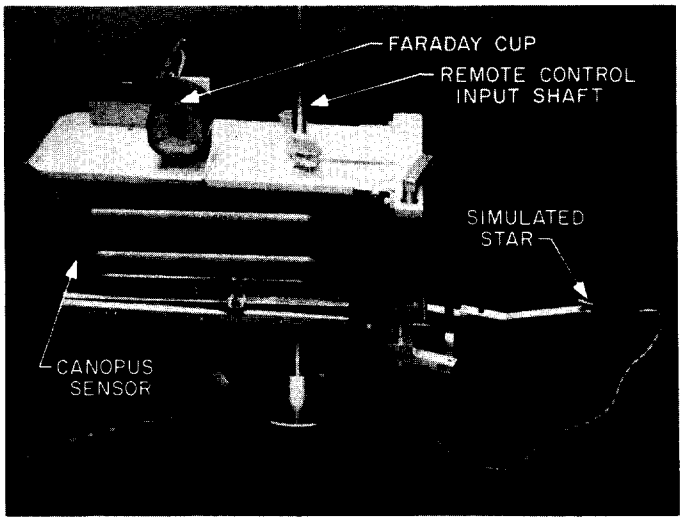

Fig. 1. Canopus sensor shown mounted in the vacuum chamber attached to the dynamitron accelerator

The dynamitron accelerator located at General Dynamics Convair was used for the electron source.[2] The beam was scattered by passing it through 0.004-in. thick copper foils. Scattered beam uniformity was measured by traversing it with a faraday cup. The intensity of the radiation fell off no more than 25% at the extremes of the tracker.

Since the tracker is sensitive to light, set-up validation tests were conducted. Light from the electron source filament and light from corona in the accelerator were shown to be adequately blocked from the tracker. After the conclusion of the test, Eldon Haines of JPL suggested that we may have been disturbed by light emanating from the copper scattering foils. It can be shown that, if all the energy deposited in the copper foils is transformed into visible light with $\lambda = 5550$ Å, the average brightness of the foil would be 23 ft-L for a radiation level at the tracker of 10^{10} electrons/cm^2/sec. This quantity of light would just cause the tracker outputs to behave as observed at this radiation level. However, our assumption concerning the conversion of energy to visible light is surely pessimistic by several orders of magnitude. It can, therefore, be concluded that luminescence of the foils did not make the tracker appear more sensitive to radiation than it really is.

The television system which was also subjected to radiation in this chamber looked directly at this foil and saw no light. Since their threshold is 10 ft-L, a margin over a factor of two is guaranteed over the worst-worst case analysis performed. The set-up was, therefore, valid from a stray light standpoint.

c. Permanent damage. The total surface radiation dosage exceeded 1.2×10^6 r. Two damage effects are noticed. The first was a discoloration of the fiberglass printed circuit boards and the solithane. The insulation characteristic of the boards was not changed enough to degrade the performance of the tracker, if at all.

The light-flint front element of the optical system suffered a degradation in transmission of 35%. The total dose received by the lens can be inferred to be 3,000 r, since transmission vs dose data have been taken on this material. No degradation was expected nor did it occur in the quartz element of the optical system.

No change in image dissector responsitivity was observed. The dark current also relaxed back to a level which could not be detected by the tracker. The relaxation of dark current after radiation intensities of 1×10^{10} electrons/cm^2/sec was not instantaneous. The apparent intensity for no star fell instantly from 25 × Canopus to 0.19 × Canopus when the radiation stopped, but complete recovery indicated by an apparent intensity of 0.04 × Canopus was not reached for several hours. This residual dark current, present immediately after exposure to high levels of radiation, is not sufficiently high to measurably degrade tracker performance on Canopus.

[2]Details of the test setup are reported in *SPS 37-34,* Vol. II, pp. 2–5.

d. Tracker failure modes. Radiation was expected to have three effects on the tracker roll error signal.

(1) Increased noise

(2) Decreased scale factor and saturation voltages

(3) Offsets in the star null position voltage

Since accuracy requirements are not particularly stringent at encounter, the criteria for tracker failure is defined by the incapacity of the unit is to generate a roll error signal sufficient for attitude control while tracking Canopus. Roll error saturation voltages exceeding ± 2.0 v are required to maintain attitude control.

In Fig. 2 the roll error saturation voltage, the null voltage, and the roll error peak to peak noise are plotted. This particular plot is for electrons accelerated to 2.5 Mev, scattered by two 0.004-in. copper foils, and irradiating the top cover of the tracker. Failure occurs at 4×10^9 electrons/cm^2/sec. Radiation causes a null offset voltage. The null shift polarity is a function of the direction of incident radiation. Since Van Allen radiation would be omnidirectional, null voltage offsets would not be expected to occur until reaching higher levels than indicated by the tests run in the General Dynamics accelerator. Fig. 2 is typical of tracker performance for monoenergetic electrons. The tracker is only slightly less sensitive to radiation incident on the side, and the sensitivity to radiation increases with electron energy.

In addition to disturbing the roll error signal radiation, it also disturbs the star intensity signal telemetry. A calibration curve of the apparent star intensity with no star in the field of view vs radiation flux is shown in Fig. 3. Loss of roll control occurs when the apparent star intensity is approximately $6.0 \times$ Canopus. If the radiation becomes strong enough to look like $6.0 \times$ Canopus, then the roll error saturation voltages while tracking Canopus will be less than ± 2.0 v.

e. Calculation of tracker apparent intensity output on the Earth's Van Allen belt. Several assumptions are necessary to extrapolate the measured performance of the tracker for monoenergetic electrons with energies between 0.875 and 2.25 Mev for the expected performance on the continuum of electrons contained in the Van Allen belts.

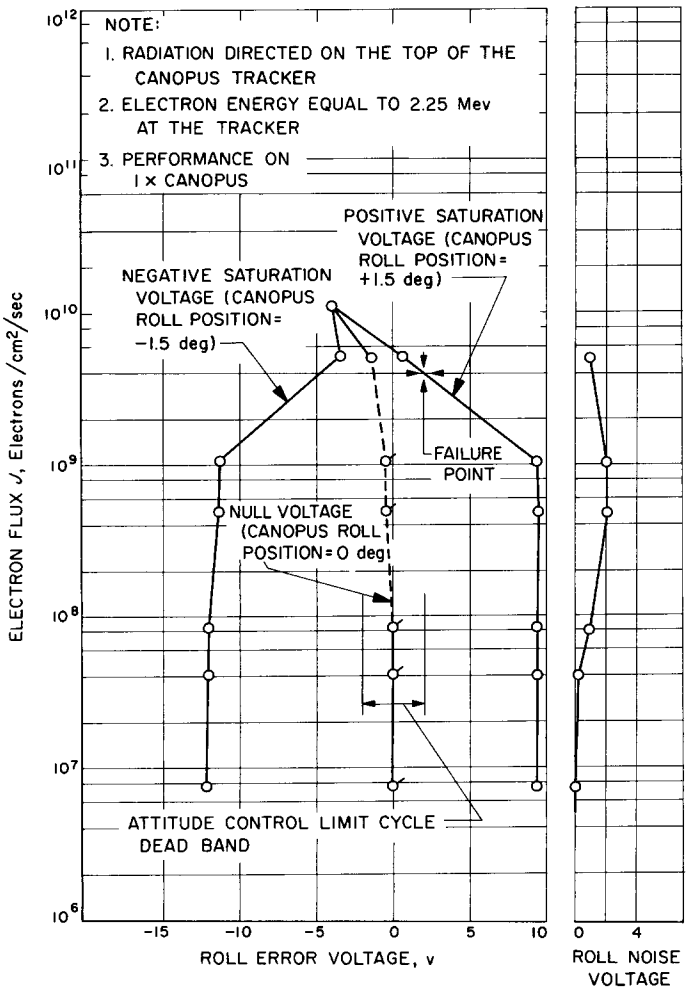
NOTE:
1. RADIATION DIRECTED ON THE TOP OF THE CANOPUS TRACKER
2. ELECTRON ENERGY EQUAL TO 2.25 Mev AT THE TRACKER
3. PERFORMANCE ON 1 × CANOPUS
POSITIVE SATURATION VOLTAGE (CANOPUS ROLL POSITION= +1.5 deg)
NEGATIVE SATURATION VOLTAGE (CANOPUS ROLL POSITION= −1.5 deg)
FAILURE POINT
NULL VOLTAGE (CANOPUS ROLL POSITION=0 deg)
ATTITUDE CONTROL LIMIT CYCLE DEAD BAND
ELECTRON FLUX J, Electrons/cm²/sec
ROLL ERROR VOLTAGE, v
ROLL NOISE VOLTAGE

Fig. 2. Roll error saturation voltage, null voltage and roll error p-p noise voltage

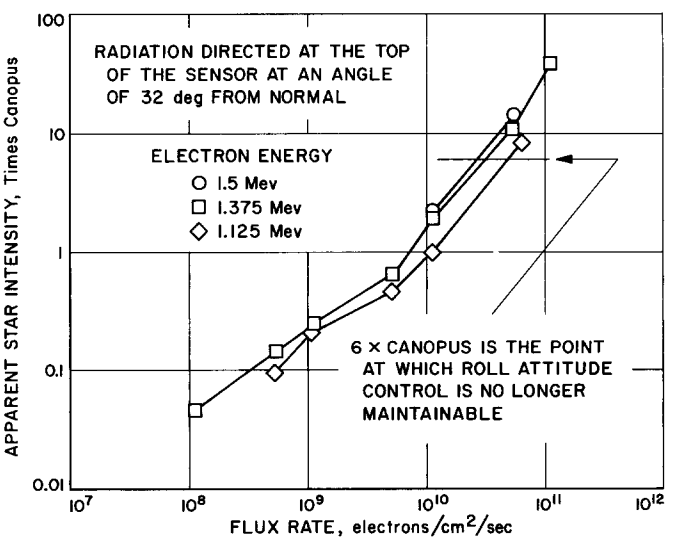
RADIATION DIRECTED AT THE TOP OF THE SENSOR AT AN ANGLE OF 32 deg FROM NORMAL
ELECTRON ENERGY
O 1.5 Mev
□ 1.375 Mev
◇ 1.125 Mev
6 × CANOPUS IS THE POINT AT WHICH ROLL ATTITUDE CONTROL IS NO LONGER MAINTAINABLE
APPARENT STAR INTENSITY, Times Canopus
FLUX RATE, electrons/cm²/sec

Fig. 3. Apparent star intensity for no star input vs radiation flux rate

Assumptions

(1) That the tracker responds to the internal ionization rate produced by the radiation. Rough calculations correlating previous x-ray test data indicate this to be a valid assumption

(2) That the internal ionization rate is proportional to the square of incident electron energy (nonpenetrating electrons)

This assumption is valid in the range of the test data, but it is conservative, since low energy electrons are probably less effective than would be predicted under this assumption.

A best fit of these assumptions to the actual data is shown in Fig. 4. Data taken with two scattering foils have been corrected to agree with data for one foil at 1.5 Mev. The discrepancy in the data (a factor of 5.6) for one and two scattering foils is probably due to the extra bremsstrahlung which occurs at a given radiation flux level when the beam is scattered by two foils. A rough estimate of the ionization rates internal to the tracker due to the bremsstrahlung from the foils indicates that this is a likely explanation for the discrepancy. It is felt that even the data taken with one scattering foil may be somewhat pessimistic, however, a detailed analysis would be required to properly evaluate this factor. Since the data taken with one foil are the most realistic data they will be used for this analysis.

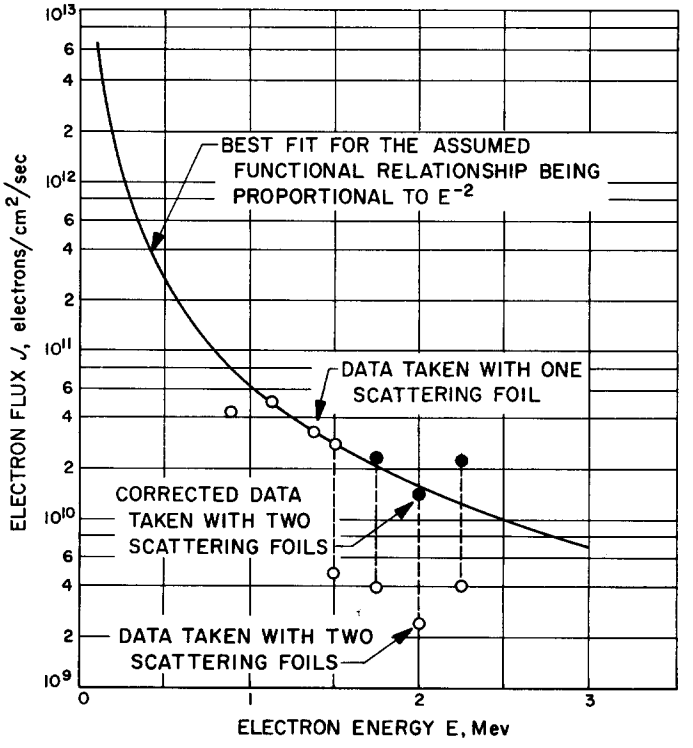
ELECTRON FLUX J, electrons/cm²/sec
BEST FIT FOR THE ASSUMED FUNCTIONAL RELATIONSHIP BEING PROPORTIONAL TO E⁻²
DATA TAKEN WITH ONE SCATTERING FOIL
CORRECTED DATA TAKEN WITH TWO SCATTERING FOILS
DATA TAKEN WITH TWO SCATTERING FOILS
ELECTRON ENERGY E, Mev

Fig. 4. Electron flux to cause the apparent intensity out of the Canopus tracker to be 6.0 × Canopus vs electron energy

The output of the tracker on monoenergetic electrons is

$$I_a = K \cdot J^n$$

I_a = Apparent intensity

K = Constant which varies with energy

J = The current density

n = 1 (from Fig. 2)

Although we had expected n to be ½ (based on our flat background tests), inspection of Fig. 2 shows that n turned out to be 1. Assuming that the predominate effect on the tracker is the release of electrons within the image tube, this indicates that these electrons were

(1) Being modulated

(2) Being primarily emitted from the photocathode in a spatially nonuniform manner

Since the internal ionization rate is proportional to E^2, $K = K' E^2$

$$\therefore I_a = K' \cdot E^2 \cdot J$$

Data plotted in Fig. 4 are for $I_a = 6 \times$ Canopus, at 1.5 Mev and $J = 2.7 \times 10^{10}$ electrons/cm²/sec.

$$\therefore K' = \frac{6}{2.25 \cdot 2.7 \times 10^{10}}$$

$$K' = 0.99 \times 10^{-10} \frac{\text{cm}^2/\text{sec}}{\text{Mev}^2 \text{ electron}}$$

For the Van Allen belt the output of the tracker would be

$$I_a = \int_{,}^{\infty} K \cdot E^2 \cdot J(E)\, dE$$

where $J(E)$ is the Van Allen belt radiation density function in electrons/cm²/sec-Mev. This integration can be performed numerically using the distribution function for Van Allen radiation which is available from *Explorer XIV*

UNCLASSIFIED

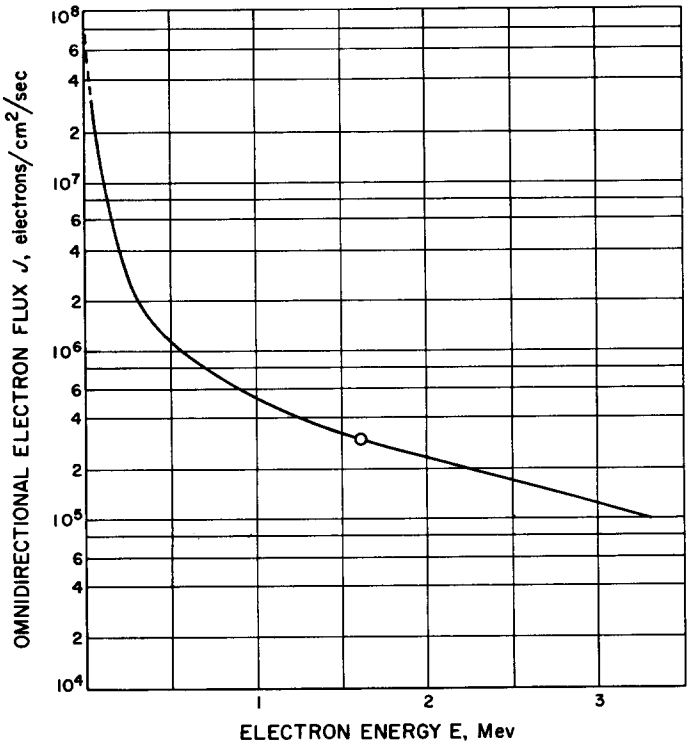

Fig. 5. Outer Van Allen belt electron distribution function

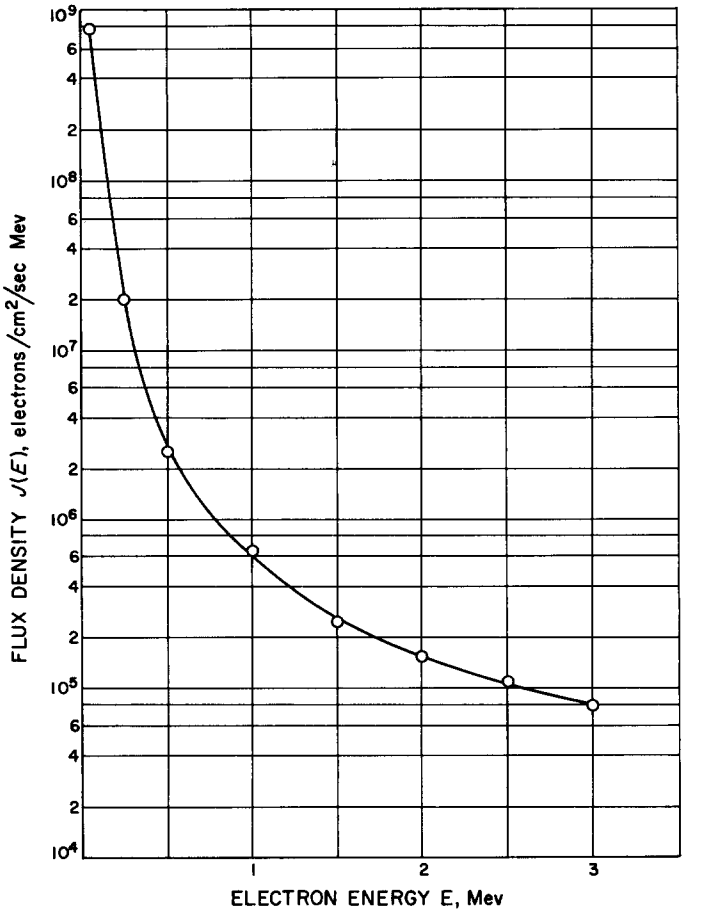

Fig. 6. Outer Van Allen belt electron density function derived from Fig. 5

measurements. Fig. 5 is a plot of these data. Fig. 6 shows the radiation density function $J(E)$ derived from these data. Integration from 0 to 2.5 Mev yields

$$I_a = 0.99 \times 10^{-10} \times 1.765 \times 10^6$$

$$I_a = 1.75 \times 10^{-4} \times \text{Canopus}$$

Since failure is predicted for $I_a = 6 \times$ Canopus the operating margin in the Earth's Van Allen belt, neglecting electrons with energy greater than 2.5 Mev is

$$\text{Margin} = \frac{6}{1.75 \times 10^{-4}} = 34{,}000$$

Continuing the integration above 2.5 Mev is not possible because the assumptions concerning tracker sensitivity are no longer applicable. Range energy considerations predict that 1.9 Mev electrons will penetrate to the photocathode if the tracker is irradiated at 32 deg from the top. However, no additional sensitivity due to penetrating electrons was noted up to an energy of 2.25 Mev. The ionization rate inside the tube goes up radically if electrons penetrate the tube. The tracker appears to be sensitive to the ionization rate for x-rays; and if it is also sensitive to the ionization rate for electrons, tracker sensitivity to penetrating electrons should be high. Tracker failure has been previously estimated to occur at an x-ray ionization rate of 6,000 r/hr. This would correspond to an electron flux density of 5×10^7 electrons/cm²/sec above 2.5 Mev. An operating margin can be computed for the tracker under the above assumptions taking the geometry of the most sensitive area into account.

$$\text{Margin} = \frac{5 \times 10^7 \text{ flux}}{1.65 \times 10^5 \dfrac{\text{flux}}{4\pi \text{ sterad}} \times 0.37 \text{ sterad}}$$

$$= 10{,}000$$

From these estimates of the sensor performance in Van Allen belt-like radiation environments it is possible to tabulate (Table 1) expected Canopus sensor performance for various levels of radiation which might have been encountered at Mars.

The accuracy of the radiation levels in Table 1 is no better than an order of magnitude. However, the margin

UNCLASSIFIED

Table 1. Expected Canopus sensor performance in Van Allen belt-like radiation environments

Radiation level in Earth's Van Allen belts	Canopus sensor performance
Greater than 20,000	Possible null offsets exceeding the attitude control deadband
10,000	Loss of Canopus acquisition
1,600	(1) Scale factor reduced by a factor of two. (2) p-p noise equal to 1/2 the deadband.
550	Low gate comes on for no star input
250	Low gate does not drop out if the star leaves the field of view

on loss of acquisition of Canopus was sufficiently large so that the use of backup modes of roll control during encounter with Mars was not required.

D. Telecommunications

1. The Mariner IV Interferometer Antenna Pattern

a. Introduction. The *Mariner IV* spacecraft used two antennas, a low gain antenna and a high gain antenna, to communicate with the DSIF. In order to verify the performance of the *Mariner* antennas, and to provide data for use in making accurate predictions of communications performance during the flight, rather extensive full scale spacecraft antenna patterns were taken.

The antenna patterns are recordings that are proportional to the amount of RF power radiated or received in any direction from the spacecraft. The majority of patterns recorded consisted of exciting one or the other of the two antennas with an RF signal. However, it was predicted, and later borne out as the flight progressed, that both antennas would radiate or receive the same signal simultaneously under certain conditions. This action would result in an interferometer pattern unlike any of the above mentioned recorded patterns.

Nonetheless, the patterns recorded with only a single antenna excited could be used to determine some elements of the interferometer pattern. The actual interferometer pattern could only be known before flight by a full scale pattern recording of the actual spacecraft flight, which was not practical to obtain.

Because the RF components of any particular spacecraft could be replaced at any time before liftoff with similar (but not identical) components, actual spacecraft flight patterns could not be recorded.

Accurate patterns for use in communications predictions could be generated, however, if certain in-flight pattern data could be obtained during the early portion of the flight. The required data consist of the angular directions about the spacecraft of an adjacent maximum and a minimum in the interferometer pattern and the relative amplitude of each. These data were obtained from the spacecraft receiver AGC telemetry readings and from tracking data.

The origin of the interferometer pattern is contained in the spacecraft radio subsystem.

b. The spacecraft radio subsystem. The *Mariner IV* radio subsystem is designed so that the transmitter or receiver can be switched to operate with either high gain or the low gain antenna. The switching operation is effected with circulator switches. Fig. 7 shows in simplified form the various modes of operation. Since the "effective" isolation provided by the circulator switches is finite, more than one path is possible for transmission of RF energy through the system. The net result of the finite isolation is to make possible the transmission or reception of the same signal over both antennas on the spacecraft. Constructive or destructive interference is possible, depending upon the relative amplitudes and phases of the interfering signals. Because the two antennas are many wavelengths apart, the relative phase between antenna signals will vary with varying look angles to the

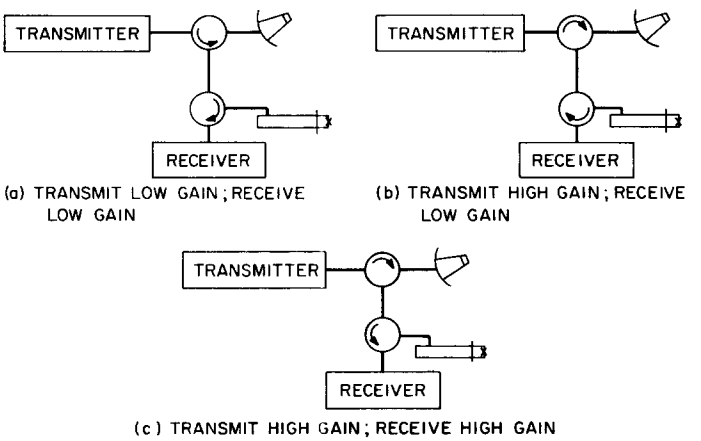

Fig. 7. Simplified schematics of the *Mariner IV* radio-subsystem antenna modes

UNCLASSIFIED

spacecraft. Due to this phase variation, the relative amplitude of the composite signal resulting from the two antennas simultaneously transmitting or receiving will vary with look angles to the spacecraft. The resulting amplitude variation with spacecraft cone and clock angle is the interferometer pattern of the two antennas.

To begin an analysis of the *Mariner* interferometer effect, consider first the signal leakage mechanism aboard the spacecraft.

c. System signal leakage mechanism. The leakage mechanism in the RF circuits of Fig. 7 is a combination of actual circulator isolation and circulator termination mismatch return loss. That is, unwanted RF signals may wind up at a circulator port via wrong-way circulation ("isolation" path) and via reflection from a mismatched termination with right-way circulation ("return-loss" path). The actual unwanted signal magnitude at the port in question depends upon the relative magnitudes and phase differences between the signals via the two paths. Hence, the leakage is a function of circulator isolation, termination mismatch, and interconnecting line lengths.

For example, assume that the circulator switches in Fig. 7 have infinite isolation for "wrong way" circulation. In the transmit-high-gain–receive-low-gain mode, a normal 2116 Mc signal will be conducted to the spacecraft receiver from the low gain antenna. In addition, any signal received by the high gain antenna will be circulated toward the low gain antenna. If the low gain antenna and/or interconnecting cables produce a reflected signal due to mismatched impedance, then this reflected signal will also be conducted to the spacecraft receiver.

This one example is representative of the many possible paths through the system. In general, leakage also occurs through wrong-way circulation. The interference can exist in both down-link and up-link.

Table 2 shows isolation measurements of a *Mariner* circulator switch at the transmit and receive frequency with its ports connected to a receiver or transmitter, but with the unused antenna port terminated in a matched load.

Fig. 8 shows mismatch return loss as a function of VSWR. A perfect circulator terminated in this mismatch would have an effective isolation equal to the mismatch return loss.

Table 2. Isolation of a *Mariner* circulator switch

Antenna mode		Frequency, Mc	
Receiver gain	Transmitter gain	2116 Isolation, db	2298 Isolation, db
Low	Low	21.4	29.7
Low	High	21.1	29.6
High	High	20.6	31.0

Test Conditions: Unused antenna port terminated in a matched load. No drive to transmitter.

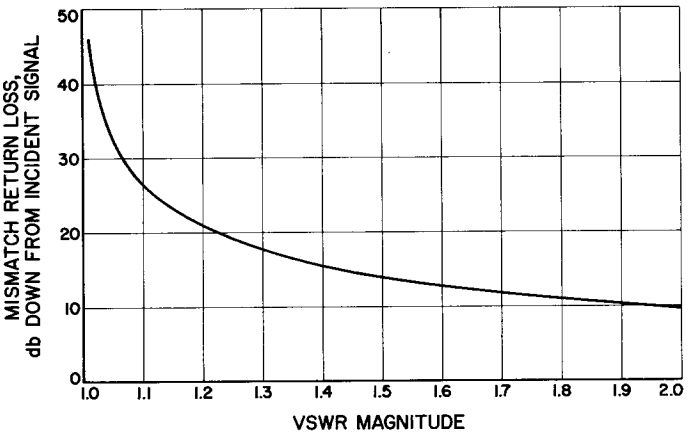

Fig. 8. Mismatch return loss vs VSWR

The point to be made is that interference effects may occur even with near-perfect components in the system if other system components interact to yield a low effective isolation.

Early in the *Mariner* RF system design the problem of circulator switch leakage was recognized, but the decision was made to continue the design. For the planned portion of the flight where the interferometer pattern occurred—over the solid angle of the high gain main beam—the spacecraft transmitter and receiver were to be connected to the high gain antenna. The large gain coupled with normal isolation to the low gain antenna would make the interferometer pattern for this switch mode negligible. Fig. 9 shows the maximum expected peak to null variation in db for two signals differing by the indicated db magnitude.

When full scale *Mariner C* (preflight designation) spacecraft antenna patterns were made, the circulator system leakage was simulated and sample patterns were taken. The leakage was simulated with 10, 20, and 30 db directional couplers. Pattern cuts were made through the low and high gain nominal pattern peaks at both transmit

UNCLASSIFIED

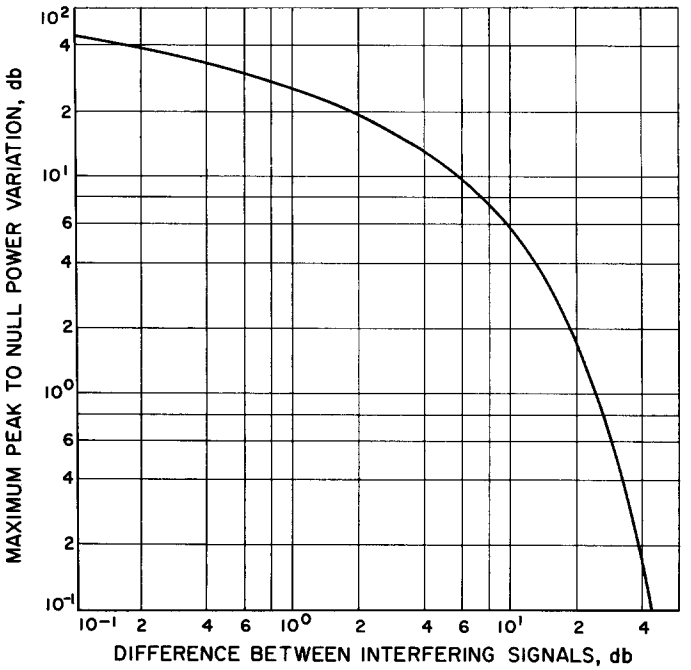

Fig. 9. Maximum ripple magnitude vs relative source strength

and receive frequencies for various positions of a line-stretcher in one antenna's feed line.

Mariner IV left the Earth in the transmit-low-gain–receive-low-gain mode. Prelaunch predictions based on an assumed isolation of 25 db indicated that +7- to −11-db maximum variations from the nominal low gain patterns could exist over that portion of the low gain pattern encompassing the high gain antenna main beam (around 38-deg cone angle). Until switchover from low gain transmitting to high gain transmitting occurred (March 5, 1965, 28-deg cone angle), the maximum variations encountered were approximately ±4 db from nominal on up-link and approximately ±3 db on down-link.

After the mode switching occurred, the interferometer effect ceased to exist on the down-link because the increased antenna gain increased the difference between interfering signals radiated via low and high gain antennas. However, the circulator switching caused the previous conditions of path phase and effective isolation for the up-link to change.

Since the project office made the decision to remain on low gain receiving, it was possible to map and to predict the interferometer pattern aboard the *Mariner IV* as the trajectory caused the spacecraft to turn in relation to the Earth.

Curve fitting analytical interferometer pattern data to the received carrier power data from the spacecraft (2116 Mc) shows the effective isolation from the high gain antenna to the receiver to be only 12.5 db for the transmit-high–receive-low mode.

One explanation for this low effective isolation is that the low gain antenna VSWR is approximately 1.3, and cable VSWR's were on the order of 1.2. These two mismatches alone could combine under worst case conditions to yield an effective VSWR of approximately 1.5, depending upon their relative phases and spatial separations. For comparison (Fig. 8), a return loss of 12.5 db is possible from a 1.63 VSWR mismatch.

To continue the analysis of the *Mariner IV* interferometer effect, consider how the interferometer pattern is created.

d. Interferometer pattern mechanics. Fig. 10 shows two dissimilar antennas situated symmetrically about the y-axis in the x-y plane of a rectangular coordinate system. Consider antenna A independently having a voltage pattern in the x-y plane $f(\theta)$, and similarly $g(\theta)$ for antenna B, where $f(\theta) \neq g(\theta)$.

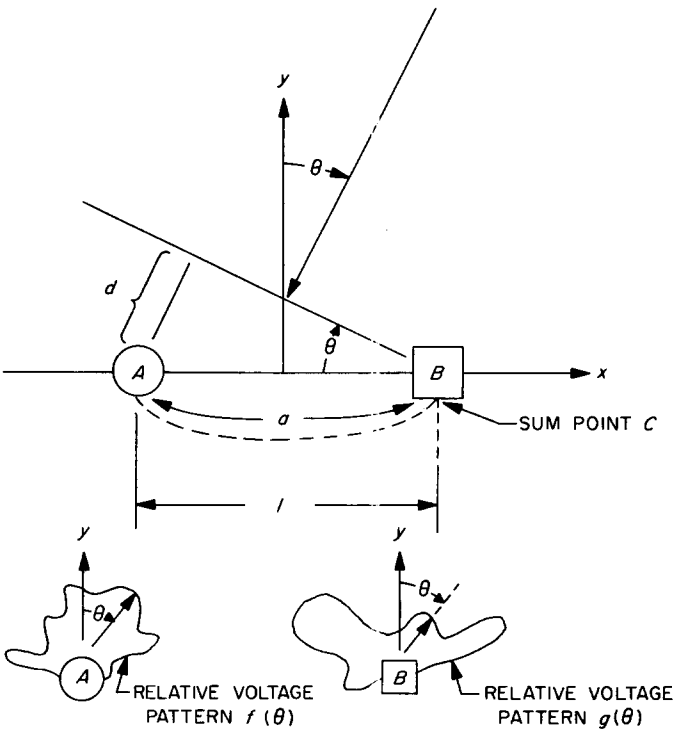

Fig. 10. Dissimilar interferometer antennas

The outputs of the two antennas (considered as receiving) are connected at C, as shown in the dashed line in Fig. 10. In the absence of radiative mutual-coupling, the output at C for a plane wave incident at angle θ is the sum of the voltage outputs of the independent antennas. For any θ the separate output voltages are proportional to the antenna's voltage pattern amplitudes at θ.

The sum must be made with due regard to the "radiated" and the "conducted" phase differences. Radiated phase difference is the phase difference corresponding to the difference in arrival time of the same incident wavefront at the two antennas. This is indicated by d in Fig. 10. Conducted phase difference is the phase difference corresponding to the difference in arrival time at the sum point C of the voltages from each antenna. This is represented by the cable of length a in Fig. 10.

Taking antenna B to the zero phase reference in the system shown in Fig. 10, the time harmonic voltages at C are (omitting e^{jwt}) represented by

$$V_B(\theta) = g(\theta) \tag{1}$$

and

$$V_A(\theta) = f(\theta)\, e^{-j\beta(l\sin\theta + a)} \tag{2}$$

where

$$\beta = \frac{2\pi}{\lambda}, \qquad l\sin\theta = d$$

The composite output voltage is given by the sum of Eqs. (1) and (2).

$$V_C(\theta) = g(\theta) + f(\theta)\, e^{-j\beta(l\sin\theta + a)} \tag{3}$$

The output power is given by

$$P_C(\theta) = V_C(\theta) \cdot V_C(\theta)^* \tag{4}$$

or

$$P_C(\theta) = f^2(\theta) + g^2(\theta) + 2f(\theta)\, g(\theta)\cos\beta(l\sin\theta + a) \tag{5}$$

Eq. (5) is the interferometer pattern in the x-y plane of the two coupled antennas.

Some consequences of Eq. (5) are

(1) The power distribution in θ is dependent on a, the conducted phase factor, only to the extent that a determines the location of pattern peaks and nulls; i.e., changing a only changes the angular location of peaks and nulls, not the overall pattern shape.

(2) The angular width between nulls is determined by l and θ. The smallest angular pattern features occur around the $\theta = 0$ deg direction.

(3) If $f(\theta) = g(\theta)$, $P_c(\theta)_{max} = 4f^2(\theta)$, i.e., a 6-db increase over the nominal power pattern db value. $P_c(\theta)_{min} = 0$ for the same condition; i.e., infinite nulls in db value.

Generalizing to the 3-dimensional *Mariner IV* case, the radiated phase difference factor d can be obtained from the projection of a vector representing the spacecraft antenna separation l, on a unit vector along the line of sight to the spacecraft.

Let

$$\mathbf{l} = l(\sin\theta_1\cos\phi_1\,\mathbf{i}_x + \sin\theta_1\sin\phi_1\,\mathbf{i}_y + \cos\theta_1\,\mathbf{i}_z) \tag{6}$$

where θ_1, ϕ_1 are the cone and clock angles, respectively, in spacecraft coordinates, of the separation l between the antenna phase centers.

The line of sight (LOS) unit vector is

$$\mathbf{LOS} = \sin\theta\cos\phi\,\mathbf{i}_x + \sin\theta\sin\phi\,\mathbf{i}_y + \cos\theta\,\mathbf{i}_z \tag{7}$$

where θ and ϕ are spacecraft cone and clock angles for the look angles to the spacecraft.

$$d = \mathbf{l}\cdot\mathbf{LOS} = l[\sin\theta_1\sin\theta\cos(\phi_1 - \phi) + \cos\theta\cos\theta_1] \tag{8}$$

The up-link interferometer pattern equation similar to Eq. (5) for the *Mariner IV* in transmit-high-gain $1/N$ receive-low gain mode is

$$P(\theta) = f_{LG}^2(\theta,\phi) + k^2 g_{HG}^2(\theta,\phi) + 2f_{LG}(\theta,\phi)\, k g_{HG}(\theta,\phi)\cos\left[\frac{2\pi}{\lambda}(d + a)\right] \tag{9}$$

where $f_{LG}(\theta,\phi)$ is the low gain antenna relative voltage pattern in cone θ and clock ϕ angles. $g_{HG}(\theta,\phi)$ is the high gain antenna relative voltage pattern. k is the coefficient of coupling between the high gain antenna and the spacecraft receiver. k is a measure of the "effective" isolation. a is the "conducted" phase difference factor. d is Eq. (8).

By subtracting space loss from the spacecraft received carrier power and plotting this amplitude vs spacecraft cone and clock angle (obtained from nominal trajectory data) the actual interferometer pattern was obtained.

Then, the digital antenna pattern (DAP) recorder data from the full scale DTM spacecraft model was substituted for $f_{LG}(\theta, \phi)$ and $g_{HG}(\theta, \phi)$ in Eq. (9). By varying the magnitude of k and a, for a best fit of the actual data, the predicted interferometer pattern elements were determined. The best fit values of k and a are $k = 0.237$ and $a = 0$. The value of k corresponds to -12.5 db effective isolation. A 1620 computer program called "INTERF" has been written to calculate Eq. (9). For input data in db from the *Mariner IV* DAP, the interferometer pattern gain in db relative to right circular isotropic is

$$P(\theta,\phi) = 10\log_{10}\left\{\left[\log_{10}^{-1}\frac{\mathrm{db}_{LG}(\theta,\phi)}{20}\right]^2 + \left[0.237\log_{10}^{-1}\frac{\mathrm{db}_{HG}(\theta,\phi)}{20}\right]^2 + 2\log_{10}^{-1}\left(\frac{\mathrm{db}_{LG}(\theta,\phi)}{20}\right) \times 0.237\left(\frac{\mathrm{db}_{HG}(\theta,\phi)}{20}\right)\cos 10.8\tau \times [0.279\sin\theta\cos(101\,\mathrm{deg} - \phi) - 0.96\cos\theta]\right\} \quad (10)$$

where $10.8\tau = 10.8$ turns (1 turn = 360 deg). (J. D. Kraus, "Antennas," McGraw-Hill Book Co., New York, 1950, has in the Appendix, pp. 515–519, a table of trigonometric functions for decimal fractions of a turn. The resolution is 0.005 turns or 1.8 deg.)

Fig. 11 shows a portion of the actual and the predicted interferometer pattern obtained from space loss rectified, received carrier power at the spacecraft, and from Eq. (10), respectively.

Fig. 12 shows plots of Eq. (10) for effective isolation of 11.5 db ($k = 0.266$), 125 db ($k = 0.237$), and 13.5 db ($k = 0.212$). As can be seen by observing the pattern magnitude at 30-deg cone angle, the depth of the pattern null is quite sensitive to the value of effective isolation.

Fortuitously, the actual interferometer pattern was so disposed about the spacecraft that a pattern maximum occurred at the look angles during encounter. At look angles other than over the high gain antenna main beam, the normal low gain antenna pattern still existed. Thus, the interferometer pattern provided higher gain than normal for the mission and yet retained the low gain or omnidirectivity for command reception capability in the event the spacecraft lost attitude control.

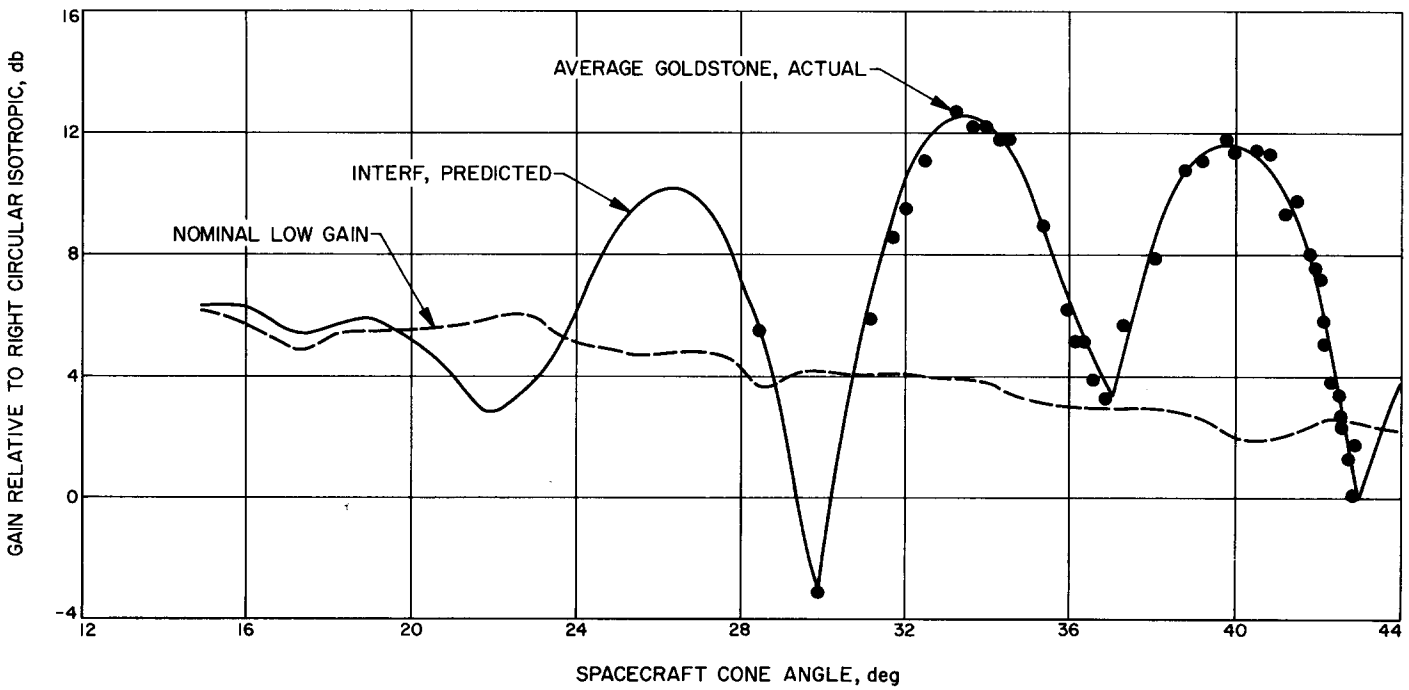

Fig. 11. *Mariner IV* up-link interferometer pattern

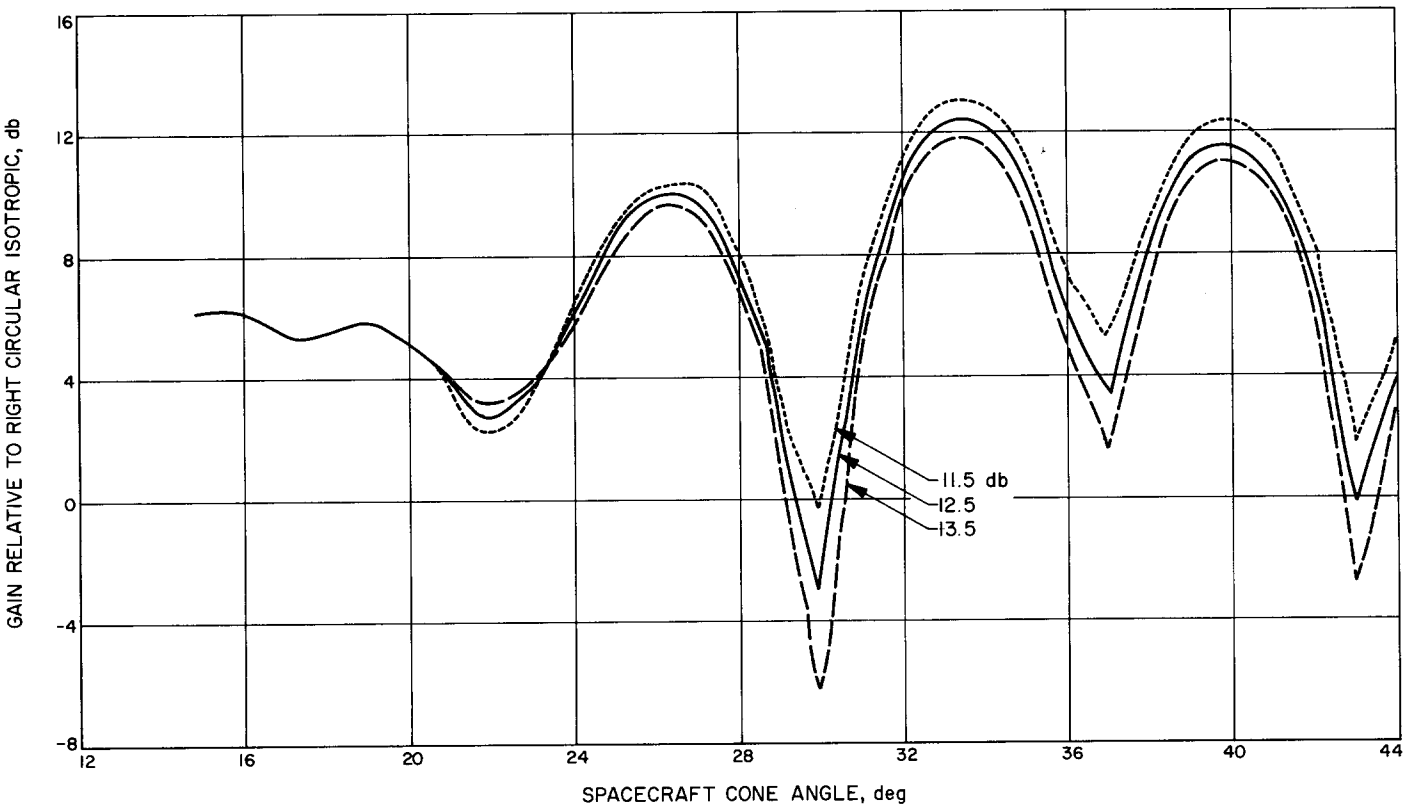

Fig. 12. *Mariner IV* interferometer pattern calculated for various coupling values

In future mission design the possibility of interferometer patterns should be more thoroughly investigated.

E. Space Sciences

1. Testing the Mariner-C TV Shutter Solenoid in a Space Molecular Sink Simulator

a. Introduction. When it was decided to initiate an early encounter science turn-on during the *Mariner IV* Mars encounter, it became necessary to obtain additional data on the life expectancy of the television camera shutter in the space environment. The pacing item affecting the operational life of the shutter is the rotary solenoid. Because of this, additional life testing of the solenoids was proposed.

In order to start the mission with a relatively "fresh" solenoid, new solenoids were retrofitted on all of the flight shutters just before the final spacecraft system tests at the Air Force Eastern Test Range. To successfully complete the *Mariner IV* photographic mission, the life requirement on the solenoid was from 2600–2800 exposures, which includes the exposures put on the shutter during subsystem and spacecraft system tests after the solenoid retrofit and during the February 1965 encounter science turn-on and the exposures necessary to complete the mission during Mars encounter. The operational life of solenoids tested at ambient conditions ranged from 16,000–29,000 exposures, but no data were available on the life expectancy of the solenoids in the clean, hard vacuum of space.

To realistically simulate the lubrication and mechanical wear conditions existing in the solenoid in the space environment, an extremely clean, ultrahigh-vacuum test environment was required. No test chamber at JPL could provide such a test environment. However, a system called a space molecular sink simulator (molsink), developed by Section 375 of the Jet Propulsion Laboratory under the office of advanced Research and Technology program No. 124-09-04-01 for experimental research, which could provide a clean, ultrahigh-vacuum test en-

vironment, was made available for life testing additional solenoids.

From these tests it was hoped that a more realistic determination of the shutter life expectancy could be made.

b. The solenoid. The rotary solenoid used to actuate the *Mariner IV* shutter was a stock commercial solenoid modified to meet JPL's requirements for flight hardware. The rotary motion was produced by three hardened steel balls rolling in inclined ball races as the armature was pulled down by the magnetic force of the coil. The total rotary motion of the solenoid was 45 deg. A coil spring attached to the armature shaft and the solenoid base produced the return motion when the coil current was turned off. Fig. 13 is an exploded view of the solenoid.

The solenoid was lubricated with a solid film lubricant (MoS_2 in a sodium silicate binder), which was sprayed onto the surfaces and then heat cured. Its primary function in the solenoid was to prevent metal to metal contact between moving surfaces, although it had some lubricating properties. Metal to metal contact was avoided because of the possibility of cold welding. The solid lubricant, of course, eventually wears away by the abrasive action of the moving surfaces. This abrasive action was particularly severe between the hardened balls and the ball races because of the extremely high contact stresses (100,000–200,000 psi). The limited wear life of this solid film lubricant determined the useful life of the solenoid.

The *Mariner-C* TV shutter required two solenoid cycles to complete one shutter exposure. That is, the first solenoid cycle opened the shutter and the second cycle closed the shutter. The exposure time was the time between the first and second solenoid pulses or cycles.

c. Vacuum chamber description. The space molecular sink simulator consists of an 18-in. diameter by 30-in. Varian stainless steel bell jar vacuum system which uses

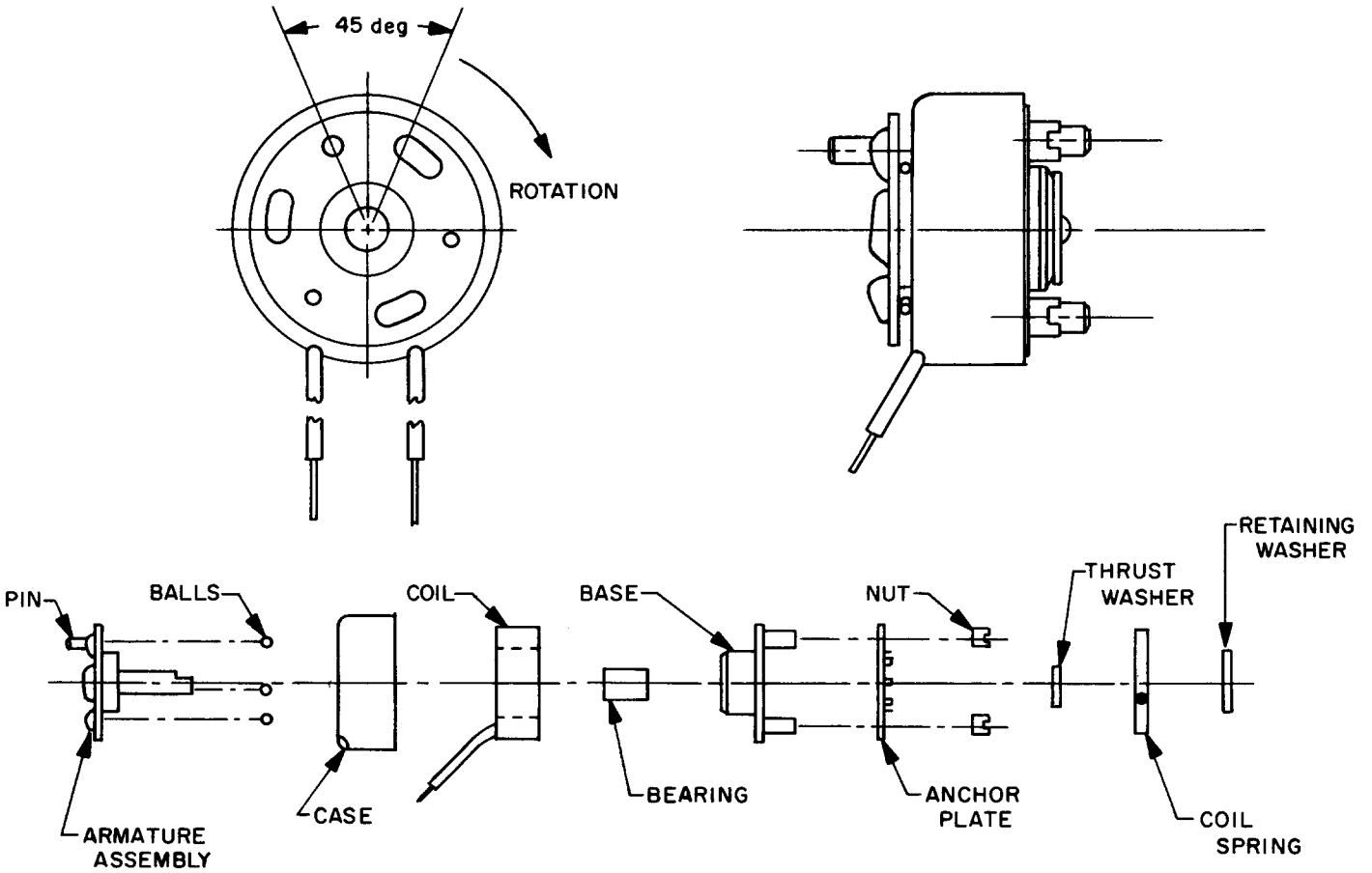

Fig. 13. Rotary solenoid, *Mariner*-C TV shutter (exploded view)

UNCLASSIFIED

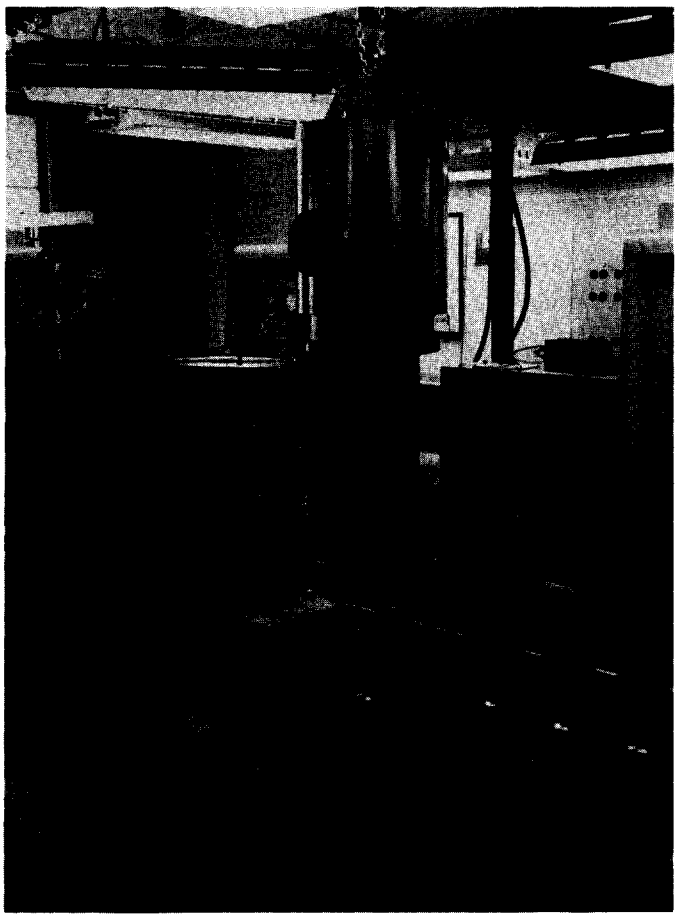

Fig. 14. Space molecular sink simulator

all metal seals and is ion-getter and titanium sublimation pumped. Fig. 14 depicts the chamber with the LN_2 cooled molecular trap removed. Fig. 15 is a view of the inside of the molecular trap array. The longitudinal sharp wedge fins of the array provide an order of magnitude capture improvement for condensible molecules emanating from the test item over that provided by a smooth wall at the same temperature. This arrangement will capture all but one out of every 10,000 condensible molecules (H_2O, oil, plasticizers) emanating from the test item before they can restrike it. Since the test item is the major source of gas within the molecular trap; this ratio and the actual outgassing rate of the test item determine the monolayer formation time at the surface of the test item.

A very rough estimate of the monolayer formation time can be made by estimating the test item gas evolution rate and also the capture coefficients of these gases upon the molecular trap surfaces and upon the test item surfaces. Combining these estimates with the known dimensions and configuration of the molecular trap and the test item, it could be assumed that the monolayer formation time was long with respect to the cycle time of the solenoids tested. For example, if the solenoid released one monolayer of water per second (2×0^{-5} torr-liters/cm^2/sec) from its exposed surfaces, it would take 1 hr for a monolayer of water to form on a cleaned (bearing surface) surface, provided all of the molecules that struck that surface stuck. The indigenous noncondensible gas pressure (nitrogen was the only gas detected by the residual gas analyzer) was measured to be about 1×10^{-9} torr. This provided a monolayer formation time of about 5 hr if it were assumed that only 10% of the nitrogen that struck the clean surface stuck. Further explanation of the space molecular sink chamber and its operation can be found in *SPS 37-30* and *37-34*, Vol. IV.

d. Test description and procedure. A total of nine solenoids were life tested in the molecular sink simulator during the period of June 15–July 21, 1965. Five of the solenoids were given an initial run-in of 1400 to 1800 exposures at ambient temperature and pressure before placing them in the molsink chamber. The other four solenoids were not given the 1400 to 1800 exposure run-in before the test but were turned on only long enough to verify that they were operating properly.

The reason for the initial run-in of five of the solenoids was to find out if a run-in of 1000 to 2000 exposures at ambient conditions had any effect on the operating life of the solenoid in a high vacuum. The solenoid on *Mariner IV* had 1500 exposures put on it at ambient conditions before launch.

The solenoids were mounted on a test fixture similar to the one shown in Fig. 16. Several fixtures were fabricated to accommodate the various numbers of solenoids that were tested in the chamber. The temperature of the solenoids was controlled by a heater wire soldered to the solenoid mounting plate and was monitored by a thermocouple attached to the mounting plate or the solenoid itself. Power leads from the solenoid were soldered to vacuum sealed terminals on the top plate of the fixture. The top plate, which serves as a vacuum seal, was mounted on the top of the chamber with the solenoid mounting plate suspended from it inside the chamber.

After the solenoid was mounted in the chamber, it was operated a few times to verify that it was working properly. The chamber was then pumped down to the 10^{-8} torr range and the system baked out at 175°F for 48 hr. The bake-out cleaned the system of condensible molecules

UNCLASSIFIED

[redacted]
UNCLASSIFIED

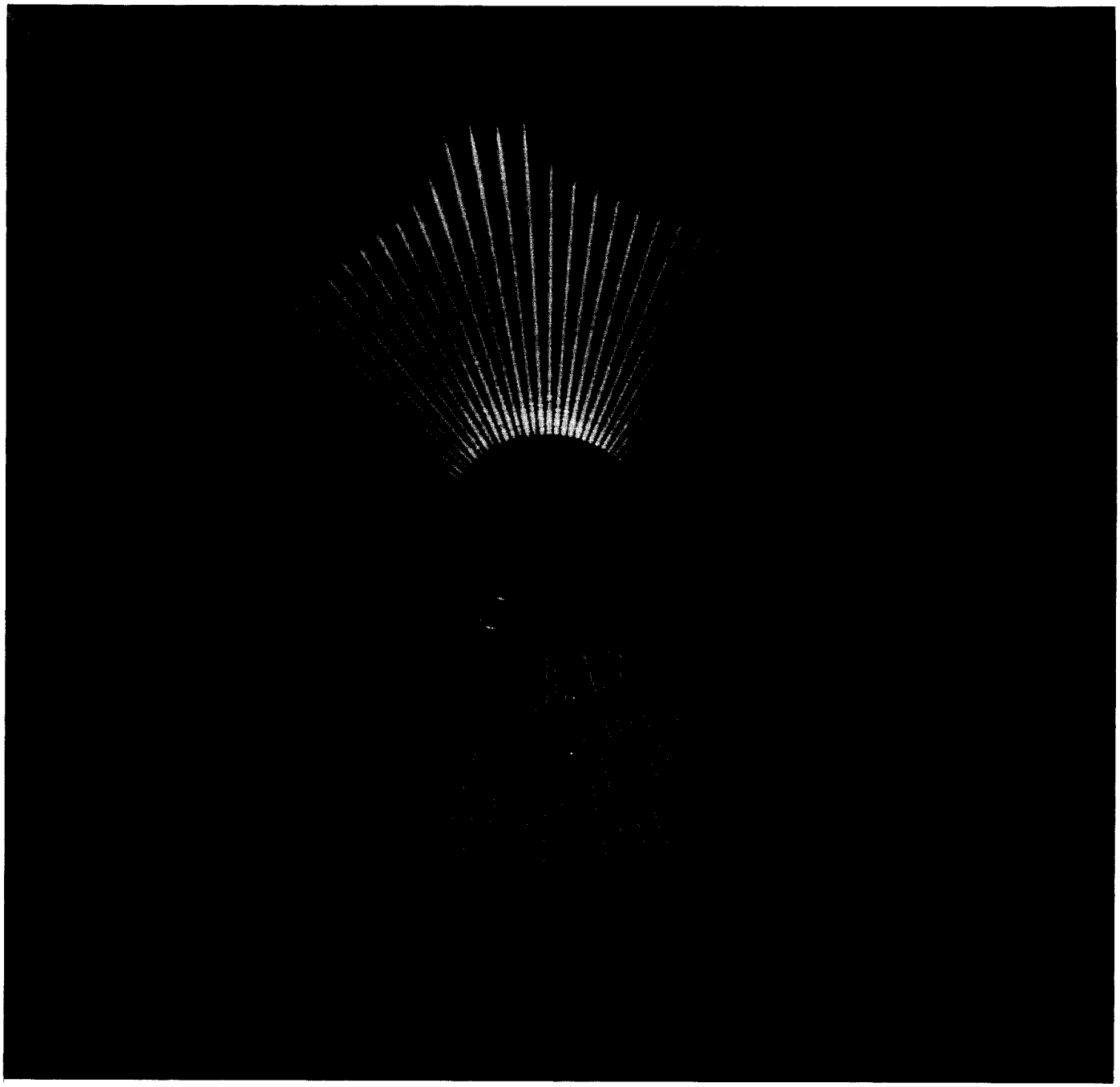

Fig. 15. View of the inside of the molecular trap

UNCLASSIFIED
[redacted]

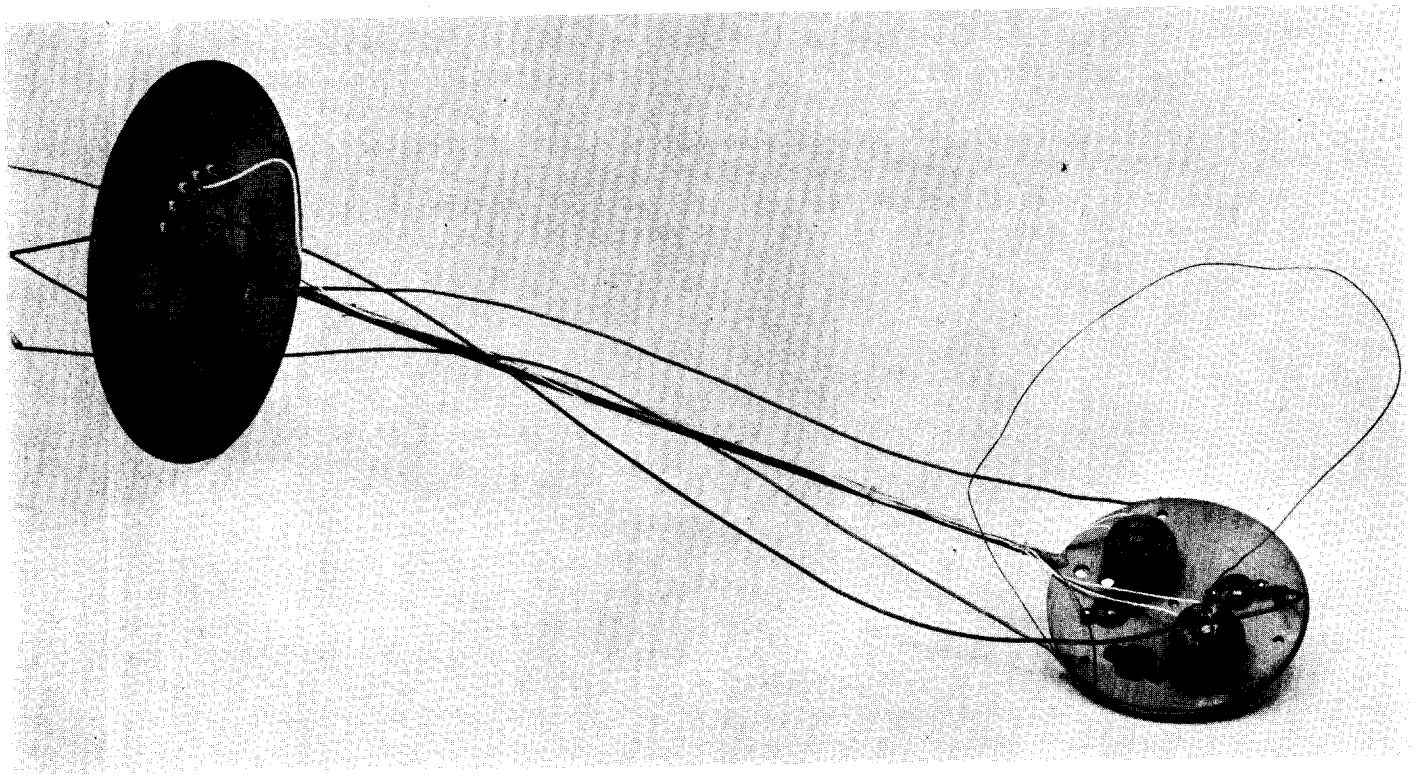

Fig. 16. Solenoid mounting fixture

and provided an accelerated vacuum soak for the solenoid, which helped simulate the effect of the 7½-mo exposure of the flight solenoid to space. The 175°F bakeout temperature did not exceed the maximum rated temperature of the solenoid, which was 257°F. All of the flight solenoid coils had been outgassed at 320°F in an argon atmosphere for 1 hr, and the assembled solenoids at 230°F for 22 hr in a vacuum. At the end of the bakeout period, the chamber cold wall was turned on and cooled down to −210°F. The solenoid temperature was maintained at +14°F by the heater wire. When the cold wall and solenoid had stabilized at their respective temperatures, the solenoid was turned on and the test started.

Two shutter pulsers, which were built for testing the flight shutters, were used to operate the solenoids during the tests. The pulsers used the same shutter drive circuit that was used in the TV camera head. The flight shutter operated at the rate of one exposure every 48 sec. Due to testing time limitations, the solenoids were operated during the tests at an accelerated rate of one exposure per five-second interval. An exposure was two solenoid pulses of 25 msec duration spaced 200 msec apart.

Solenoid operation during the tests was monitored by displaying the coil current on an oscilloscope and periodically observing and photographing the current waveform. Typical current waveforms are shown in Fig. 17. The shape of the waveform was affected by the moving armature, due to the back emf induced in the coil. Basically, three things were determined from the shape of the waveform

(1) That the solenoid moved when pulsed

(2) How fast it moved

(3) Amount of ringing or bounce at the end of the power stroke

The amount of ringing of the armature at the end of the power stroke indicated the amount of friction in the solenoid. That is, a decrease in the amount of ringing indicated an increase in friction. The solenoids were also monitored by listening to their operation, which could be heard outside the chamber. In some tests the solenoids were operated all night. In this situation they were monitored by recording the signal from an accelerometer, which was mounted on the chamber top on a strip recorder. This produced a spike on the strip chart when the solenoid was pulsed.

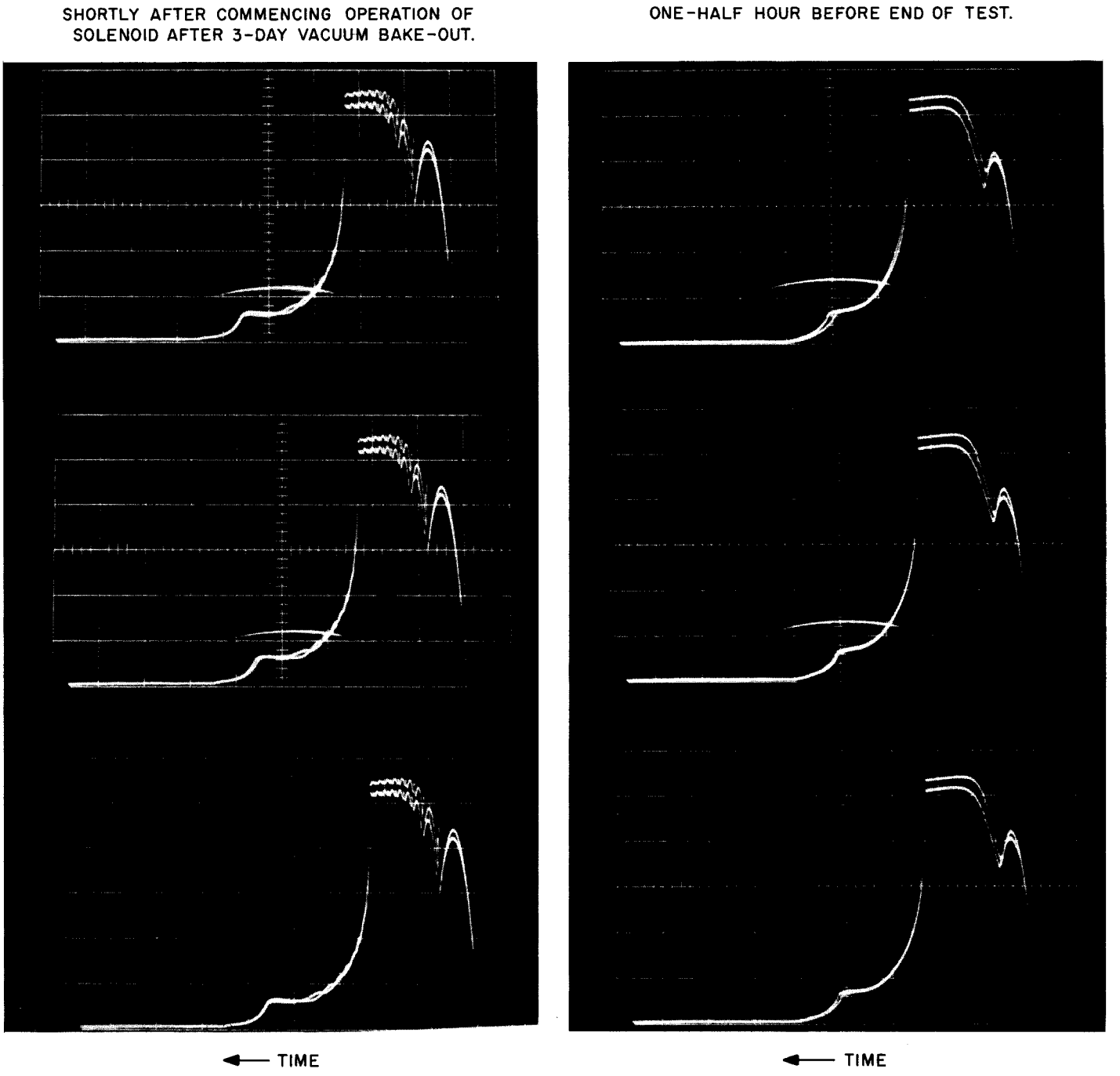

Fig. 17. Solenoid No. 204 coil current during JPL molecular sink testing

e. Solenoid life test results. The results of the solenoid life tests are given in Table 3. The loaded test condition means that the solenoid was tested while assembled in a *Mariner-C* TV shutter. The number of exposures to failure given is the number put on a solenoid during the test. It does not include the pretest run-in exposures. The initial failure occurred when the solenoid first failed to actuate on a pulse. The complete failure occurred when the solenoid failed for several minutes to actuate when pulsed.

f. Conclusions. The tests showed that the solenoids had a considerably shorter life expectancy operating in the molsink than they did operating in air. The operating life of the solenoids tested in air ranged from 16,000–

UNCLASSIFIED

Table 3. *Mariner*-C TV shutter solenoid life test results

Test		Solenoid Serial No.	Date of test	Solenoid test conditions			Number of exposures			Remarks
Type	No.			Temperature, °F	Pressure, torr	Solenoid loading	Before test	To initial failure	To complete failure	
Bench test		217	9/23/64	+75	Ambient	Unloaded	Unused	26,000		The bench tests at ambient conditions were conducted in the Space Optics Group Laboratory. The test of each solenoid was ended after the onset of the initial failure mode.
		223	to			Unloaded	Slightly used	19,000		
		205				Loaded	Unused	16,000		
		213	12/2/64			Loaded	Unused	29,000		
Molesink tests	1	207	6/15/65	+14	4×10^{-8} to 3×10^{-9}	Unloaded	Unused	7,620	9,060	Microscope examination of this solenoid showed evidence of a misaligned armature, which accelerated the abrasion of the solid lubricant in one ball race.
	2	204	6/18/65 to 6/24/65	+14	5×10^{-9} to 3×10^{-10}	Unloaded	1,775		15,000	These two solenoids were mounted on one fixture and operated simultaneously during the test by two shutter pulsers. Solenoid 204 did not fail; the test plan was limited to 15,000 exposures.
		212				Unloaded	Unused	4,000	7,900	
	3	215	6/25/65 to 6/30/65	+14	5×10^{-9} to 3×10^{-10}	Unloaded	1,400	8,340	8,820	The solenoids in this test were mounted and operated in the same manner as in test No. 2.
		221				Unloaded	Unused	11,130	13,890	
	4	201	7/2/65 to 7/7/65	+14	4×10^{-9} to 8×10^{-10}	Loaded	Unused	14,715	17,415	
	5	219	7/8/65 to 7/21/65	+37	3×10^{-9} to 6×10^{-10}	Unloaded	1,440	7,260	19,485	In this test all three of the solenoids were mounted on one fixture in the chamber but only one solenoid was operated at a time.
		220				Unloaded	1,440	14,340	No data	
		224				Unloaded	1,440	10,920	11,040	

29,000 exposures, while the life of those tested in the molsink ranged from 4,000–15,000 exposures.

The type of failure that occurred in the solenoid was a mechanical lock-up between the steel balls and the ball races, which prevented the solenoid from actuating when pulsed. This lock-up was preceded by a decrease in the armature bounce (ringing at the end of the power stroke) and a slowing of the armature movement.

Microscopic examination of three of the solenoids tested to failure in the molsink showed that the solid lubricant had been completely removed from the bottom of the ball races by the abrasive action of the steel balls. It was this complete removal of the solid lubricant, producing metal to metal contact, that was considered to be the cause of the solenoid failure. The solid lubricant appeared to provide adequate lubrication of the solenoids in a high vacuum. There was no difference in operating characteristics of the solenoids when operating in air and when operating in the molsink at the start of the test.

Although the high vacuum in the molsink had no apparent effect on the operating characteristics of any of the solenoids at the start of the test, the lack of absorbed molecules between friction surfaces probably accelerated the abrasion of the solid lubricant from the bearing surfaces. It was speculated that after the bare metal surfaces started to come in contact with one another, a form of microscopic cold welding took place during the vacuum test. This speculation was supported by the fact that when the chamber was back filled with a dry gas, the solenoids then proceeded to operate again. The dry gas may have acted as a separating wedge on the microscopic cold welds. In the case of bench test (ambient conditions) failure, it was presumed that the wear proceeded until sufficient galling occurred to produce a lock-up condition which could not be broken by the pulsing force of the solenoid.

UNCLASSIFIED

F. Propulsion

1. Postinjection Propulsion System: Temperature Effects on Squib Performance

The effect of temperature on squib performance was studied as part of the *Mariner-C* type-approval test program (Ref. 1). A formal report on all phases of the squib-valve test program is in preparation; however, this article is being published now because of its applicability to current sterilization studies.

Thirteen *Mariner-C* gas generator electroexplosive squibs[1] (Fig. 18) were subjected to time-temperature cycling followed by functional testing. Twelve squibs were arranged into groups each of which contained three units for exposures at 200, 250, 300, and 400°F, with times being varied for 6, 12, or 48 hr. One squib was exposed to 300°F for 192 hr. Complete test results are contained in Table 4. The squib firings were conducted while at temperature in fixed-volume bombs with internal volumes of 0.0927 in.^{3} (maximum). Fig. 19 represents a typical firing trace obtained from the bomb. The top trace displays an overall indication of the squib output pressure, while the two lower traces display the leading segment of the pressure trace and the firing current trace, respectively, but with a shorter time base.

[1]JPL Drawing No. J 4700697, Hi-Shear Corp., Torrance, Calif.

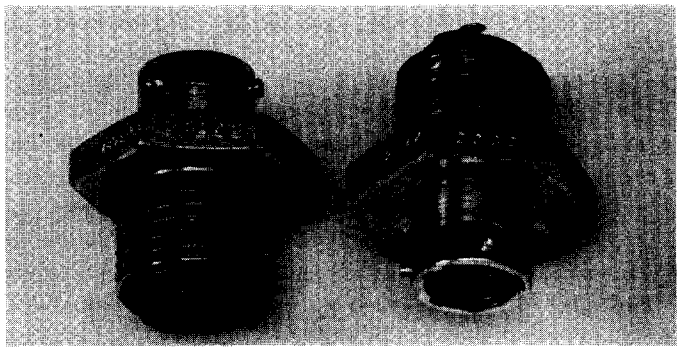

Fig. 18. *Mariner-C* explosive valve squibs

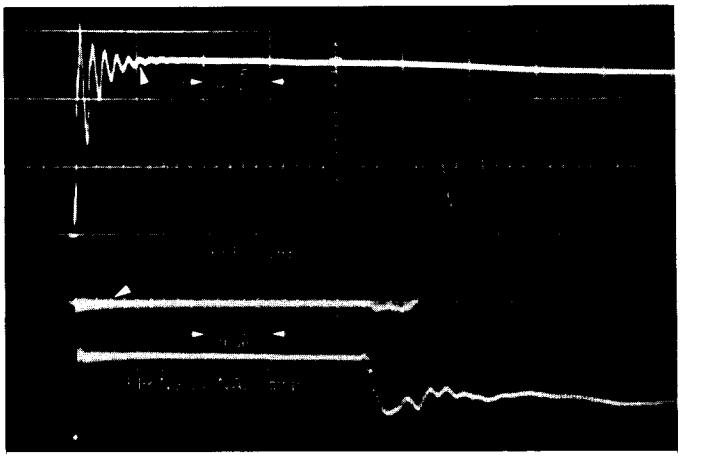

Fig. 19. Oscillograph of typical squib firing parameters

A dynamic form of a squib tester (Fig. 20) was developed to simulate the operation of an explosively-actuated device more realistically than did the static test bomb and in addition, to provide a measurement of the squib total energy output. In operation, a squib is fired against a piston which in turn is connected to a liquid shock spring to take up the load. A total force transducer measuring the output force, together with a linear displacement transducer to measure piston travel, provides the total output energy curve. Fig. 21 represents the method of attaining the total energy and Fig. 22 shows an actual trace. One squib was exposed at 400°F for 4 hr, allowed to cool to room temperature, and then fired in the dynamic tester. Table 5 compares the data from this

Table 4. Test results from squib firings in bombs

Serial number	Test temperature, °F	Exposure time, hr	Maximum current, amp	Pressure rise time, msec	Time to maximum pressure, msec	Maximum pressure, psi
20671	200	6	8.0	0.14	0.84	18,000
20656	200	12	8.2	0.06	0.38	16,500
20833	200	49	8.2	0.06	0.48	12,000
20649	250	6	8.0	0.20	0.86	20,000
20742	250	12	10.0	0.14	1.02	12,200
20679	250	48	8.3	0.12	1.04	19,000
20682	300	6	8.5	0.12	0.76	20,000
20646	300	12	8.3	0.13	0.95	18,000
20825	300	50	8.3	0.12	1.22	19,000
20748	300	192	8.5	0.03	0.36	23,000
20792	400	6	8.5	1.25	1.45	17,500
20764	400	12	8.4	2.14	3.00	15,000
20757	400	48	9.0	0.20	1.30	20,000

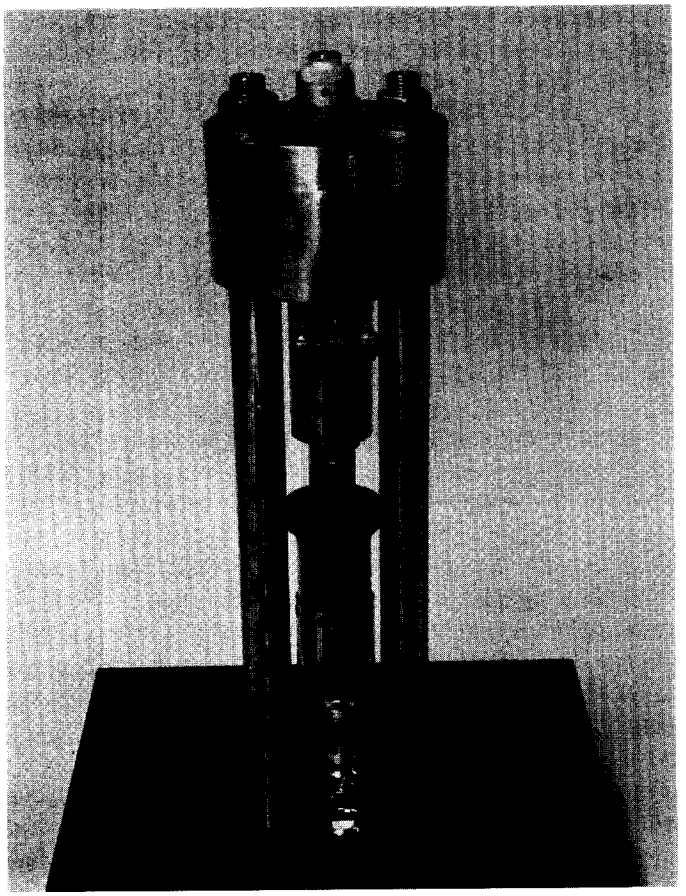

Fig. 20. *Mariner*-C dynamic squib tester assembly

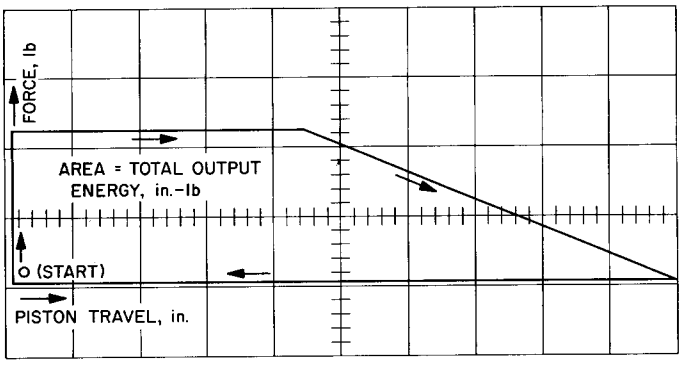

Fig. 21. The method of obtaining total energy

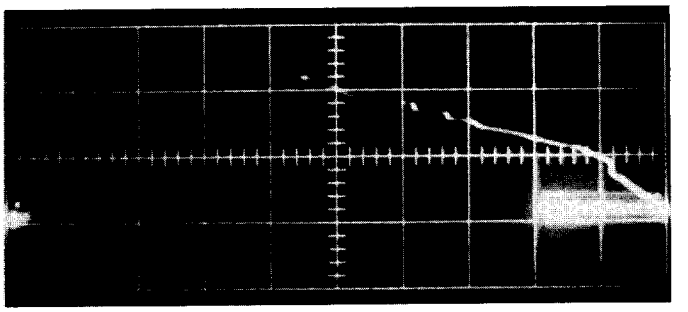

Fig. 22. Actual trace of total energy

test with those of a similar squib having only an ambient temperature history.

The current technology of electroexplosive production squibs is such that individual performance variations are expected even within the same batch, and this fact is evident in the results. The one important conclusion that may be drawn from these limited tests is that the subject squib is capable of satisfactory operation after temperature exposure at 300°F and as high as 400°F. The effects of several short cycles are expected to be no more severe than those of the single longer cycles reported herein.

Table 5. Test results from dynamic tester firings

Serial number	Exposure		Maximum current, amp	Pressure rise time, msec	Time to maximum pressure, msec	Maximum pressure, psi	Maximum force, lb	Total energy, ft-lb
	Temperature, °F	Time, hr						
25193	Ambient	—	7.0	0.16	0.70	9000	1600	800
20815	400	4	7.5	0.12	1.32	8900	1700	1230

Reference

1. Jet Propulsion Laboratory, *Design Specification, Mariner-C Flight Equipment, Explosively Actuated Valve Assemblies,* Specification MCE-33192-DSN-A, Jet Propulsion Laboratory, Pasadena, July 30, 1964.

II. *Voyager* Project

A. Introduction

1. Objectives

The primary objective of the *Voyager* project is to carry out scientific investigations of the solar system by instrumented, unmanned spacecraft which will fly by, orbit, and/or land on the planets. Emphasis will be placed on acquisition of scientific information relevant to the origin and evolution of the solar system, the origin, evolution, and nature of life, and the application of this information to an understanding of terrestrial life. The primary objective of the *Voyager* mission to Mars, beginning in 1971, is to obtain information relative to the existence and nature of extraterrestrial life, the atmospheric, surface and body characteristics of Mars and planetary environment by performing a series of integrated missions beginning in 1971 performing unmanned experiments on the surface of, and in orbit about the planet. For the 1971 missions, primary emphasis will be placed on the orbiter, with engineering capsule tests or probes to be included if possible. The first capsule missions to conduct scientific experiments on the surface will be scheduled during the 1973 opportunity.

A secondary objective is to further our knowledge of the interplanetary medium between the orbits of Earth and Mars by obtaining scientific and engineering measurements from the spacecraft while in transit.

2. Project Plan

All *Voyager* missions will be conducted as events of an integrated program in which each individual flight forms a part of a logical sequence in an over-all technical plan of both lander and orbital operations. The *Voyager* design will provide for the carrying of large scientific payloads to the planet, the telemetering of a high volume of data back to Earth, and long and useful lifetimes in orbit about the planet and/or on the planetary surface. Hardware will be designed to accommodate a variety of spacecraft and/or capsule science payloads, mission profiles, and trajectories. Particular emphasis will be given to simple and conservative design, redundancy wherever possible, and a comprehensive program of component, subsystem, and system testing.

Overall direction and evaluation of the *Voyager* project is the responsibility of the Office of Space Science and Applications (OSSA) of the National Aeronautics and Space Administration (NASA). Management of the *Voyager* project and implementation of selected systems is the responsibility of the Jet Propulsion Laboratory of the California Institute of Technology.

a. Technical description. Two *Voyager* planetary vehicles are to be designed, constructed, and tested for launch on a single Saturn V during the 1971 Mars opportunity. Attention is also being given to requirements imposed on such vehicles by similar launches subsequent to 1971, such as missions planned for 1973 and 1975. Each

planetary vehicle is to consist of a flight spacecraft and a flight capsule, although in 1971 the capsule will be limited to a nonsurviving test capsule or atmospheric probe. The spacecraft bus with its several hundred pounds of science payload will weigh approximately 2,500 pounds, its retropropulsion subsystem may additionally weigh up to 15,000 pounds, and the flight capsule will be under 3,500 pounds. The flight spacecraft will be a fully attitude-stabilized device utilizing celestial references for the cruise phase, and will be capable of providing velocity increments for midcourse trajectory corrections and for Mars orbit attainment by both the spacecraft and the capsule. Onboard sequencing and logic will be provided, as well as ground command capability.

The spacecraft will supply its own power from solar energy or from internal sources and will be capable of maintaining radio communications with Earth. In addition, the spacecraft will be thermally integrated and stabilized and will monitor various scientific phenomena near Mars during transit and will telemeter this information back to Earth; it will also monitor and telemeter data pertaining to spacecraft operation. The flight spacecraft will also provide the flight capsule with services such as power, timing and sequencing, telemetry, and command during the transit portion of the missions, and it may also serve as a communications relay. The sterilized flight capsule will be designed for separation from the flight spacecraft in orbit, for attaining a Mars trajectory, for entry into the martian atmosphere, descent to the surface, and (by 1973) impact survival, and for surface lifetimes of as much as 6 mo. The flight capsule will contain the power, guidance, control, communications, and data handling systems necessary to complete its mission.

No deep space flight tests of the flight spacecraft are planned, and compensation by more extensive ground tests will be attempted to the extent possible. The test program for the flight capsule, which may include Earth-entry flight tests on an *Atlas* or smaller launch vehicle, will investigate entry, descent, impact, communications, and sterilization.

b. Sequence of events. The project plan is being implemented as follows:

Initially, Mission Engineering studies were undertaken to derive a model sequence of *Voyager* missions over several planetary opportunities. This model was to serve as the criterion for the design of the 1971 *Voyager* mission. On the basis of the 1971 mission specification, spacecraft system analyses and tradeoff studies were performed during phase IA both by JPL and by its spacecraft contractor to assess the requirements and constraints imposed on the spacecraft by the mission objectives and by the other systems and elements of the project. With the project approval document revision of October 19, 1965, from use of the *Saturn IB/Centaur* launch vehicle to the use of *Saturn V*, this effort is being reviewed and modified, with the three spacecraft contractors being given phase IA extensions. After completion of preliminary designs, a single spacecraft phase IB contractor under JPL technical direction will be selected to refine the preliminary designs and functional descriptions developed earlier, and to develop system and subsystem functional specifications. Selected subsystem hardware will be breadboarded and tested. In addition, the contractor will prepare for JPL approval detailed plans covering management and implementation of the development, fabrication, test, launch, and test operations efforts to be undertaken during phase II.

B. Guidance and Control

1. Voyager Central Computer and Sequencer

a. Introduction. This article describes the results of a study task to develop a central computer and sequencer (CC&S) suitable for the *Voyager* spacecraft "baseline" design. The design presented here is the result of several iterations of "timer oriented" and "memory oriented" designs. (See *SPS 37-31*, Vol. IV, p. 45, for definitions and discussions of timer oriented and memory oriented CC&S's.) The timer oriented versions were ruled out early due to a major effect of relatively minor changes in functional requirements. The requirements for the CC&S were negotiated with the guidance and control (G&C) *Voyager* project section and are documented in the baseline design document.

b. General characteristics. The *Voyager* CC&S consists of a memory unit, arithmetic and control logic, maneuver duration and input decoding units. Fig. 1 is a block diagram of the system. The salient features of a two address system and a single address system were incorporated utilizing magnetic elements where possible to mechanize the dynamic logic.

Two destructive readout (DRO), random access, coincident current memories (each consisting of one hundred and twenty-eight 21-bit words) are used. The

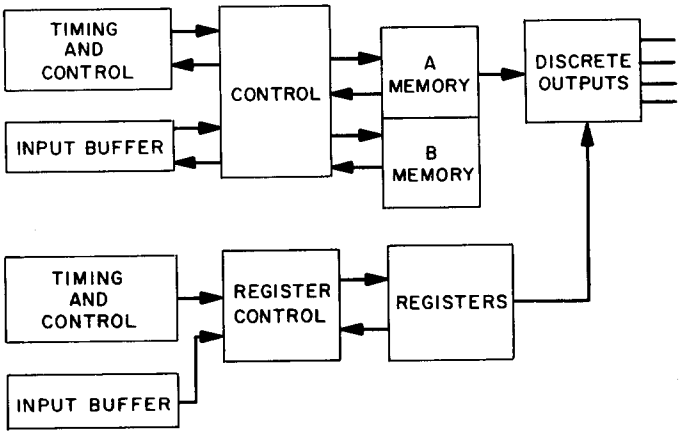

Fig. 1. Block diagram of CC&S system

memories are processed in a serial bit read/bit write manner. The B memory contains the program, and the A memory contains the discrete times. Constants may appear in either memory.

Both internal and external interrupts are available for RF modification of the program and/or the initiation of special sequences, such as midcourse and retro. The extensive use of magnetics provides a fairly low power consumption (7-w dc) and a system impervious to power dropouts.

Word format. Fig. 2 shows the formats of the instruction, time and data words. Bits six and fourteen are logical timing bits.

Instruction list. The instruction list was chosen, first to satisfy the present requirements of the *Voyager* mission (time dependent discrete events, midcourse, retro and capsule release maneuvers, linear and polynomial curve

INSTRUCTION

BIT No.	1 ← → 5	6	7 ← → 13	14	15 ← → 21
	OP CODE		A MEMORY ADDRESS		B MEMORY ADDRESS

TIME

BIT No.	1 ← → 13	14	15 ← → 21
	TIME MAGNITUDE		EVENT ADDRESS

DATA

BIT No.	1 ← → 13	14	15 ← → 21
	ANYTHING		ANYTHING

Fig. 2. Instruction, time, and data words formats

fitting), and second to offer sufficient flexibility to cover some anticipated changes of reasonable complexity in requirements. Table 1 presents the instruction list with descriptions of each operation.

Maneuver duration. The midcourse and retromaneuver sequences are processed by a subsystem that is independent of the main part of the CC&S. There are two basic reasons for this. First, since these two sequences are the most critical in the mission and are not readily accessible for radio command back-up, it is felt that by performing them in a separate subsystem a more complete redundancy scheme can be applied without its having to embrace the entire CC&S. Second, independent registers would be required for the motor burns in any case because the processing speed of the memory is not fast enough to handle the expected accelerometer pulse rates. The subsystem to be described is basic. No redundancy has been applied, as the form of the redundancy has not been decided upon. The requirements on the subsystem are the same as those demanded in *Ranger* and *Mariner*. They are

(1) Command the spacecraft to switch from fixed sensor to gyro stabilization.

(2) Command the spacecraft to perform pitch and roll turns of predetermined durations.

(3) Command the spacecraft motor to burn for a predetermined duration.

(4) Command the spacecraft to switch back to sensor stabilization.

c. Logical mechanization. The choice of logical mechanization is based on a number of factors.

(1) It must satisfy the presently known *Voyager* functional requirements.

(2) It should have growth potential so that more complex functions can be accommodated with only minor modifications to the equipment.

(3) The mechanization should be relatively simple so that functional changes that may arise in the future can be more readily assessed as to their impact on the subsystem design.

(4) The system should be as immune to power dropouts and line transients as possible with loss of time being the only type of error permitted.

These factors have led to the selection of a dynamic mechanization based on the type of circuitry used in the

UNCLASSIFIED

Table 1. The instruction list with operation descriptions

No.	Operation	Symbol	Description	No.	Operation	Symbol	Description
1	Add	Add	Add the contents of A memory to the contents of B memory and place the sum in the B memory. Step PC by one for the next instruction.	9	No operation	NOP	No operation performed. Step PC by one for the next instruction.
2	Subtract	Sub	Subtract the contents of the A memory from the contents of the B memory and place the difference in the B memory. Step PC by one for the next instruction.	10	Program stop	NON	Resets scan control. Stops clock. The B address of the instruction word is loaded for the location of the next instruction when scan is resumed.
3	Decrement A by one	SRA_{123}[a]	Decrement bits 1–13 of the contents of the A memory and check for zero. If zero: Step PC by one for the next instruction, decode the event address and fire event. Nonzero: Jump to B address of instruction word for the next instruction.	11	Address modification	DEC	Decrement bits 7–13 of the B memory by one. Step PC by one for the next instruction.
4	Decrement A by one	SRA_x	Same as 3, except on zero this instruction is cleared to all zeros.	12	Compare	CMP	Compare the contents of the A memory to the contents of the B memory. If $=$: Step PC by one for the next instruction. If $\neq$: Step PC by two for the next instruction. The contents of A and B are recirculated.
5	Transfer A to B	XBA	Transfer the contents of the A memory to the B memory, recirculating the contents of A. Step PC by one for the next instruction.	13	Load	LD	Interrogate the input decoder for a ready signal. If ready, load address register and memory location selected by input decoder and step PC by one for the next instruction. If not ready, step PC by one for the next instruction.
6	Transfer B to A	XBA	Transfer the contents of the B memory to the A memory, recirculating the B memory. Step PC by one for the next instruction.	14	Jump if flag is set	JMF	Interrogate sensor flag. If set: Jump to B address of instruction word for the next instruction.
7	OP code modification	XOP	Transfer bits 1–5 of the A memory to bits 1–5 of the B memory, recirculating A. Step PC by one for the next instruction.	15	Extract	EXT	Load the contents of the A memory into the buffer register and send ready signal to appropriate subsystem. Contents of A are recirculated. Step PC by one for the next instruction.
8	Jump	JMP	Unconditionally jump to the B address of the instruction word for the next instruction.				

[a] Resolution subscripts:
1 = 1 pps
2 = 1 ppm
3 = 1 pph

Ranger, *Mariner C* and, most recently, in the *Mariner* 1966 systems.

Two memories are used in this system. This was done to remove the necessity of providing external registers such as a transfer register and an accumulator. It also permits a memory cycle to be completed in two phases instead of three. The memories are labeled A and B on the block diagram. The B memory contains the program and constants and the A memory contains time, data words and constants. Communication between the two memories is effected through the use of the transfer instructions XAB and XBA.

Bit timing for the memories is generated by a two-by-twenty-one way current steering switch that is driven by a 2.4-kc scan clock. The enabling of the scan clock is under control of the program and the scan control logic. The scan rates employed are once a second, once a minute and once an hour. The rates selected have been based on the required resolution of time dependent events for different phases of the flight.

A scan, in this system, consists of processing the program pertinent to a given phase of the flight. Since the program changes, depending on the phase of the flight, the time required for its processing varies. Typically, a scan takes a few tenths of a second. The rate at which these scans occur depends on the program. For example, if during the preceding scan an SRA_2 were encountered, this information would be stored in the scan control logic, and the next scan would be initiated on the next one-minute pulse.

UNCLASSIFIED

The purpose of all this is to minimize the operating time of the system. The advantages obtained are twofold. First, the chance of introducing errors is reduced; and second, a considerable savings in power is realized. For example, the power required between scans is approximately 1 w while during a scan the power required can be as high as 7 w. These advantages are most easily seen by considering the cruise phase of flight where the system is required to operate only a few tenths of a second each hour.

As mentioned previously, this system can require two phases to process an instruction. In the first phase the operation is decoded, and the address of the memory location or locations to be operated on is established. In the second phase the operation selected is performed. Some of the operations require only the first phase to process. These operations are mainly concerned with the program and are not associated with time or data words. These operations are jump (JMP), program stop (NON), processing an SRA command at the wrong flag (SRAWF), load (LD) and jump on sensor (JMF). The last two operations are conditional and may require phase one and phase two. For example, the LD operation will require two phases if it finds that the input buffer has received information from the command system.

Referring to the instruction word it is seen that bits seven through thirteen contain the A address and bits fifteen through twenty-one contain the B address. Depending on the operation code the address in B may or may not be the source of the next instruction. If the address selected in B is that of a data word or a constant, then the address of the next instruction must be obtained from a program counter (PC). For example, the ADD operation requires that the contents of the location specified by the A address be added to the contents of the location specified by the B address. Here the B address has no relation to the next instruction.

The program counter is read out at the same time as the B address (bits fifteen through twenty-one), and for all two-phase operations it is decremented (reduced in magnitude by one) in phase one in anticipation that the address of the next instruction is the next word in the B memory. This is the case for all operations except the SRA and CMP where it is conditional on the results of the operation being performed. If the instruction is a JMP, NON, SRAWF or SF, then the B address is inserted into the PC and the B address register at the same time during phase one. In this way the PC always contains the address of the next instruction.

RF access to the memory is through the input buffer where the word is verified and then passed on to the memory for action. The process is as follows: the word is transmitted from the ground station, processed by the command decoder subsystem and stored in the input buffer. The complement of the word is then transmitted from the ground station—going through the same processing—and presented by the command decoder on a separate line. This word is compared bit by bit with the contents of the input buffer. If a comparison is achieved, a signal is sent to the scan control logic that a verified word exists in the input buffer. A scan is initiated the next second, and when the LD instruction is reached in the program the word is entered into memory. Another scan is initiated 1 sec after the completion of the load scan. If no comparison is reached a signal is sent to the telemetry system which informs the ground station that the comparison has failed.

Outputs from the system include up to one hundred and twenty-eight event actuations, a 1-pps signal sent to the telementry system, and a time-tag word. The time-tag word is entered into an output buffer every hour. It contains the day and the hour in the day. Once the time-tag word is in the buffer a signal is sent to the user indicating that the time tag is available. The user then sends shift pulses and shifts the word into his equipment as required.

The maneuver duration subsystem consists of a frequency divider (or clock), an input decoder, seven linear feedback shift registers, shift register sequencing circuitry, and the necessary actuator outputs. Information is sent from the ground station through the spacecraft command decoder to the input decoder. The input decoder determines which of the registers is to be loaded and routes the information accordingly. A parity check is made on the information as it is being processed. If parity is correct a signal is sent to telemetry where it is transmitted to the ground. After the registers have been loaded a discrete command is sent through the command decoder to start the sequence. This command may be start midcourse or start retro. Upon receipt of this command a gate is opened permitting a 2.4-kc signal to be applied to the input of the frequency divider. One hour later the roll-turn register is turned on and "start roll" is commanded. The register is shifted at a 1-sec rate, and when it overflows it generates a "stop roll" command, shutting off the roll register and starting a fixed 4-min counter. When the 4-min counter overflows it starts the next event in the sequence. When the last event in the sequence has occurred the gate controlling the 2.4-kc signal to the frequency divider is closed.

UNCLASSIFIED

As many maneuvers as desired may be performed, as the subsystem automatically resets itself after the last event has occurred. For example, to perform a second midcourse all that is necessary is that the registers be reloaded and another discrete start command be sent.

d. Programming. There are a few restrictions to observe in the programming of the *Voyager* CC&S.

(1) An LD instruction must occur in each scan.

(2) Each scan must end with a NON.

(3) The total scan time must be less than the established scan rate.

Programs of "assumed" missions indicate that the instruction list chosen is more than adequate and that the memory size is adequate. Should more storage be required, increasing the number of words in the memories is not an insurmountable problem. Figs. 3–5 are timing diagrams for an assumed mission.

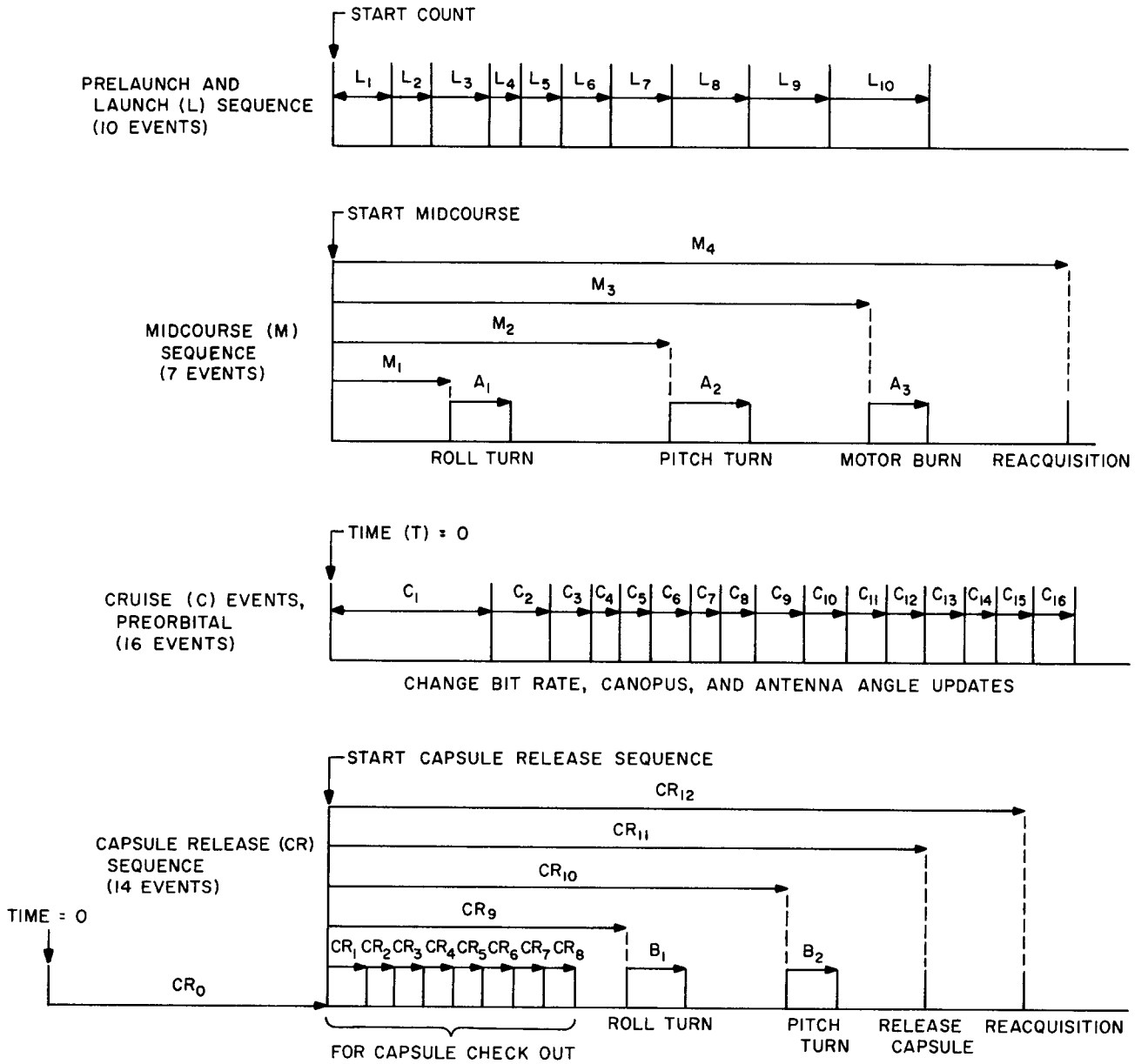

Fig. 3. Discrete events for typical program—standard launch, midcourse, and cruise

UNCLASSIFIED

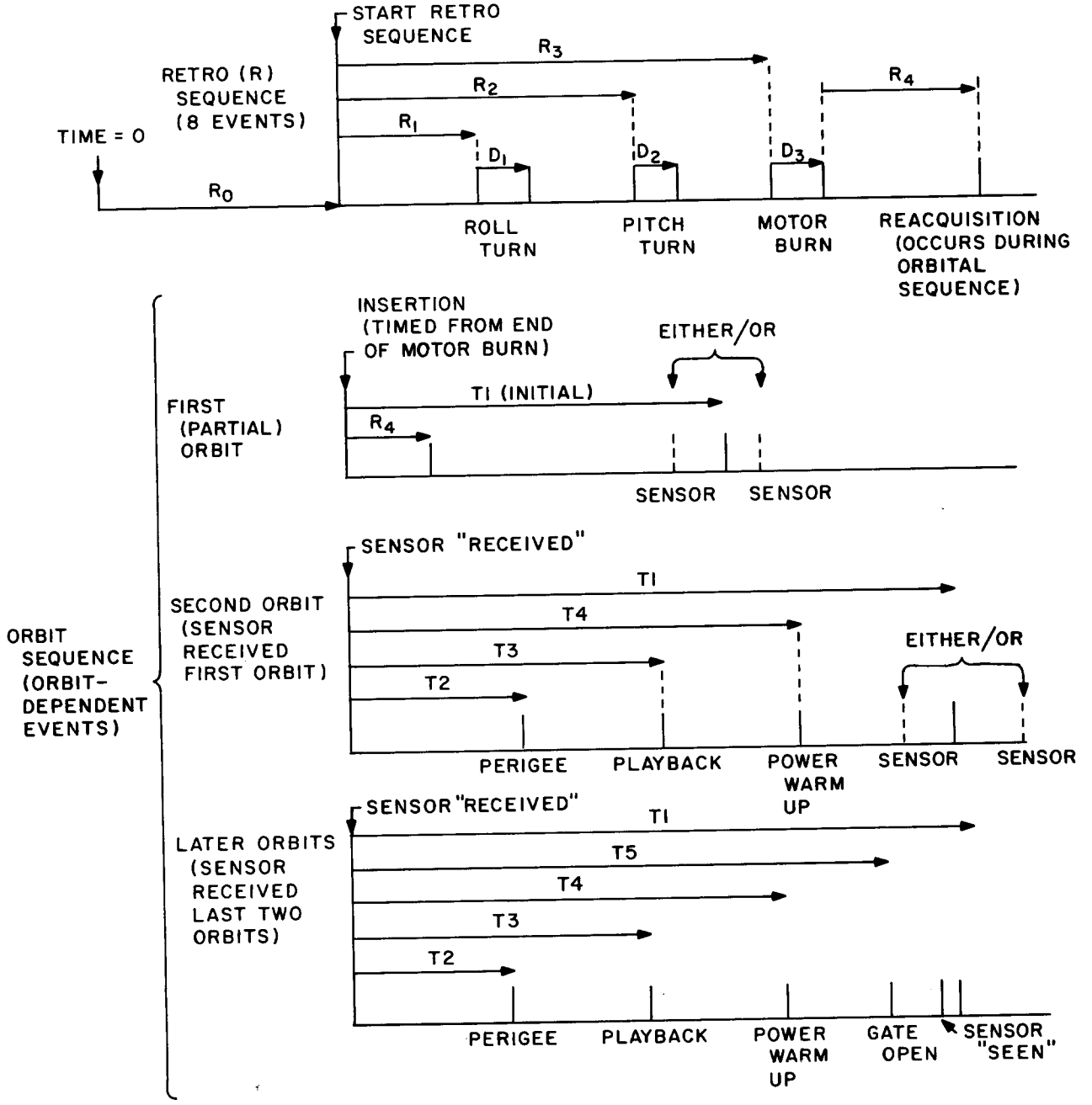

Fig. 4. Orbit sequence for a typical program

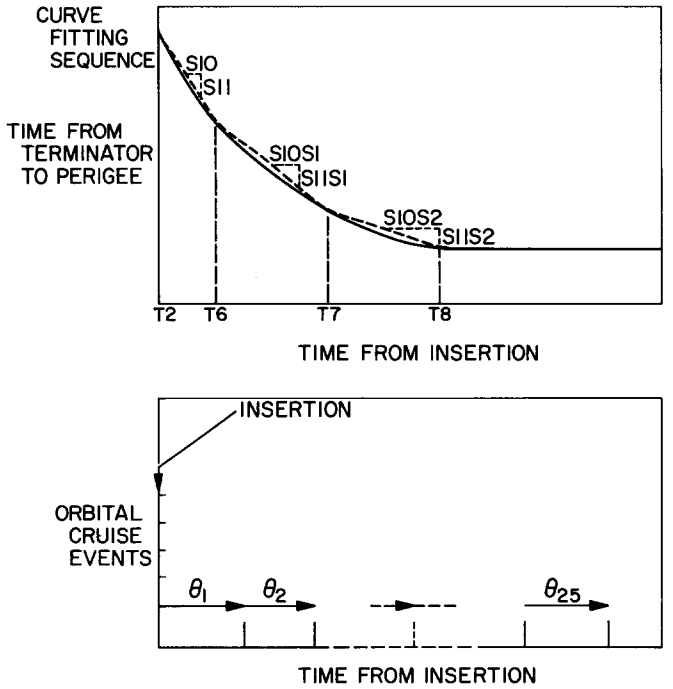

Fig. 5. Example of curve fitting terminator sensing

e. Physical characteristics. Based on the maximum use of three-dimensional cordwood packaging techniques in standard $1.6 \times 6 \times 12$ in. subchassis the following estimates can be made. (128 outputs are assumed, each a relay and a driver.)

Weight 35 lbs

Volume 575 in.^{3}

Components

Magnetic ferrite switch cores = 7000

Semiconductors, resistors, capacitors, relays, etc. = 4500

2. Spacecraft Power

In support of the *Voyager* project, the JPL Spacecraft Power Section will perform a number of task assignments. These task assignments have two main purposes

(1) To investigate in detail those areas of power system design that are of particular interest for the *Voyager* mission.

(2) To provide a reservoir of information on power system components and technology that could be of value to the *Voyager* project.

To date, a total of six task assignments have been undertaken. One task, a study of solar cell array performance on the surface of Mars, has been completed. The remaining five tasks divide roughly into the areas of energy storage, energy sources, power conditioning, power system design, and *Voyager* contractor support. To carry out the work called for in the tasks, each task has been divided into a number of subtasks, each subtask being a logical and complete part of the larger task. The output of the subtask is a report, written in the form of an engineering memo and containing enough information to be complete in itself.

In order to assess progress in carrying out the task assignments, each subtask is scheduled on a bar chart that runs through fiscal 1966. These charts clearly state the point in time at which each subtask is initiated, the dates of interim reports, the date of the final report, the amount of time to be spent on the task and the individual or individuals responsible for carrying out the work. This method of control allows problem areas and schedule slips to be revealed early enough to take corrective action.

To date, the following subtasks have been started

(1) A review of the *Mariner-C* power system detailed design in order to avoid repeating the design weaknesses on *Voyager.*

(2) A parametric analysis of the effects of power subsystem frequency, voltage regulation, input voltage range, output power and voltage on such parameters as weight, reliability and efficiency.

(3) An analysis of the problem of providing increased power conditioning equipment reliability using redundancy, load switching, fault sensing and cleaning, etc.

(4) An analytical comparison of the advantages and disadvantages of down-regulating switched regulators and booster regulators (the type used on *Mariner-C*).

(5) The acquisition and correlation of parametric performance data on silver-zinc, silver cadmium and nickel cadmium batteries.

(6) Presentation of parametric performance data on new solar cell types and an analysis of their possible usefulness to the *Voyager* project.

(7) An investigation of the advantages and disadvantages of using a *Mariner-C* power system mechanization method for the *Voyager* bus.

(8) A review of the methods used in establishing power subsystem design margins and recommendations for margin allotments in the *Voyager* program.

UNCLASSIFIED [redacted]

(9) Parametric design – on a functional block level – of power systems for various power levels.

All the above subtasks are proceeding satisfactorily. Outputs are expected in sufficient time to be of value in the *Voyager* bus phase 1B contract efforts. Work on other subtasks will be started as the above listed subtasks are completed.

3. Voyager Gyro Survey

One current activity in support of the design of both the *Voyager* spacecraft and the landing capsule guidance system is being provided by an in-depth survey and study of gyros which might be applicable to this system. The main criteria for studying a gyro in this survey is that it must be a miniature floated rate integrating type. Both ball bearing and gas bearing designs, as well as wide angle, low gain and narrow angle, high gain types will be considered.

The products of six companies are known to fall with the above criteria. The latest up-to-date material on the gyros produced by these vendors is being obtained, and will be analyzed to determine the values obtainable for performance, environmental capability, and predicted life.

The information obtained will be used to make comparisons and to study tradeoffs between the different gyros under consideration. It is also intended that this study shall include a detailed analysis of problems associated with the gyro control assembly used in the *Mariner-C* system as well as a consideration of possible improvements for use in *Voyager*. The present time schedule for this effort calls for the final report to be completed by January 31, 1966.

C. Telecommunications

1. Omnidirectional Antenna

a. Introduction. The low gain antenna (Fig. 6) which is being considered for use in the *Voyager* project was developed by the JPL Spacecraft Antenna Systems Group for *Mariner IV*. The antenna, for discussion, can be considered in three basic parts

(1) *A circular waveguide (Fig. 6).* This waveguide serves as a low loss transmission line between the circular polarized source, and the antenna aperture, and simultaneously provides a means of separating the aperture from the spacecraft for minimum illumination of the spacecraft.

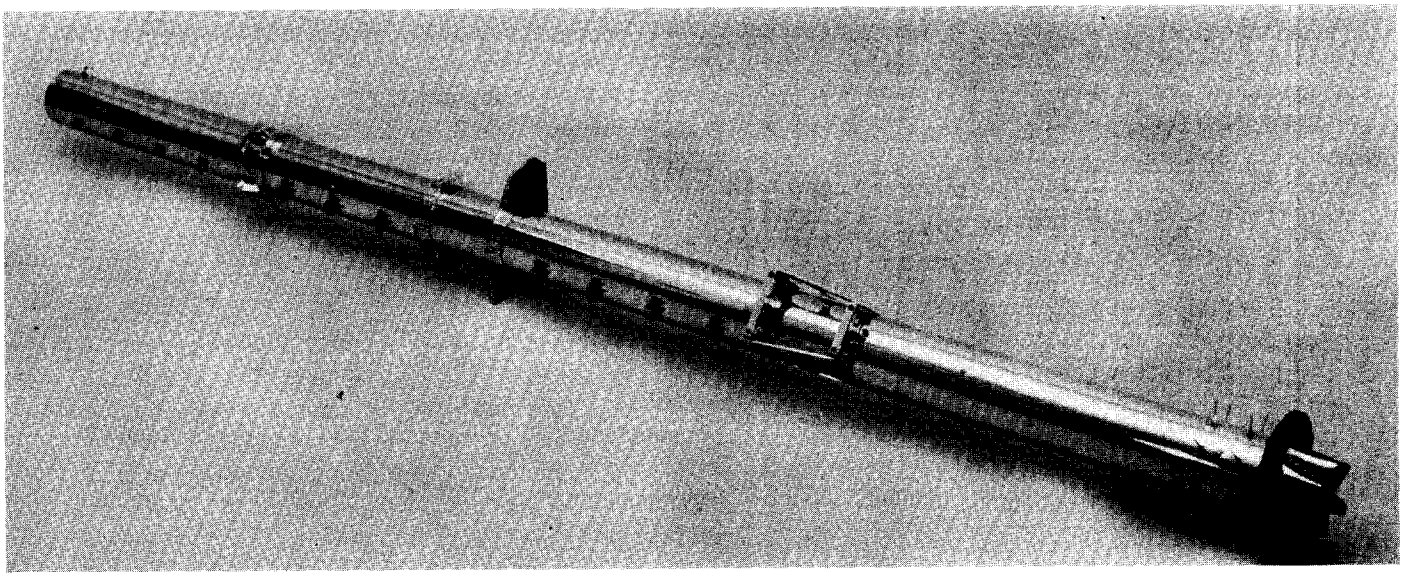

Fig. 6. *Mariner*-Mars low gain antenna

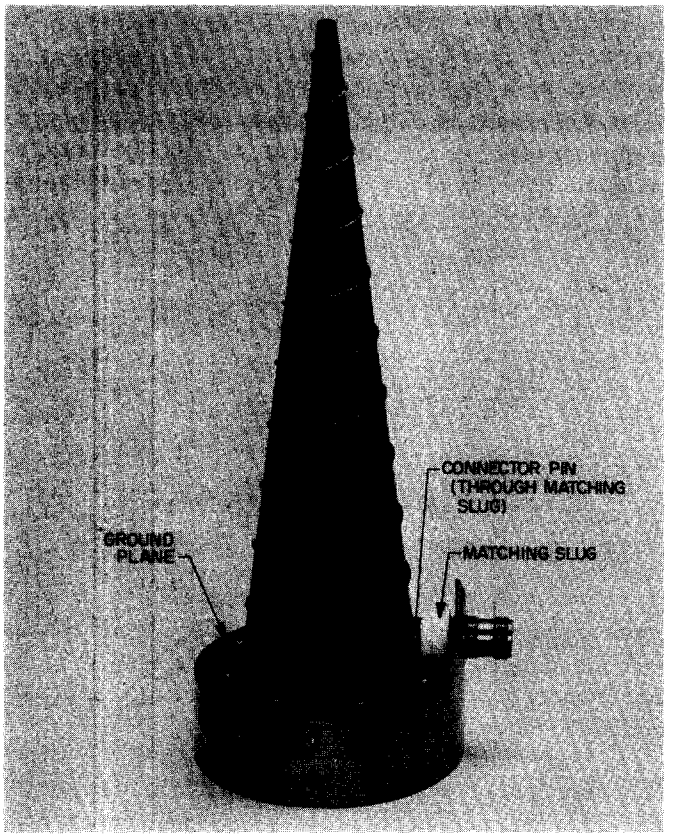

Fig. 7. Low gain antenna feed

(2) *A helical antenna feed (Fig. 7).* The feed is used to convert from the coaxial transmission line mode to a circularly polarized TE_{11} circular waveguide mode.

(3) *A crossed slot crimped aperture (Fig. 8).* The aperture with associated ground plane and reflectors provides the required basic pattern and gain characteristics.

Although the low gain antennas which flew with *Mariner III* and *IV* were flight worthy in both a mechanical and electrical sense, they were, so to speak, "custom made." Philco Corporation performed the fabrication and testing and found that components, such as the helical feed (Fig. 8), supposedly interchangeable from antenna to antenna were indeed not interchangeable, as evidenced by an inability to meet electrical test specifications from antenna to antenna. A subsequent testing program was initiated by Philco to determine the dispersions in electrical performance by testing a particular feed in various circular waveguides and antennas and vice versa. The variations associated with the on-axis ellipticity ratio RHCP/LHCP illustrated by Fig. 9, is a case in point and

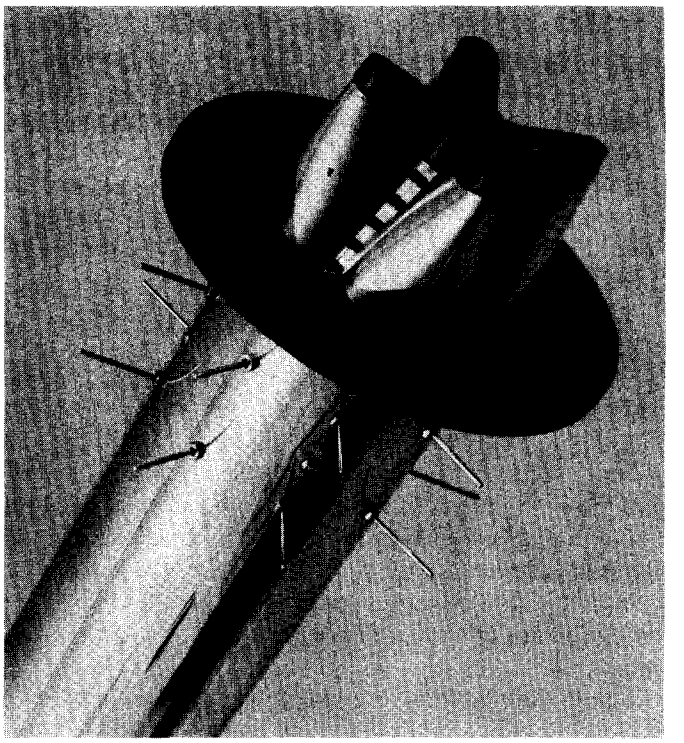

Fig. 8. Crimped aperture and reflectors

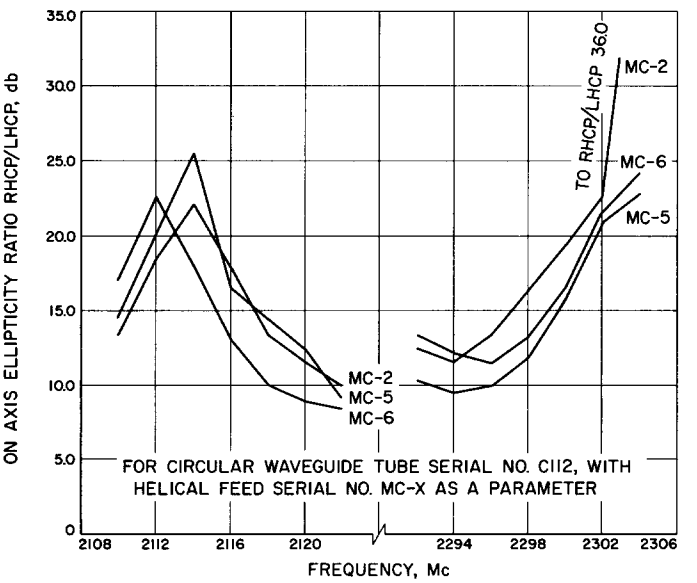

Fig. 9. Helical antenna feed axial ratio dispersion

seems to indicate that tighter mechanical tolerances or design modifications could eliminate this unpredictable type of performance.

b. Tolerance study effort. As a first course of action towards a solution to this electrical performance problem,

an investigation was made at JPL which looked into the existing mechanical tolerances placed on the helical feed. The feed, due to its many parameters (Ref. 1), was suspected as a critical area. Inspection of the fabrication drawings showed relatively tight tolerances already in existence in the critical area. For example (Fig. 7)

(1) Coax pin connector height above ground plane ± 0.002 in.

(2) Length of matching slug ± 0.005 in.

(3) Pin connector length ± 0.005 in., diameter ± 0.002 in.

(4) Helix wire diameter ± 0.003 in.

(5) Cone wall thickness ± 0.004 in.

There exists the possibility of altering some of the original dimensions and tightening tolerances. A tolerance and dimensions study, however, seems to the author as a possible but tedious effort, since the number of parameters involved in the helical feed is large. A successful effort very likely would not decrease the complexity, with a corresponding increase in reliability, but it would increase the fabrication costs. Other possible ways of generating a circularly polarized TE_{11} circular waveguide mode that would not be as sensitive to dimensional changes have been investigated and are discussed below.

c. Feed redesign—theoretical. The launching of the TE_{11} circularly polarized mode in a circular waveguide transmission line can be accomplished in many ways (Ref. 2). With weight and simplicity a desirable supplement to electrical performance a dual array of reflectionless capacitive pins judicially placed in a circular waveguide has been selected as the new feed. This capacitive pin scheme was originally developed at X-band by A. J. Simmons and is discussed in detail in his paper (Ref. 3). For *Mariner*, and possibly *Voyager* frequencies and requirements, Simmons' design is scaled down in frequency and slightly modified physically to meet structural and environmental requirements. A prototype of this array of reflectionless capacitive pins is shown in Fig. 10(c).

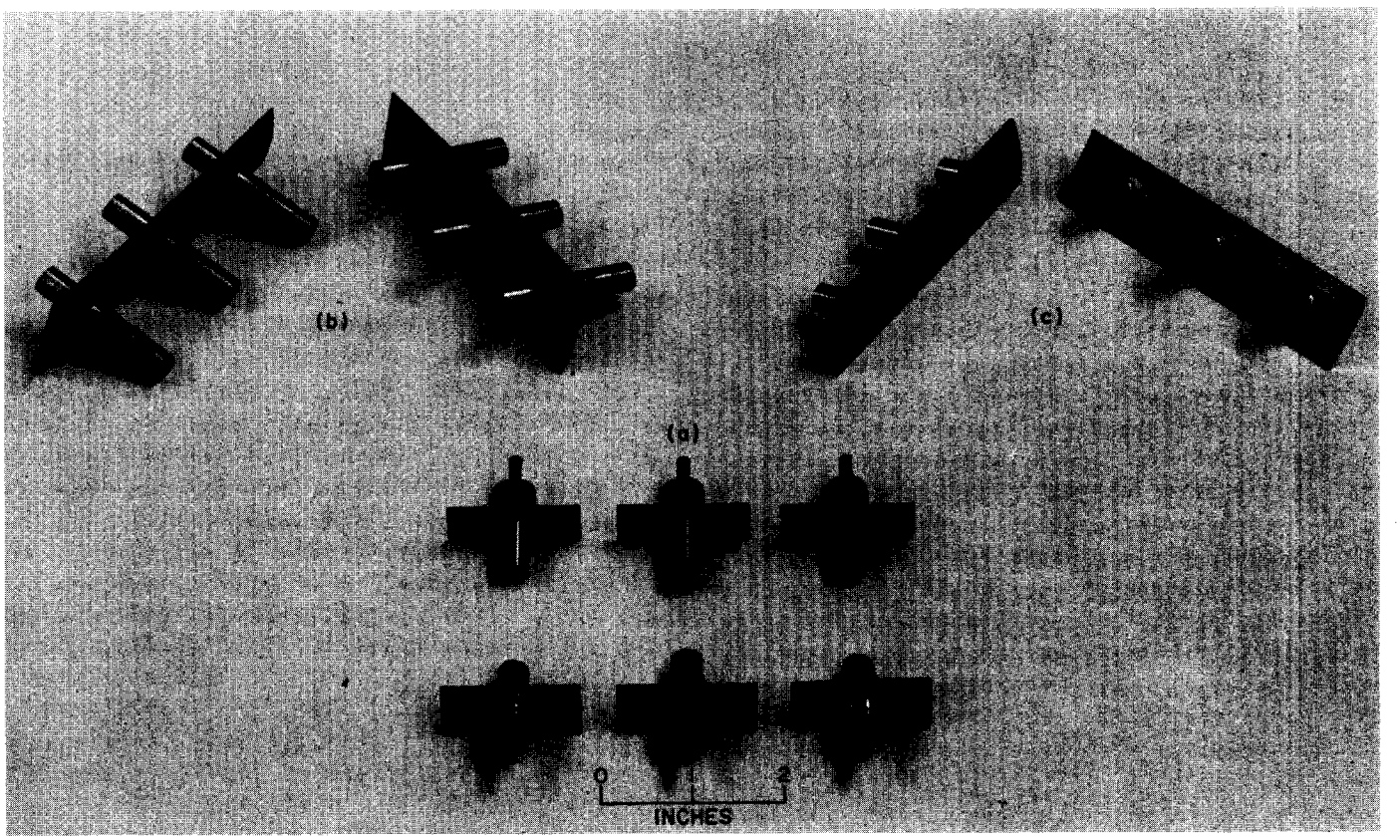

Fig. 10. Capacitive pin development models: (a) original development, pins and ridge; (b) ridge development model; (c) prototype of capacitive pin array

UNCLASSIFIED

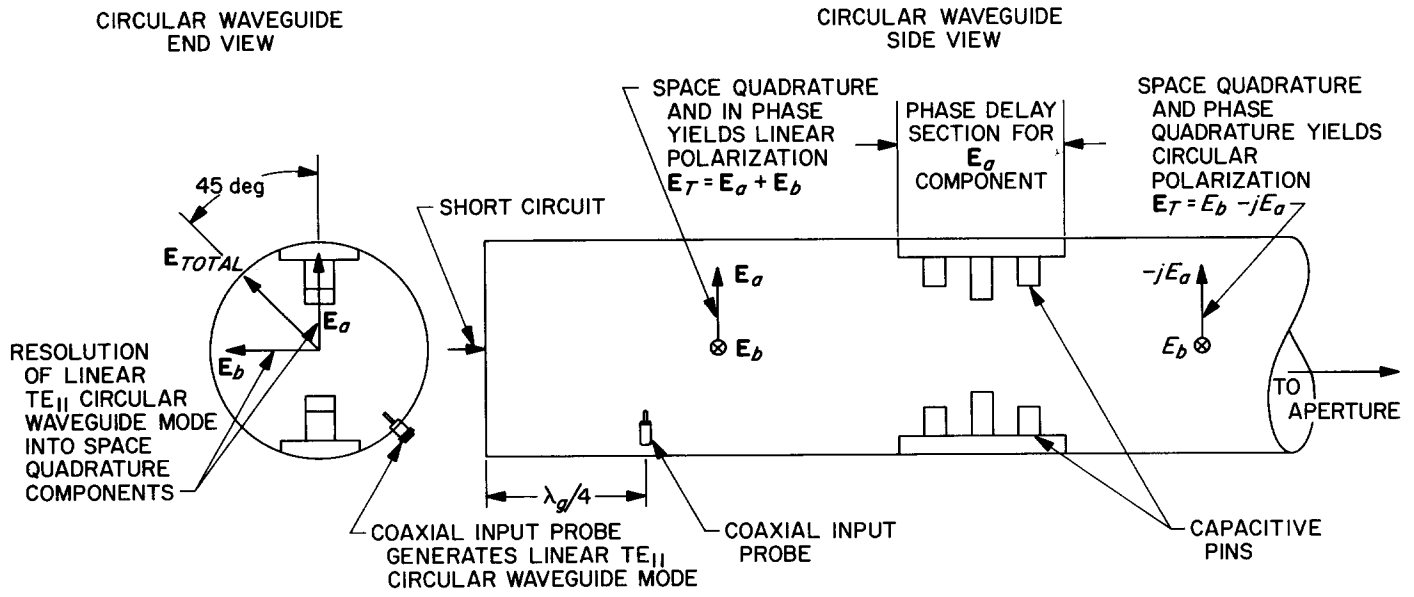
CIRCULAR WAVEGUIDE END VIEW
CIRCULAR WAVEGUIDE SIDE VIEW
SPACE QUADRATURE AND IN PHASE YIELDS LINEAR POLARIZATION $E_T = E_a + E_b$
PHASE DELAY SECTION FOR E_a COMPONENT
SPACE QUADRATURE AND PHASE QUADRATURE YIELDS CIRCULAR POLARIZATION $E_T = E_b - jE_a$
45 deg
E_{TOTAL}
E_a
E_b
SHORT CIRCUIT
RESOLUTION OF LINEAR TE_{11} CIRCULAR WAVEGUIDE MODE INTO SPACE QUADRATURE COMPONENTS
$-jE_a$
TO APERTURE
$\lambda_g/4$
COAXIAL INPUT PROBE GENERATES LINEAR TE_{11} CIRCULAR WAVEGUIDE MODE
COAXIAL INPUT PROBE
CAPACITIVE PINS

Fig. 11. Generation of circular polarization

The generation of the circularly polarized TE_{11} circular waveguide mode takes place in the following manner. A coaxial waveguide transition probe (Fig. 11) excites the linear TE_{11} circular waveguide mode. The dual capacitive pin array is placed 45 deg with respect to this probe and the linear polarized incident field that it generates. The wave incident on the array is resolved into two linear TE_{11} modes in space quadrature. The mode with the electric vector parallel to the capacitive pins is designated the $\mathbf{E}_a$ vector. The mode perpendicular to the pins is designated the $\mathbf{E}_b$ vector. These space quadrature components propagate in phase up to the array. On passing through the array the $\mathbf{E}_a$ vector undergoes a 90 deg phase delay with respect to the $\mathbf{E}_b$ vector. Recombination of the space quadrature modes, which are of equal amplitude but now in phase quadrature at the output, result in the required circularly polarized TE_{11} circular waveguide mode. The interested reader may refer to Simmons' paper for a detailed analysis.

d. Development and testing. For development and testing purposes, the microwave circuit was constructed as shown in Fig. 12. The function of the circuitry up to the input to the bi-directional coupler is to provide a matched frequency modulated source monitored in both power and frequency. The reflectometer provides input VSWR information and indicates the magnitude of input impedance variations due to the capacitive pins as the pin parameters are varied during development. The axial ratio of the resulting circularly polarized mode is measured by a small electrical probe located in the upper section of the circular waveguide. The top circular waveguide section and the probe are easily hand rotated via the mechanical rotary joint, for ready measurement of axial ratio generated by the capacitive pins. For testing purposes, the coaxial-waveguide transition probe was matched to the waveguide with a VSWR < 1.09 across the 2116–2298 Mc band. This included perturbations due to rotations of the upper section. The mismatch due to the load was insignificant, and its effect on the input VSWR measurement was negligible.

e. Experimental development results. Developmental models of the capacitive pin array are shown in Fig. 10. These models were used to investigate the dependence of the axial ratio on the pin diameter, relative pin insertion depth into the guide and ridge height. Pin diameters of 0.094, 0.188 and 0.376 in. were evaluated in the development. The 0.094-in. diameter pin was found to be deficient in satisfying the low axial ratio (< 1.0. db) at both frequencies of interest and, in general, was found to be frequency sensitive at all insertion depths into the guide. The 0.188 in. diameter pins at an insertion depth of 0.100 in. from nominal[1] were found to yield an axial ratio which was less sensitive over the 2100–2300-Mc band of frequencies; however, the ratio was above 1.0 db at the 2100-Mc frequency.

In the search for an axial ratio of less than 1.0 db over the 2100-2300-Mc frequency range, a 0.376-in diame-

[1] Insertion depth is defined as the length of the pin from the inside wall of the waveguide, as a reference. Nominal depth is 0.913 in. for the middle pin and 0.767 in. for the outer pins.

UNCLASSIFIED

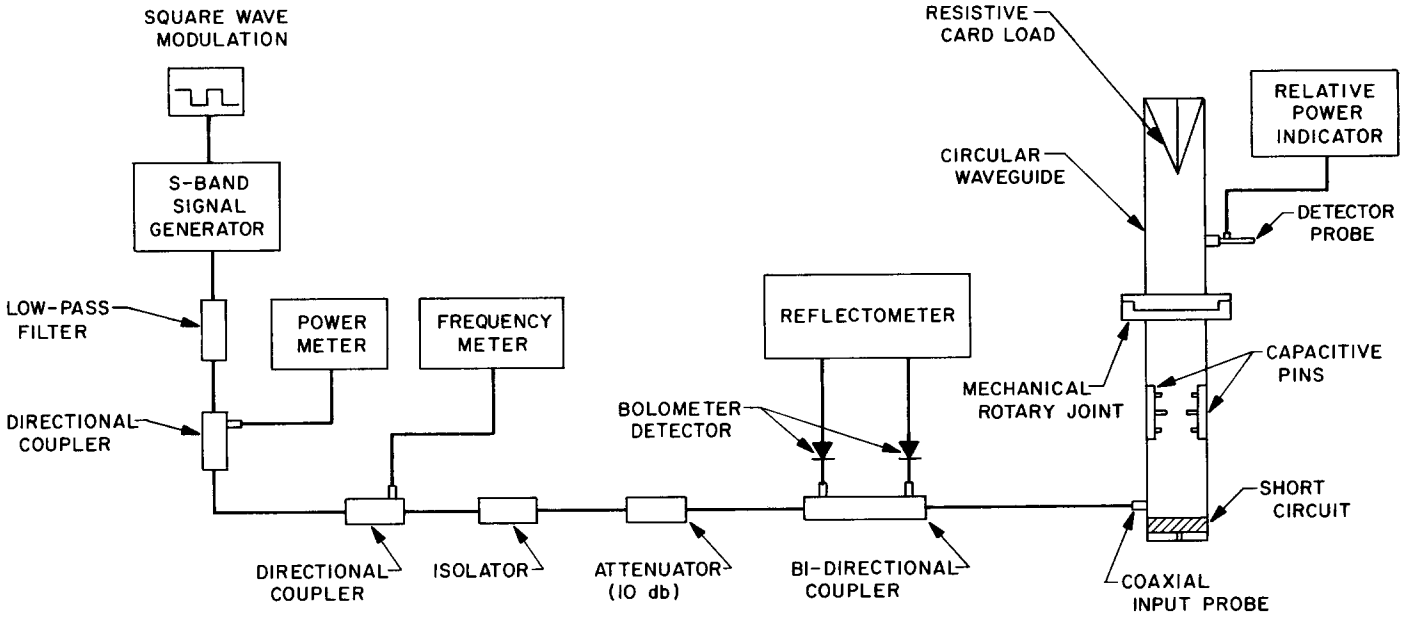

Fig. 12. Schematic, test circuit

ter was next investigated. (This diameter represents an exact scaling from Simmons' X-band model.) Axial ratio and input impedance for insertion depth of nominal and ±0.016 in. from nominal were measured. A comparison of axial ratio over a 20-Mc band, of the 0.376-in. diameter pin, the 0.188-in. diameter pin and a *Mariner* flight type helical feed are illustrated in Fig. 13. It is interesting to note the 2.86-db peak in axial ratio at the 2300-Mc frequency for the *Mariner* flight type helical antenna feed. Although the nature of this tuned effect has not been investigated it strongly suggests that such a resonant point could be critical to design parameters and hence, be in part an answer to the wide variations of on-axis ellipticity measured during acceptance testing. Inspection of Fig. 14 also shows the overall decrease in input impedance mismatch utilizing the array of capacitive pins.

The 0.376-in. diameter pin was chosen for further development because of its overall lower axial ratio at the two frequencies of interest.

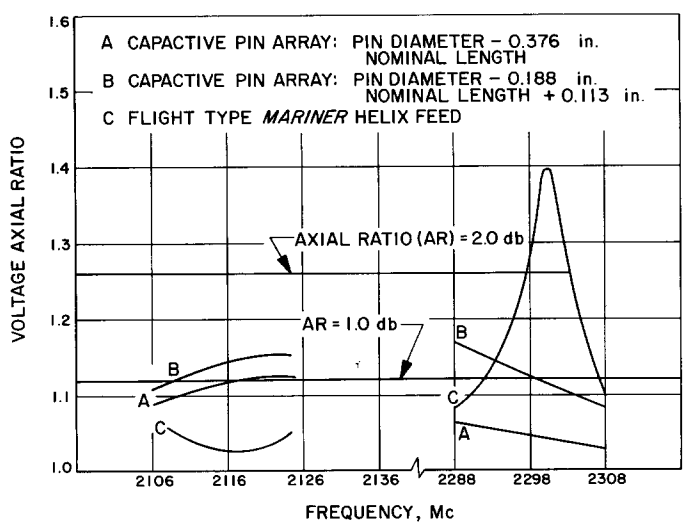
A CAPACTIVE PIN ARRAY: PIN DIAMETER – 0.376 in. NOMINAL LENGTH
B CAPACTIVE PIN ARRAY: PIN DIAMETER – 0.188 in. NOMINAL LENGTH + 0.113 in.
C FLIGHT TYPE MARINER HELIX FEED
AXIAL RATIO (AR) = 2.0 db
AR = 1.0 db
VOLTAGE AXIAL RATIO
FREQUENCY, Mc

Fig. 13. Helix-capacitive pin array comparison: axial ratio

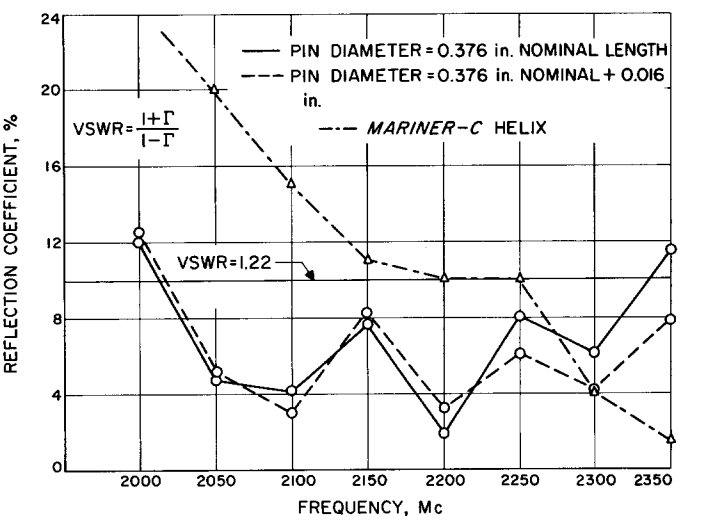
PIN DIAMETER = 0.376 in. NOMINAL LENGTH
PIN DIAMETER = 0.376 in. NOMINAL + 0.016 in.
MARINER-C HELIX
VSWR = (1+Γ)/(1−Γ)
VSWR = 1.22
REFLECTION COEFFICIENT, %
FREQUENCY, Mc

Fig. 14. Helix-capacitive pin array: input reflection coefficient

f. Ridge development. The original pin holders used for initial investigations had finite ridges on them [Fig. 10(a)] which were first assumed to have negligible effect on the measurement data. The effect, however, was later found to be significant, as evidenced by comparing phase and amplitude data with and without the ridges in the circuit. It was realized that this effect could be used to advantage electrically and that a ridge would provide structural integrity to the capacitive pin array. Utilizing the 0.376-in. diameter pin various ridge heights were investigated. A ridge height of 0.130 in. was determined as optimum in terms of output axial ratio characteristics. The ridge of 0.130 in. was further tested to determine the effect of ridge width on axial ratio. It was found that for a ridge width of $0.850 < w < 1.380$ in. the effect was negligible at both frequencies.

As a final step before fabricating a prototype for design verification, the output axial ratio for the 0.130-in. ridge height was optimized with a pin insertion depth of 0.022 in. from nominal.

g. Development to date. At this stage of the development, the method of generating the required TE_{11} circularly polarized waveguide mode consists of an array of capacitive pins, as shown in Fig. 10(b). Axial ratio and input VSWR are shown in Figs. 15 and 16, to be under 0.5 and 1.17 db respectively, at the 2116- and 2298-Mc frequencies. The plot over a frequency band reveals that the output axial ratio is relatively insensitive to frequency. Tolerance data taken thus far show that machining tolerances for pin diameter length, ridge width, and height are reasonable and that expected variations in electrical performance, due to these mechanical tolerances, are negligible.

2. Low Loss Spacecraft Coaxial Cable Systems

a. Introduction. Since the beginning of this program, two new constraints have been added to the environmental capabilities of the connector design: (1) that the assembly be able to survive a 10,000-*g* impact; and (2) that the assembly be able to survive a high temperature heat sterilization process without any degradation to its physical characteristics. With these newly added constraints, it becomes necessary to probe the present state-of-the-art and determine which type of materials will adequately survive such treacherous environments.

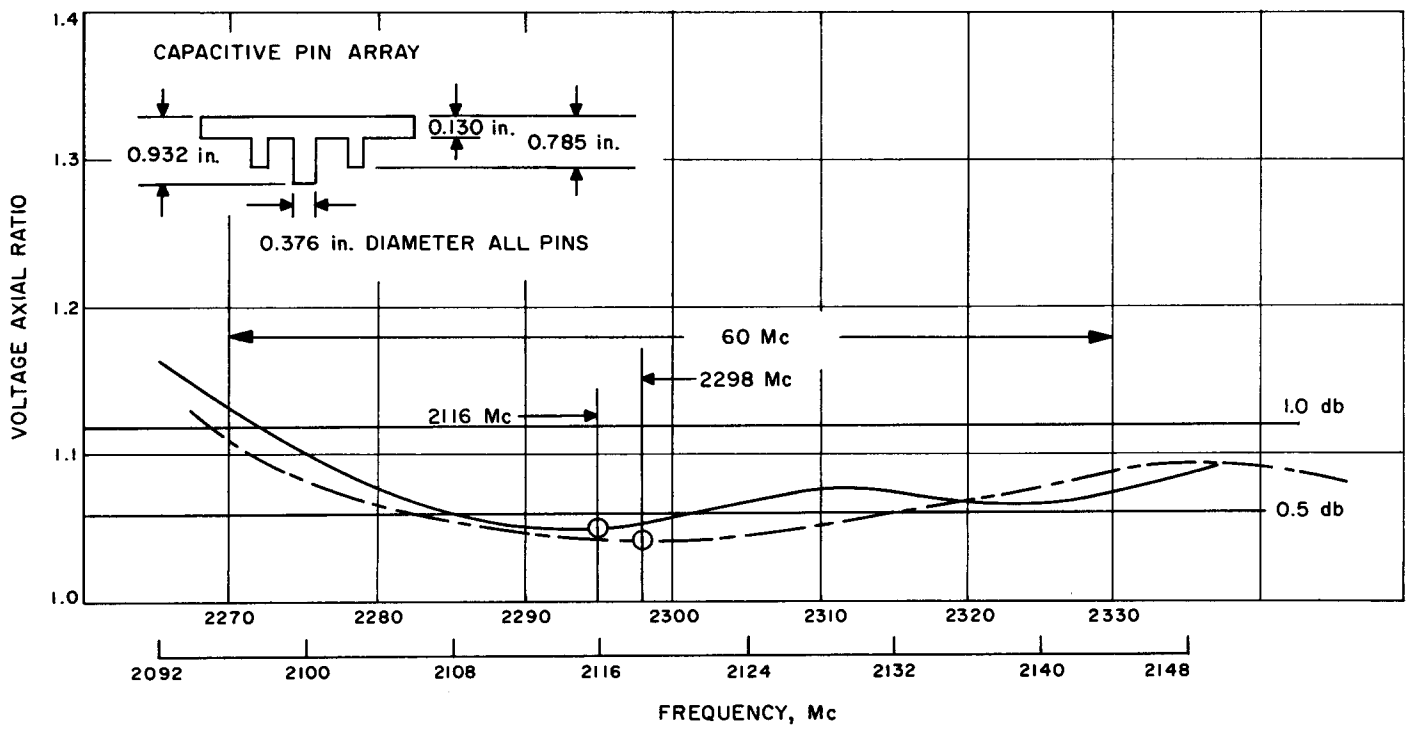

Fig. 15. Capacitive pin array axial ratio characteristics

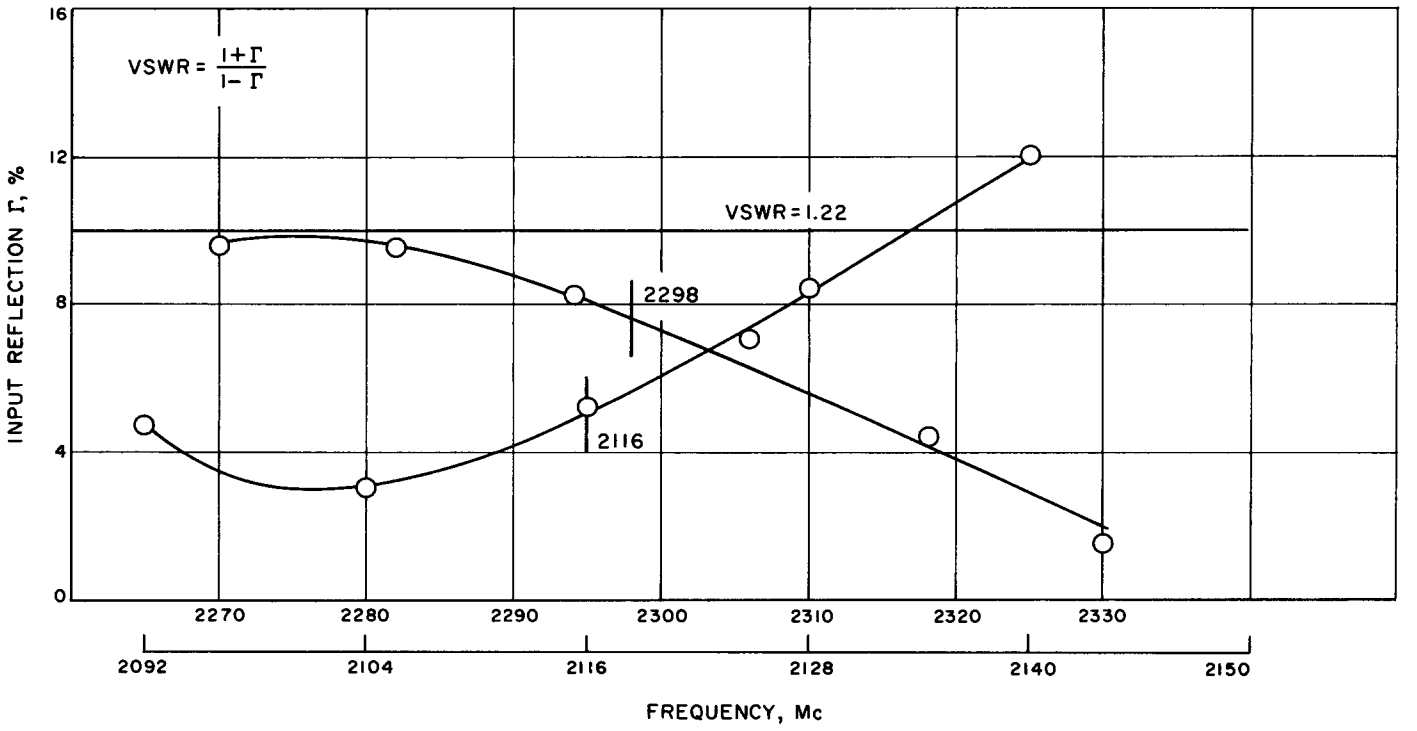

Fig. 16. Capacitive pin array feed VSWR characteristics

Besides investigating the connector materials problem, other advances have been made in the design of the center conductor alignment bullet. One basic design has been adopted with three variations stemming from it. The author feels that it should be mentioned at this point that the bullet design is presently in the theoretical design stages. No experimental data have been accumulated on this bullet design as yet; however, a thorough experimental schedule is being prepared for evaluating its merits. With this in mind, it should be understood that only the concepts of the bullet design shall be discussed here since supporting experimental data have not yet been obtained.

b. Connector body. When the first concept of the connector design was initiated, it was thought that 2024-T4 aluminum would fulfill the requirements imposed upon the system. 2024-T4 aluminum has a yield strength of 47,000 psi, a Brinell hardness of 120 and a conductivity 30% that of annealed copper. From a strength and endurance point of view 2024-T4 Al was capable of withstanding high temperatures (~300°F) and moderate shock levels (~500 g's).

The use of this aluminum alloy was considered outstanding until the two new environmental constraints were made. The ductility of 2024-T4 is acceptable for high impact environments; however, this is not where the problem lies. It lies in the fact that, when 2024-T4 Al is heated to temperatures as high as 300°F, it becomes more tempered. Therefore, the alloy loses much of its ductility, which lessens its chance of surviving a high impact.

An aluminum alloy that does not have altering characteristics when subject to 300°F is 6061-T6 Al. It has a yield strength of 40,000 psi, a Brinell hardness of 95 and a conductivity 40% that of annealed copper. These figures compare closely to those of 2024-T4 Al, but most important of all, the ductility does not change at raised temperatures. Therefore, 6061-T6 Al was incorporated into the connector design wherever possible to keep weight penalties at a minimum.

The flanged connector (*SPS 37-35*, Vol. II, p. 50) is completely made of 6061-T6 Al, except for the alignment ring which is 303 stainless steel. The selection of this particular steel was not as critical as that of aluminum, since the characteristics of stainless steel are not altered at 300°F. However, the selection was minimized to the 300 series since ferro-magnetic materials are undesirable. All of the 300 series were capable of fulfilling the requirements, but since 303 is more easily machined, it was incorporated into the design wherever stainless steel was necessary.

UNCLASSIFIED [redacted]

The alignment ring is made of stainless steel, because if it were aluminum, galling would occur due to the close fit between the ring and the aluminum shells. The shells are not anodized since, from an electrical point of view, anodizing would produce undesirable effects. However, the flanges are anodized for protection against damage during handling.

The dog-leg connector (*SPS 37-35*, Vol. II, p. 50) has its shells made of 6061-T6 Al, and the clamp and ring are made of 303 stainless steel. Here again the shells are not anodized for electrical reasons. The clamp and ring are made of stainless steel for durability and prevention of galling.

The 4-channel track connector (*SPS 37-35*, Vol. II, p. 50) has its inner shells made of 6061-T6, which are not anodized for electrical reasons. The two outer shells are made of 303 stainless steel to prevent galling, since there is a close fit between the outer and inner shells. To keep the connector's total weight to a minimum, the clamping nut is made of 6061-T6 Al, which is anodized for ruggedness.

The threaded flanged connector (*SPS 37-35*, Vol. II, p. 50) is exactly like the flanged connector, except that the flanges are made of 303 stainless steel instead of aluminum. The flanges are stainless steel because rugged tapped threads are desired for locking purposes.

c. Center conductor bullet design. Fig. 17 shows the advancement in the center conductor bullet design. All three configurations are basically the same, except for a variation in one of the alignment cylinders. Fig. 17(a) shows a design that requires minimum connector disengagement. The small alignment cylinder is dimensioned such that there is a slide fit between it and the cable's conductor. Once the spring cylinder is placed into the center conductor of one cable, a maximum distance of only 0.12 in. is necessary to engage and disengage the connector.

Fig. 17 (b) shows a slight variation of the bullet shown in Fig. 17 (a). The difference lies in the length of the slide fit alignment cylinder. It is approximately 1½ diameters long which requires a disengagement distance of 0.23 in. The purpose of such a long alignment cylinder is to hold any cocking action to a minimum by the protrusion of the cylinder.

Fig. 17 (c) shows a design exactly the same as that in Fig. 17(b), except that it is a spring press fit instead of a slide fit. The spring does not protrude back to the retainer ring because the cylinder is press fitted to the shaft of the other half of the bullet, making the bullet effectively one piece.

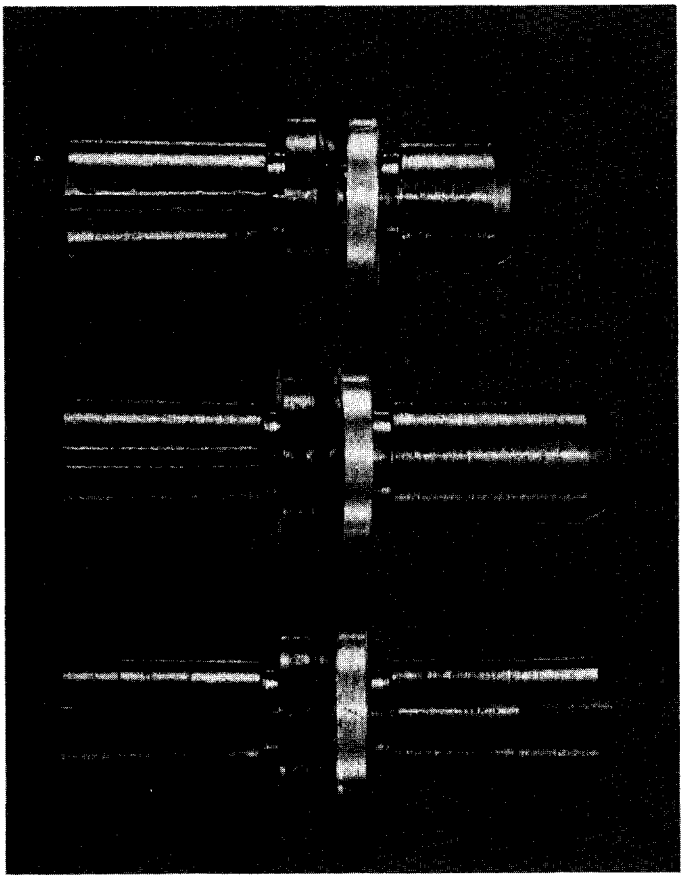

Fig. 17. Design variations of basic center conductor alignment bullets; (a) small alignment cylinder; (b) long slide fit alignment cylinder; (c) spring press fit alignment cylinder

All three bullet designs are basically the same; they all have the same interface butting surfaces. The aluminum retainer ring is allowed to move freely back and forth thus allowing the distance to be varied between the butting surfaces. The movable ring is aluminum and the shaft is beryllium copper. The dissimilar metals reduce the chance of galling between the moving parts. The three wave spring offers tension to the system, which insures a good cable butting contact. Because of the spring action contact, a more continuous system is possible at the conductor interface. This variable dimension feature compensates for any tolerance build-up which may occur on the connector shells interface. (*SPS 37-35*, Vol. II, p. 50).

UNCLASSIFIED [redacted]

D. Propulsion

1. Monopropellant-Hydrazine Investigation

During the past two years, monopropellant hydrazine rocket engine and gas generator testing programs have revealed a problem when employing spontaneous catalyst beds (*SPS 37-25*, Vol. IV, pp. 100–101). A chamber pressure disturbance occurs shortly after ignition, usually within 1–10 sec, depending upon injector and catalyst bed configurations. The disturbance appears as a transient pressure excursion, or spike, with a magnitude of about 170% of steady-state chamber pressure P_c, as measured by a Taber transducer and recorded by an oscillograph. It has been hypothesized that the pressure disturbance occurs when the primary reaction zone, which starts at the lower end of the catalyst bed, undergoes a rapid shift to the top portion of the catalyst bed. The liquid phase contained in the top section of the bed is heated by conduction and recirculation until it undergoes a rapid vaporization and chemical reaction with an associated change in specific volume, which results in a rapid pressure rise, or spike. The reaction zone location is detected by the color change in the chamber wall caused by the increase in local temperature, as well as by bed thermocouple measurements.

The spiking problem can most likely be eliminated by forcing the initial reaction zone to start at the top end of the bed. The various methods which have been employed to achieve this are listed below:

(1) The geometric surface-area-to-volume-ratio of the catalyst pellets was increased by cutting the standard ⅛-in. diameter by ⅛-in. long cylinders in half.

(2) Hollow and solid cone injection nozzles with various cone angles were used.

(3) The distance from the injector face to the catalyst bed was varied.

(4) The bed loading factor G, defined as the flow rate per unit cross-sectional area of the chamber ($\dot{w}/A_c$), was varied by lowering the injector pressure with an associated decrease in chamber pressure (*SPS 37-31*, Vol. IV, pp. 197–201).

Although certain combinations of the above methods have shown promise by causing the pressure spike to occur at a time closer to ignition, the spike has not been completely eliminated, nor has the initial reaction zone been moved all the way to the top end of the bed.

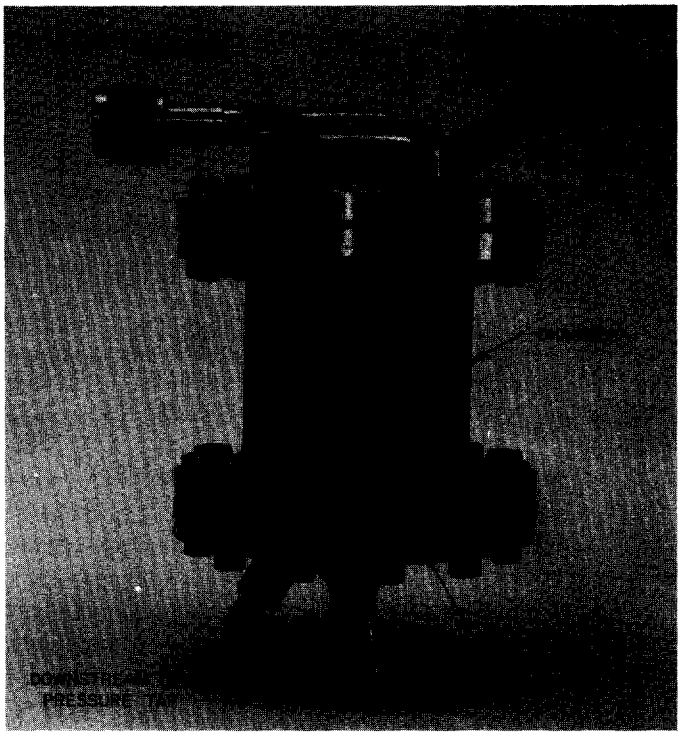

Fig. 18. Test engine configuration

As a continuation of the work done previously, a bed loading study at constant chamber pressure, was conducted. Only the diameters of the injector spray nozzles and nozzle throat were varied. The basic hardware used for this series of test (Fig. 18) is similar to the *Mariner-C* engine; however, it was adapted for spontaneous catalyst test work. Fig. 19 shows a typical *Mariner-C* flight-type injector in which the center injection spray nozzle is used for nitrogen tetroxide (N_2O_4) during the hypergolic ignition period ($\sim$1 sec), while the remaining four nozzles are used for hydrazine (N_2H_4). Fig. 20 shows a heavyweight, modified injector as adapted for spontaneous catalyst testing in which five 30-deg hollow-cone spray nozzles are used for fuel. Five injectors and five nozzle throats were designed and fabricated to mate with an existing heavyweight, flanged test chamber. These configurations allowed tests to be made at five different flow rates, or G-loadings, while maintaining a constant chamber pressure and constant pressure drop across the injector. The nominal downstream chamber pressure was 188 psia while the nominal pressure drop across the injector was 100 psi. The injector face was located 0.95 in. from the top of the catalyst bed with the nozzle tips extending 0.08 in. from the face. The catalyst bed diameter was

UNCLASSIFIED

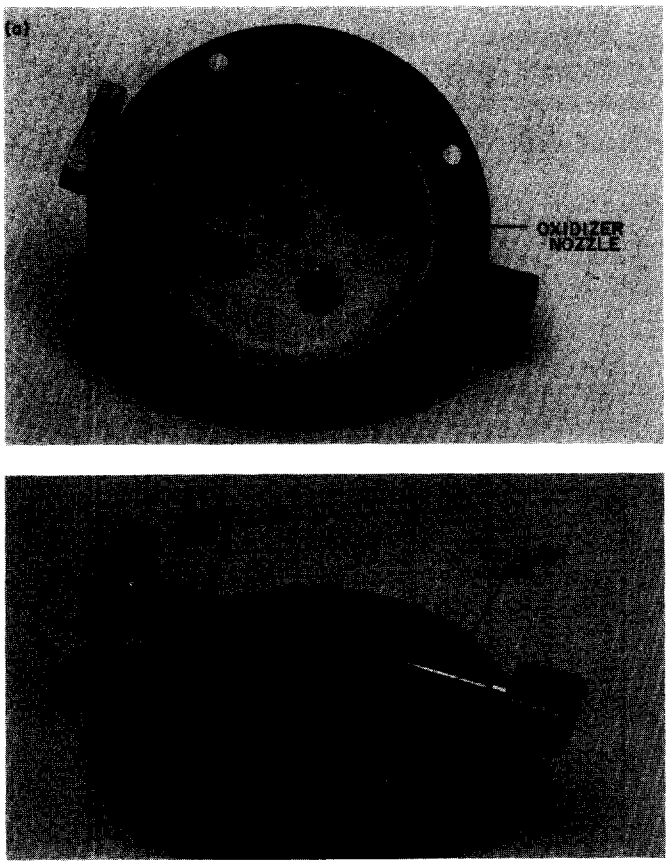

Fig. 19. *Mariner*-C flight-type injector: (a) injector face; (b) side view

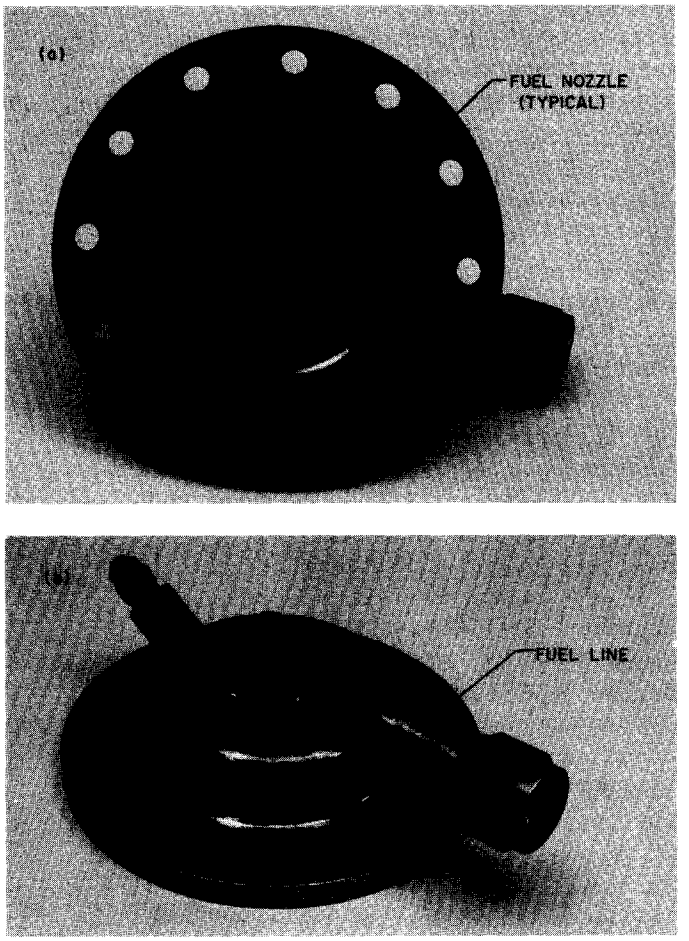

Fig. 20. Heavyweight test injector: (a) injector face; (b) side view

2.65 in. and its length was 3.45 in. The spontaneous catalyst[1] was in the form of cylinders, ⅛ in. diameter by ⅛-in. long. The same batch was used in all tests.

Several tests were made to determine what effect bed loading variations would have on the pressure spike, both in magnitude and location. A summary of the test results is given in Table 2. The pressure spike usually occurred within 3–10 sec after ignition. This time interval appeared to be independent of bed loading. As seen in Fig. 21, there appeared to be little correlation between the pressure spike overshoot ratio ($P_{transient}/P_{steady\text{-}state}$) and bed loading for the flow range tested. Although the datum points for higher flow rates have more dispersion, one could infer that the overshoot ratio is a weak function of bed loading, as seen by the slight negative slope in the bandwidth of data.

It should be noted from Table 2 that in three tests the spike did not occur within the 10-sec period. Prior to test 462, the catalyst had been used for some other experimental firings and was exposed to the atmosphere for a prolonged period. Catalyst oxidation or water absorption during that interval may have caused the extremely long time delay. In test 476 the spike was not observed, and in test 477 the spike occurred approximately 20 sec after ignition. Following test 477, samples of several pellets were taken from the catalyst bed and tested for activity. Observation indicated that the reactivity of the pellets with hydrazine was much reduced in comparison with the unused catalyst tested in a similar manner.

From the knowledge gained in this experimental testing program, together with work previously done at the Laboratory, it is believed that the pressure spike problem will be eliminated only by utilizing an unconventional, unique injector design in conjunction with an optimum catalyst bed configuration. A limited-scope investigation is continuing and will be reported upon subsequently.

[1]Type 8416-20, Shell Development Co., Emeryville, California.

UNCLASSIFIED

Table 2. Bed loading test results

Test No.	Length of run, sec	Engine serial number	Ignition delay[a] msec	Fuel line pressure P_{fl}, psia	Upstream chamber pressure P_{cu}, psia	Downstream chamber pressure P_{cd}, psia	Catalyst bed pressure drop P_{cat}, psi	Steady-state downstream chamber pressure amplitude peak-to-peak, psi	Fuel temperature, °F	Ambient throat area A_t, in.^{2}	Actual flow rate w_a, lbm/sec.	Bed loading G, lbm/sec. in.^{2}	Downstream chamber pressure spike occurrence, sec.	Downstream chamber pressure spike magnitude[b], psia	Downstream chamber pressure spike overshoot ratio	Characteristic velocity c^{*c}, ft/sec.
455	30	1	20.0	319	—	183	—	12	75	0.150	0.210	0.038	3.0	333	1.82	4250
462	30	2	11.5	304	212	188	24	10	82	0.132	0.190	0.034	19.6	311	1.66	4250
463	30	2	23.5	306	215	191	24	10	73	0.132	0.194	0.035	8.5	286	1.50	4240
464	30	2	27.5	306	215	189	26	10	73	0.132	0.194	0.035	7.9	243	1.28	4200
465	30	3	11.0	303	207	189	18	12	80	0.113	0.168	0.030	6.4	284	1.50	4180
466	30	3	25.2	303	208	190	18	11	83	0.113	0.168	0.030	5.0	337	1.78	4180
467	30	4	11.8	310	199	189	10	5	75	0.075	0.113	0.020	10.2	341	1.80	4100
468	30	4	18.9	311	200	190	10	5	76	0.075	0.114	0.021	6.0	352	1.86	4090
469	44	5	11.0	296	195	191	4	4	74	0.038	0.060	0.011	5.0	358	1.87	3920
470	45	5	16.0	293	190	185	5	4	80	0.038	0.058	0.010	5.8	313	1.69	3890
471	45	5	17.8	294	191	186	5	4	80	0.038	0.059	0.011	5.8	322	1.73	3880
472	30	4	10.0	310	200	191	9	9	86	0.075	0.114	0.020	2.7	331	1.74	4100
473	30	4	12.0	312	199	189	10	6	83	0.075	0.133	0.020	3.4	334	1.77	4090
474	30	3	10.2	303	207	188	19	7	82	0.113	0.168	0.030	4.3	290	1.54	4150
475	30	3	14.4	304	207	188	19	7	84	0.113	0.168	0.030	4.8	258	1.37	4160
476	30	2	14.0	302	—	—	—	—	76	0.132	—	—	—	—	—	—
477	30	2	21.6	302	209	188	21	13	75	0.132	0.193	0.035	20.1	322	1.72	4190

[a] When the propellant valve is opened, a fuel line pressure transient occurs with an initial decay followed by a rapid rise. The ignition delay is defined as the time interval between the time that the fuel line pressure first rises to the steady-state value and the time that the downstream chamber pressure (P_{cd}) reaches 5% of steady-state value.

[b] The spike magnitude is the value of the largest pressure oscillation, which occurs on the oscillograph record during the disturbance period.

[c] The c^* calculation is made using the calculated hot throat area.

UNCLASSIFIED [redacted]

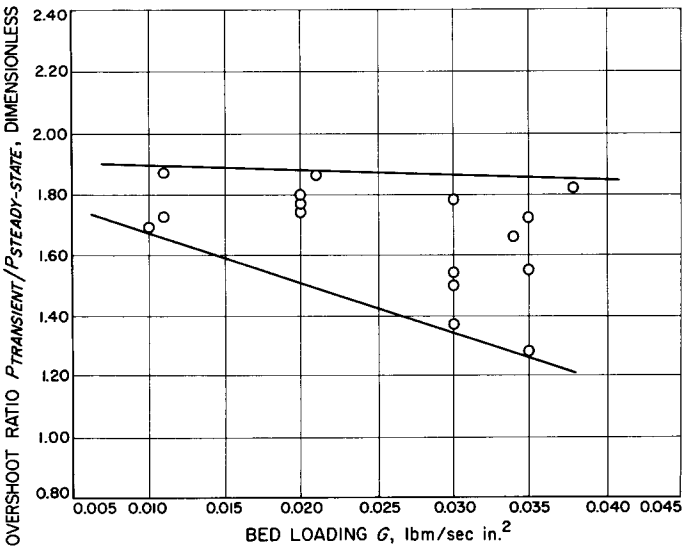

Fig. 21. The effect of bed loading upon pressure spike overshoot ratio

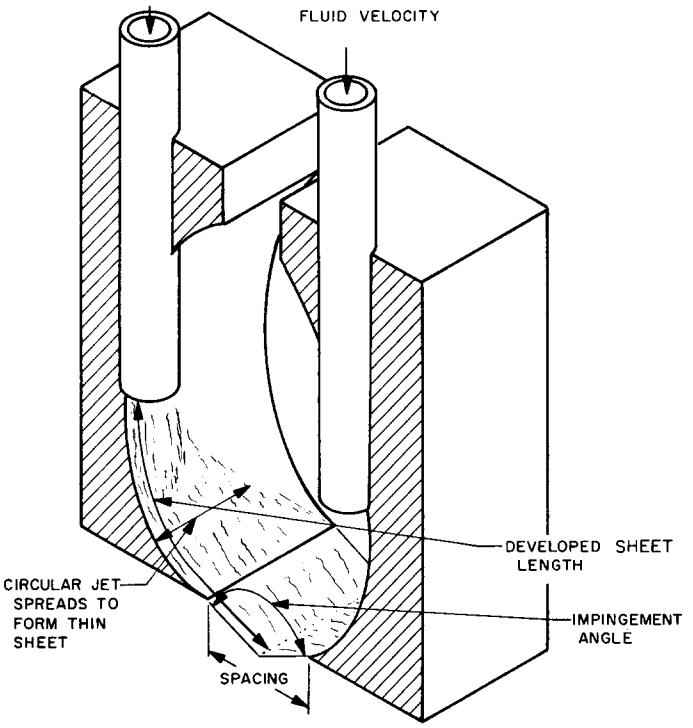

Fig. 22. Schematic representation of impinging sheet doublet element

2. Injector Development Program

a. Introduction. Although impinging jets (both like and unlike) have been used for many years in liquid bipropellant rocket engine injectors, they exhibit a number of disadvantages. Precise and reproducible alignment of the impinging jets is often difficult, and the resultant combustion efficiency may be strongly dependent on the physical size of the elements and the stream energy available for mixing. In addition, for extremely reactive storable propellants such as nitrogen tetroxide (N_2O_4) and hydrazine (N_2H_4), chemical reaction may occur at the liquid interface and disrupt the streams before effective propellant mixing has occurred (Ref. 4). In the light of these inherent disadvantages, considerable attention at this Laboratory has in recent months been devoted to the cup-and-plug injector element (*SPS 37-31*, Vol. IV, p. 203), and to the impinging-sheet unlike doublet injector element (Ref. 5 and *SPS 37-35*, Vol. IV). In each case the propellant sheet is formed by directing a jet of fluid against a solid, curved deflector surface, as shown in Fig. 22 for an impinging-sheet doublet element. The following discussion concerns this particular element, although the sheet-formation data are being used to design a cup-and-plug injector as well. The latter results will be reported in subsequent Space Programs Summaries.

The combustion efficiency of the impinging-sheet element is related to the degree of mixing and atomization it can achieve. The latter depend on the key "macro" parameters of

(1) Momentum.

(2) Momentum ratio.

(3) Sheet dimensions and degree of coincidence at the impingement line.

(4) The included impingement angle.

These, in turn, depend only on the deflector geometry and the velocities and physical properties of the working fluids. Thus, if the fluid flow onto the deflector is controlled, it should be possible to achieve predictable and reproducible injector performance in terms of only the element's geometry and propellant flowrates.

A necessary first step, therefore, is the definition of the relationship between deflector geometry and the properties of the resultant sheets for various liquid velocities and physical properties. Accordingly, a detailed experimental program having this objective is currently in progress, and some preliminary results will be presented here.

b. Apparatus and procedures. The experimental apparatus is shown schematically in Fig. 23. Cylindrical deflector surfaces of radius R and included angle θ were

UNCLASSIFIED [redacted]

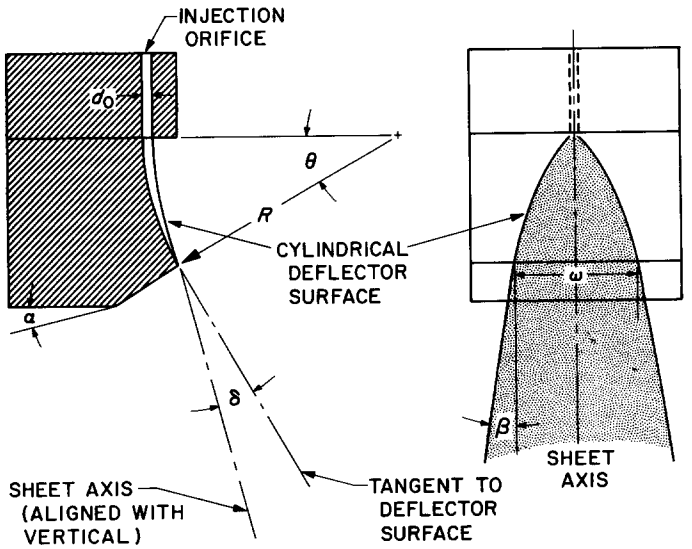

Fig. 23. Schematic representation of experimental apparatus

machined into aluminum blocks and polished to a high degree of surface finish. Deflector radii ranging between 0.10 and 0.60 in., and deflector angles of 15, 20, and 30 deg, were investigated. The water was introduced tangentially onto the deflector. Experiments were conducted with orifice diameters of 0.020, 0.030, and 0.040 in. and with injection velocities of 91 and 129 ft/sec.

At these injection velocities (on the order of those employed in typical liquid rocket engines), the jets from the orifices turn onto the deflector surface and form a thin liquid sheet as they spread through a half-angle β (Fig. 23) to a width w before leaving the deflectors. (The corresponding developed sheet length L, is the arc-distance $\theta\pi R/180$, when θ is expressed in degrees.) In general, the sheets did not exit tangentially, however. Rather, the planes of the sheets were turned through the angle δ away from the tangents to the deflector surfaces, as shown in Fig. 23.

The sheet turning angle δ was determined to within about ± 1 deg *in situ* as follows. Upon rotation of the entire apparatus, the axis of the flowing sheet was aligned with the vertical by optical techniques, and the angle α between the bottom surface of the block and the horizontal was measured. The angle δ was then found from

$$\delta = \theta - \alpha \tag{1}$$

The sheet width w and spreading half-angle β were measured from high-speed photographs made of the flowing sheets, using synchronized-pulse lighting. The lens axis was orthogonal (± 5 deg) to the sheet axis in each case.

c. Preliminary findings. Data reduction and analysis are still in progress; however, some preliminary correlations, which neglect effects of Reynolds and Weber numbers, are reported here. The correlations shown represent one convenient way in which to present the data collected thus far, and are intended to show gross effects only. Because of these limitations, no attempt should be made to scale the data to other geometries, velocities or fluids, until a more complete analysis has been conducted.

Plots of δ/θ vs L/d_o are shown in Figs. 24 and 25 for sheets formed from water flowing at velocities of 91 and 129 ft/sec respectively. There is some data scatter due to the accuracy (about ± 1 deg) of the spray angle measurement technique. However, most of the data lie on a smooth curve, and it appears as though velocity has little, if any, effect on the position of the curve. At both velocities, deflector geometry seems to exert the primary influence on the sheet turning angle for constant fluid properties.

w/d_o is plotted vs L/d_o in Fig. 26 for water flowing at 91 ft/sec. ω/d_o is seen to vary as the square root of L/d_o. For values of θ of 15, 20, and 30 deg, the proportionality factor depends on θ, so that at 91 ft/sec,

$$\frac{w}{d_o} = 0.57\,\theta^{0.48}\left(\frac{L}{d_o}\right)^{0.5}, \qquad \theta \leq 30 \text{ deg} \tag{2}$$

Corresponding data collected at the higher water velocity of 129 ft/sec are shown in Fig. 27. w/d_o is again found to vary as the square root of L/d_o, and for values of θ of 15, 20, and 30 deg is correlated by

$$\frac{w}{d_o} = 0.69\,\theta^{0.42}\left(\frac{L}{d_o}\right)^{0.5}, \qquad \theta \leq 30 \text{ deg} \tag{3}$$

Comparison of Figs. 26 and 27 indicates that w increases with velocity at fixed geometry. The exact manner of this variation cannot be defined until the results of experiments at several different velocities have been evaluated.

If it is assumed that each flowing sheet, when flattened out, is a trapezoid, then the spreading half-angle β would be expected to be

$$\beta = \tan^{-1}\frac{w - d_o}{2L} \tag{4}$$

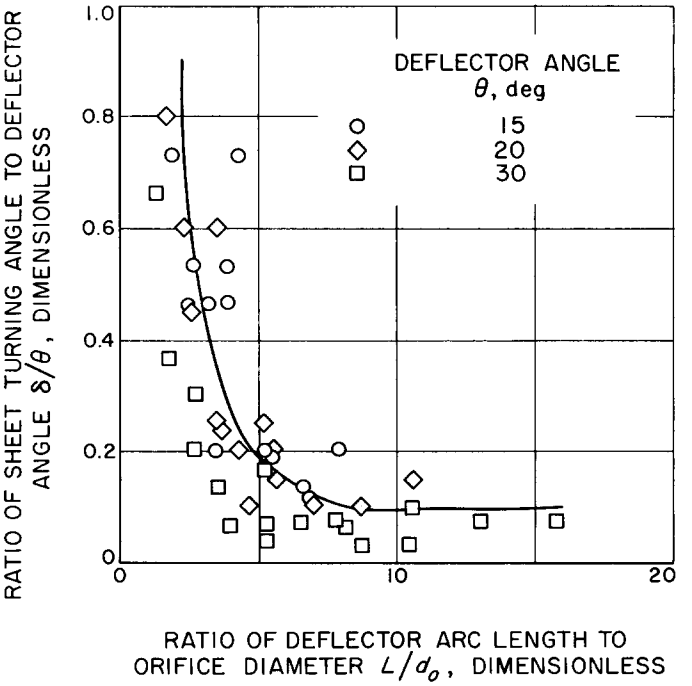

Fig. 24. Variation of ratio of sheet turning angle to deflector angle with deflector geometry for water at 91 ft/sec

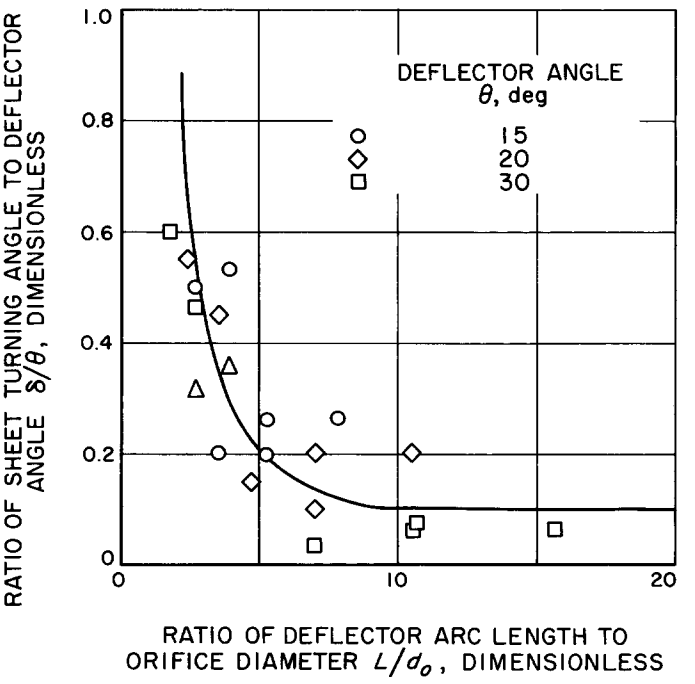

Fig. 25. Variation of ratio of sheet turning angle to deflector angle with deflector geometry for water at 129 ft/sec

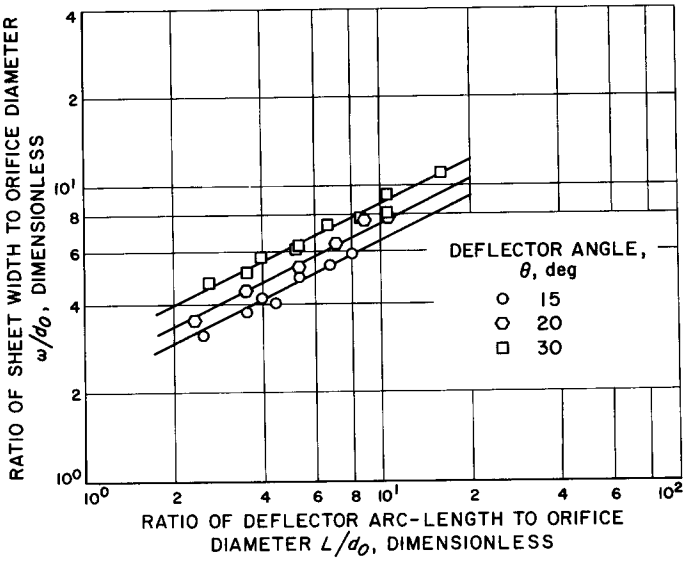
RATIO OF SHEET WIDTH TO ORIFICE DIAMETER ω/d₀, DIMENSIONLESS
DEFLECTOR ANGLE, θ, deg
15
20
30
RATIO OF DEFLECTOR ARC-LENGTH TO ORIFICE DIAMETER L/d₀, DIMENSIONLESS

Fig. 26. Variation of ratio of sheet width to orifice diameter with deflector geometry for water at 91 ft/sec

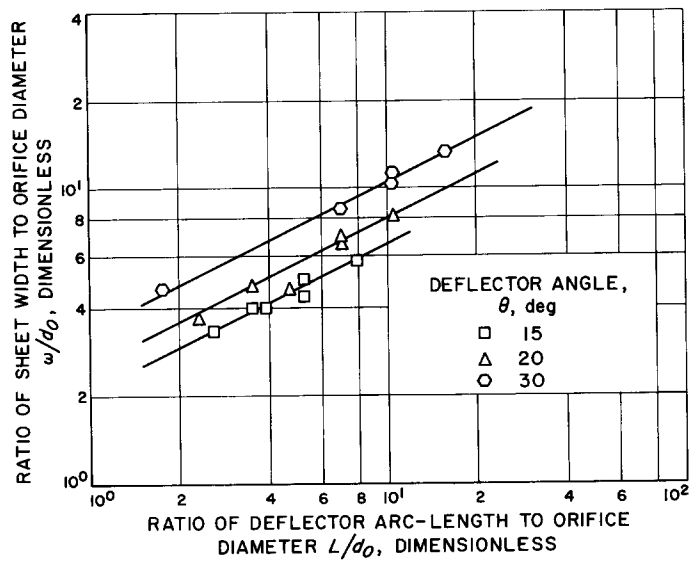
RATIO OF SHEET WIDTH TO ORIFICE DIAMETER ω/d₀, DIMENSIONLESS
DEFLECTOR ANGLE, θ, deg
15
20
30
RATIO OF DEFLECTOR ARC-LENGTH TO ORIFICE DIAMETER L/d₀, DIMENSIONLESS

Fig. 27. Variation of ratio of sheet width to orifice diameter with deflector geometry for water at 129 ft/sec

Actually, the sides of the "trapezoid" are slightly curved, and a plot of all the data at $V = 91$ ft/sec indicates that

$$\beta = \tan^{-1}\frac{w - d_o}{2L} - 0.27 \qquad (5)$$

Spreading angle data are still being reduced for the higher velocity flows, but similar results are expected.

d. Future effort. Additional studies with water flowing at about 65 ft/sec are planned to complete definition of velocity effects. Deflectors with angles of 45 deg will be studied. Experiments to investigate the effects of fluid physical properties such as density, viscosity, and surface tension will then be carried out. Attempts will also be made to improve the accuracy of the turning angle measurements.

E. Quality Assurance and Reliability

1. Effects of Prolonged Exposures at −196°C Upon a Small Signal Transistor

A test performed in the Component Reliability Laboratory has demonstrated that a small signal transistor is capable of withstanding exposures of −196°C for 310 hr. This test was performed on Texas Instruments 2N2412. The 2N2412 is a PNP small signal switching transistor. It is housed in a TO-18 case which contains a 20 × 20 mil chip. The chip is attached by the use of a gold preform to the header. The leads are ball bonded. This mechanical configuration is typical of most small signal planar transistors.

Associated with the transistors exposed for the long term were 10 samples which were also cycled between +25° and −196°C. No effects were observed in either group that could pose reliability problems. As all chemical activity is greatly attenuated at this temperature, and almost all mechanical strains should have become apparent by the 6 cycles of +25° to −196°C, it can be concluded that the 2N2412 will withstand the −196°C storage indefinitely. The 2N2412's were purchased commercially and screened at JPL prior to this test.

The test procedure consisted of selecting a group of 40 parts at random from a screened lot of greater than 100 samples. Ten samples were drawn aside for control units, 20 others were separated out for long-term exposure, and the remaining 10 samples were used for temperature vs time studies. All samples were initially measured for six sensitive parameters

I_{CES}	V_{CE} (SAT)
I_{EBO}	V_{BE} (SAT)
h_{FE}	BV_{CEO}

UNCLASSIFIED

All of these parameters were checked at each subsequent measurement point. At each measurement point of the test samples, the control samples were also measured, and the measuring equipment was verified. The group of 20 long-term storage samples were placed in a glass vial which was weighted and submerged in liquid nitrogen throughout the test. The 10 time vs temperature samples were similarly prepared and were measured at intervals of 4, 20, 50, 100, 310 and 410 hr.

The foregoing test is valid for the screened 2N2412's; however, it should not be presupposed that commercial unscreened parts will be able to meet this exposure, as the manufacturer will guarantee only a lower exposure limit of −65°C. This test has demonstrated that these parts can be screened to withstand this exposure with a high yield.

2. *Evaluation Test of Ceramic Capacitors*

In recent years larger capacitance values have been made available, which design engineers want to incorporate into their designs because of the size advantage. Based on the results of a recently completed test, it now appears feasible to extend the approved usage of ceramic capacitors to a higher range of capacitance values. The results, however, quite clearly show that not all the manufacturers who supplied parts for this test provided capacitors that are suitable for spacecraft applications. In fact, only one part can be recommended with good confidence—Type MC605 by Aerovox Corp.

Extended range ceramic capacitor lines from eight manufacturers were evaluated. All capacitors were subjected to identical tests to permit direct comparisons of the various types. The test groups and sequence of tests were made in such a way that parameter behavior could be analyzed with respect to time, temperature, sequence of environments and stress conditions.

Basically, the results indicated a wide variability among the suppliers in the area of reliability. However, the behavior of parameters were quite similar. With respect to temperature, capacitance changes were typically −10 to +15% over the temperature range of −55 to +125°C. Dissipation factor reached a maximum at −55°C with a typical value of 3.0% and a minimum at 125°C with a typical value of 0.5%. Insulation resistance was nominally about 100,000 MΩ at room temperature and generally did not drop below 1,000 MΩ at 125°C. With respect to the environmental test, parameter changes were insignificant in vibration and shock, exhibited some perturbation in temperature cycling, and exhibited a drop of insulation resistance in the moisture resistance test. During the operating life test, those parts which were affected by the moisture test generally dried out (i.e., insulation resistance increased), and otherwise the parameters were reasonably stable (i.e., no changes beyond specification). In order to make comparisons, a box score type presentation (Table 3) was made.[2]

The table summarizes the occurrences of catastrophic failures only; blanks indicate no failure. Catastrophic failures are defined as capacitors which exhibit opens, shorts or physical damage to the extent that they cannot be functionally tested. The test levels represented are as follows:

(1) Visual inspection at 3 × magnification.

(2) Screen test twice-rated voltage at 125°C for 168 hr.

(3) Vibration at 50–3000 cps, 35 g rms, 3 axes, 6 sweeps/axis.

(4) Shock at 300-g peak, 1 msec, 3 axes, 10 shocks/axis.

(5) Thermal cycling at −55 to +125°C, 10 cycles.

(6) Moisture resistance per method 106 of MIL-STD-202.

(7) Temperature coefficient was determined from parameter measurements over the −55 to +145°C range.

(8) Terminal strength at 5 lb pull followed by 5 bends through 360-deg arcs.

(9) Breakdown voltage was a gradual increase of applied voltage until the dielectric broke down.

(10) Life tests for 2000 hr.

In conclusion, the results of the test indicated a wide range of capability among the various manufacturers. Since the units tested represent new processes and "beyond the standard range," the results do not necessarily reflect the capability of various companies to produce standard items. Only the Aerovox Type MC605 of those capacitors tested merits consideration for spacecraft usage at this time.

[2]Manufacturers are represented by numbers. Where two types of capacitors were tested per manufacturer, the difference is noted by attached subscript letters.

UNCLASSIFIED

Table 3. Catastrophic capacitor failures

Manufacturer	Visual inspection ($n = 170$)	Group I ($n = 50$) screen test	Group I and II ($n = 100$)				Group III ($n = 10$) temperature coefficient and terminal strength tests	Group IV ($n = 10$) breakdown voltage destructive test	Group V ($n = 50$) control group	Life test matrix					
			Vibration	Shock	Temperature cycle	Moisture resistance				50v, 85°C ($n = 75$)	50v, 125°C ($n = 15$)	100v, 85°C ($n = 15$)	100v, 125°C ($n = 15$)	200v, 85°C ($n = 15$)	200v, 125°C ($n = 15$)
MC605 (Aerovox) 1								740–2500							
2		3	7	1		1		940–1370		11	3	3	2	5	
3a			1	1				760–1260			2				
3b		3	2		1	1		270–620		9	3		3	6	8
4		1				1		580–1300							1
5		3	5	1		21		420–1050		12	10	7	11	14	2
6		4	3	4	2			820–1200		7	2	2		2	2
7a			8	1	7			1800–3600		13	1	1	1		1
7b			1					480–1240		4	2	3	3	2	
8			2	1		4		420–910		3					1

3. Toroidal Transformer Fabrication Technique

Many of the transformers used in spacecraft are manufactured on toroidal cores. Heretofore, certain techniques have been employed which do not contribute to the highest reliability. One of these is the manner in which leads are connected to the wires in the toroid.

It is common practice among manufacturers to utilize the following terminating procedure. After the toroid winding is complete, the various wire ends, representing starts and finishes of windings, are stripped of their insulation by either chemical or mechanical means. Each winding end and a prestripped flexible lead wire are twisted together and soldered. One or more patches of adhesive insulating tape are placed on the wound coil. Next, the soldered joint is placed in the center of the patch and other pieces of tape are placed on top of it, insulating and securing the lead in place, the number of layers of tape depending upon the voltage the lead is carrying as well as lead size. Since toroids may have as many as thirty leads, the taping procedure introduces a great deal of bulk into the assembly. Often the finished leads and winding are covered with a layer of mylar or glass tape to assist in securing leads and insulation in place. Theoretically, these tape patches and the final wrap should be set by curing in an oven at a specified temperature, but in practice, this is too often omitted. The whole coil is then impregnated, encapsulated or potted in a plastic potting cup.

A change from this procedure is embodied in a new method developed at JPL. The toroid is wound in a normal fashion and all lead ends stripped. A terminal board consisting of a flat ring of thin (0.015 – 0.030 in.) epoxy glass is prepared. As many brass eyelets as there are leads are swaged to the board as shown in Fig. 28.

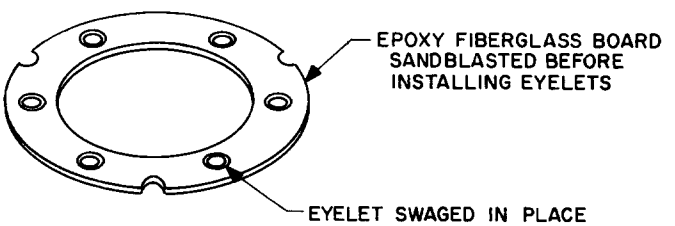

Fig. 28. Brass eyelets swaged to epoxy fiberglass terminal board

A thin layer of insulating material is placed on the toroidal coil and the terminal board placed over it as shown in Fig. 29. One of the coil wires is drawn through each eyelet. At the same time, a prestripped flexible lead wire is inserted through each eyelet (Fig. 30). The two wires are then twisted together and soldered into the eyelet.

The terminal board can then be tied to the toroid. This whole assembly can be potted, encapsulated or otherwise protected.

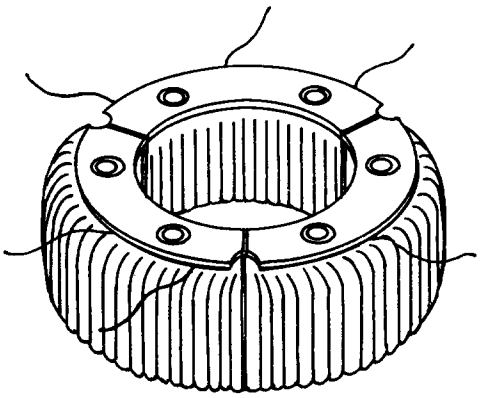

Fig. 29. Terminal board positioned on toroid

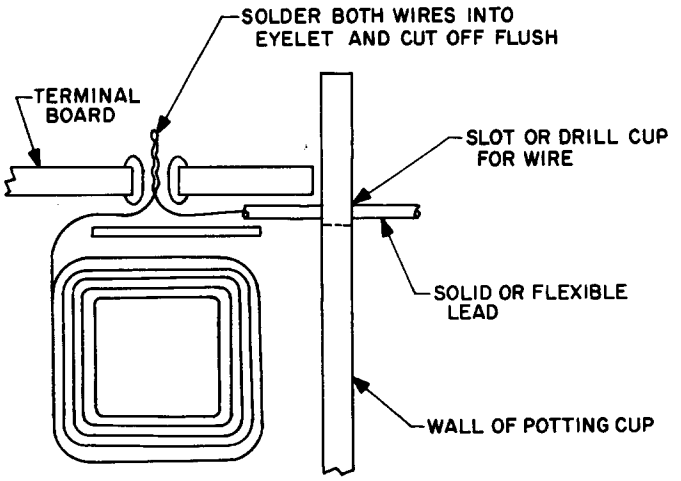
SOLDER BOTH WIRES INTO EYELET AND CUT OFF FLUSH
TERMINAL BOARD
SLOT OR DRILL CUP FOR WIRE
SOLID OR FLEXIBLE LEAD
WALL OF POTTING CUP

Fig. 30. Lead wire connections to toroid

There are a number of advantages in the new method. First, the flexible leads are firmly anchored to a terminal board and do not depend upon adhesive tapes to hold them in place. Secondly, the joint can be visually inspected at any time up to potting, and if a clear potting material is used, it can be inspected any time. Third, with the flexible lead wire stripped to a point just short of where it emerges from the potting cup, wicking, penetration of moisture through the stranded wire, is prevented.

References

1. Kraus, J. D., *Antennas*, McGraw-Hill Book Co. Inc., pp. 175—176, 1950.
2. Jasik, H., *Antenna Engineering Handbook*, McGraw-Hill Book Co. Inc., Chapter 17, 1961.
3. Simmons, A. J., "A Compact Broadband Quarter Wave Plate," *Proceedings of the Institute of Radio Engineers*, pp. 1089—1090, September 1952.
4. Johnson, B. H., *An Experimental Investigation of the Effects of Combustion on the Mixing of Highly Reactive Liquid Propellants*, Technical Report No. 32-689, Jet Propulsion Laboratory, Pasadena, July 15, 1965.
5. Dipprey, D. F., et al, *On the Evolution of Advanced Propulsion Systems for Spacecraft*, Technical Report No. 32-735, Jet Propulsion Laboratory, Pasadena, July 15, 1965.

UNCLASSIFIED [redacted]

III. Future Projects

A. Introduction

The JPL Future Projects Office is responsible for the direction, sponsorship, and, in cooperation with other technical areas of the Laboratory, origination of advanced mission and future project studies of interest and applicability to the Laboratory space program. The objective is to ensure the availability, when required, of preliminary technical information and plans for potential missions, including associated information on spacecraft systems, instrumentation, launch vehicle systems, resources, and schedule requirements. This preliminary information will be used to define specific flight mission projects and to provide general guidelines for the direction of Laboratory research and advanced development efforts. A summary or informative abstract of the results of each study will be presented in the *Space Programs Summary*, including, where appropriate, reference to the more detailed formal final report issued by the Future Projects Office.

B. Systems

1. A Systems Comparison of Direct and Relay Link Communications for an Eventual Long-Life Mars Surface Experiment[1]

This article summarizes the results of an evaluation of two alternate schemes for returning data to Earth from an eventual long-life Mars surface experiment. One scheme involves transmission of the lander data to an artificial planetary satellite for subsequent transmission to Earth, and the other involves transmission directly from the lander to Earth. The relay system, requiring the orbiting and simultaneous operation of a communications satellite with the landing of the capsule, represents

[1]A detailed description of this analysis is presented by Barber, T. A., Billy, J. M., and Bourke, R. D., in *A Systems Comparison of Direct and Relay Link Data Return Modes for Advanced Planetary Mission*, Technical Memorandum No. 33-228, Jet Propulsion Laboratory, Pasadena, California (To be published).

a considerable increase in complexity over the direct-link system. The satellite receives data from the lander sporadically at a high rate and transmits it continuously to Earth at a low rate. With the direct system, on the other hand, it is necessary to erect and steer a highly directional antenna to support the required data rate for reasonable powers. The requirements for these operations serve to degrade the reliability of the direct-link system. Furthermore, since the lander is on the surface of a rotating planet, it can view and transmit to Earth during only a fraction of the day. Both systems must return the data over the enormous, continuously changing Earth–Mars range. These and other technical aspects of the two schemes were evaluated so that their data return capabilities could be quantitatively compared.

Three comparison criteria were used:

(1) Effective information rate $\dot{I}_e = \dot{I}_i \cdot v$, where $\dot{I}_i$ is the actual information rate when communications are established, and v is the fraction of time that transmission is actually carried out. Whereas the direct scheme has only one effective information rate, the relay scheme has two: one for the lander-to-orbiter link and the other for the orbiter-to-Earth link. The smaller of these two determines the amount of lander data received at Earth.

(2) Reliability $R(t)$, the probability that each system is operating properly at time t. This has been obtained through reliability and failure-rate models of subsystems and required functional sequences.

(3) Expected total bits

$$I(T) = \dot{I}_e \int_{t_0}^{T} R(t)\, dt,$$

where t_0 is the time at which data begin to accrue, and T is greater than t_0 and less than or equal to the end-of-mission time. This quantity is actually the measure of the average amount of information received at Earth using one particular scheme.

To numerically evaluate these three comparison criteria, two basic assumptions were made: (1) The lander was assumed to gather and return to Earth 10^{10} bits of data over a 6-mo period, and (2) the opportunities of 1975 and 1977 were assumed for trajectory purposes. As a consequence of the first assumption, the following telecommunications system characteristics were used in this analysis: The Mars-to-Earth links for both schemes were taken to use steerable high-gain (~35-db) 12.5-ft-diameter antennas, 50-w S-band transmitters, Earth coverage as required with the 210-ft-diameter Deep Space Instrumentation Facility antennas, command playback, and adequate on-board data storage. The lander-to-orbiter link of the relay system was taken to use a VHF transmitter; an antenna on the planet surface erected to the local vertical; an antenna on the orbiter directed toward the planet center, which, in conjunction with the lander antenna, was to give about 10 db of total gain; command playback; and automatic acquisition. Adequate storage (a few percent of the total bits) to prevent the loss of significant amounts of data was assumed for both ends of the link.

The results of this study, shown in Table 1, may be summarized as follows:

(1) For the assumed parameters, the effective bit rate of the relay link is better by a factor of three.

(2) The relay link is less reliable than the direct link, being about twice as likely to fail during the 6-mo mission.

(3) The amount of expected cumulative data using the relay link is greater than that using the direct link by a factor of two.

(4) For the assumed lander relay transmitter power, a 4000- × 20,000-km orbit reduces the relay-link effective bit rate below that of the direct link.

Table 1. Results of the direct- and relay-link systems comparison

Comparison criteria	Relay system				Direct Mars-to-Earth link
	Lander-to-orbiter link[a] with indicated orbital altitude			Mars-to-Earth link[b]	
	5000 km	2000 km	4000 × 20,000 km		
Viewing fraction v	0.118	0.038	0.124	~1	0.33
Actual information rate $\dot{I}_i$, bits/sec	28,300	143,000	2930	3340	3340
Effective information rate $\dot{I}_e$, bits/sec	3340	5450	364	3340	1110
Total bits (perfect reliability), × 10^{10}	5.2	8.5	0.57	5.2	1.7
Expected total bits $I(T)$, × 10^{10}	0.63	1.03	0.069	0.63[c]	0.33[c]

[a] 10-w lander transmitter; 10-db antenna system gain.
[b] 35-w radiated power; 36.7-db antenna system gain.
[c] 400-day transit; 0.75 direct link antenna reliability.

(5) Both systems are data-rate-limited by the Earth link.

(6) The 10^{10}-bit requirement necessitates the use of a high-power transmitter and a very-high-gain steerable antenna for both systems.

On the basis of these results, it may be concluded that both systems yield comparable expected total data return and that, consequently, the choice between a direct- and relay-link system should be made on grounds other than data return capability.